

AD-A250 555



## MENTATION PAGE

Form Approved  
GME No. 0104 0185

Estimated to average 1.5 minutes per response, including the time for reviewing instructions, searching existing data sources, gathering and reviewing the data, and completing the review. Send comments regarding this burden estimate or any other aspect of this collection of data, including suggestions for reducing the burden, to Washington Headquarters Service, Directorate for Information Operations and Reports, 1215 Jefferson Davis Highway, Suite 1204, Arlington, VA 22202-4302, and to the Office of Management and Budget, Paperwork Reduction Project (0104-0185), Washington, DC 20503.

REPORT DATE 1991		3. REPORT TYPE AND DATES COVERED THESIS <del>MONITORING</del>	
4. TITLE AND SUBTITLE Studies in Dynamic Characterization and Control of a Flexible Structure and Optical Beampath		5. FUNDING NUMBERS	
6. AUTHOR(S) Marcus R. Schulthess, 2d Lt			
7. PERFORMING ORGANIZATION NAME(S) AND ADDRESS(ES) AFIT Student Attending: University of Washington		8. PERFORMING ORGANIZATION REPORT NUMBER AFIT/CI/CIA-91-130	
9. SPONSORING / MONITORING AGENCY NAME(S) AND ADDRESS(ES) AFIT/CI Wright-Patterson AFB OH 45433-6583		10. SPONSORING / MONITORING AGENCY REPORT NUMBER	
11. SUPPLEMENTARY NOTES			
12a. DISTRIBUTION / AVAILABILITY STATEMENT Approved for Public Release IAW 190-1 Distributed Unlimited ERNEST A. HAYGOOD, Captain, USAF Executive Officer		12b. DISTRIBUTION CODE	
13. ABSTRACT (Maximum 200 words)			
<div data-bbox="289 1417 759 1638" data-label="Text"> <p><b>DISTRIBUTION STATEMENT A</b> Approved for public release; Distribution Unlimited</p> </div> <div data-bbox="1006 1381 1352 1617" data-label="Text"> <p><b>DTIC</b> <b>ELECTE</b> <b>MAY 11 1992</b> <b>S B D</b></p> </div>			
14. SUBJECT TERMS		15. NUMBER OF PAGES 92	
		16. PRICE CODE	
17. SECURITY CLASSIFICATION OF REPORT	18. SECURITY CLASSIFICATION OF THIS PAGE	19. SECURITY CLASSIFICATION OF ABSTRACT	20. LIMITATION OF ABSTRACT

University of Washington

Abstract

**Studies in Dynamic Characterization and Control of a Flexible  
Structure and Optical Beampath**

by Marcus R. Schulthess

Chairperson of Supervisory Committee:

Prof. Juris Vagners

Dept. of Aeronautics and Astronautics

The dynamic characterization and control of a flexible structure and optical beampath is explored. The experiment is motivated by the expanding demand for structurally mounted space based laser pointing and tracking systems. The setup of the cantilevered UWAA planar truss is based on a similar setup at the Air Force Academy. An existing finite element model is modified to reflect the characteristics of the UWAA truss and experimentally validated. A reduced order truss model suitable for simulation is developed and validated with the hardware. The formulation of linear and non-linear models for the AJT and tilting mirror actuators are explored. The design and implementation of the mirror and structural control is manifested in the form of proportional-integral (PI) feedback to a tilting control mirror to actively reject line of sight disturbances and velocity feedback to on-off AJT actuators to suppress large amplitude low frequency lateral structural vibrations. Good line of sight disturbance rejection is demonstrated for the first four lateral modes of the flexible truss structure. The AJT velocity feedback controller was used to suppress large amplitude low frequency oscillations to bring structural vibrational motions to within limited range of the tilting mirror platform. A baseline theoretical model of the reduced order truss and control actuators was constructed in SIMULAB and thoroughly validated. The simulation model provides a theoretical basis for future work on the UWAA planar truss. Theoretical design and practical implementation issues are explored and future research possibilities suggested.

2 Lt Marcus R. Schulthess, USAF

Masters of Science in Aeronautics and Astronautics, 1991. 92 Pages

**92-11979**

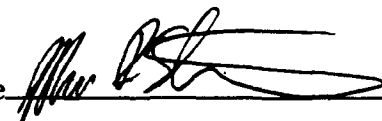


**92 5 01 038**

Date December 18, 1991

In presenting this thesis in partial fulfillment of the requirements for the Master's degree at the University of Washington, I agree that the Library shall make its copies freely available for inspection. I further agree that extensive copying of this thesis is allowable only for scholarly purposes, consistent with "fair use" as prescribed in the U. S. Copyright Law. Any other reproduction for any purposes or by any means shall not be allowed without my written permission.

Signature



Date

18 Dec 91

<b>Accession For</b>	
NTIS GRA&I	<input checked="checked" type="checkbox"/>
DTIC TAB	<input type="checkbox"/>
Unannounced	<input type="checkbox"/>
Justification	
By	
Distribution/	
Availability Codes	
Dist	Avail and/or Special
A-1	

University of Washington

Abstract

Studies in Dynamic Characterization and Control of a Flexible  
Structure and Optical Beampath

by Marcus R. Schulthess

Chairperson of Supervisory Committee:

Prof. Juris Vagners

Dept. of Aeronautics and Astronautics

The dynamic characterization and control of a flexible structure and optical beampath is explored. The experiment is motivated by the expanding demand for structurally mounted space based laser pointing and tracking systems. The setup of the cantilevered UWAA planar truss is based on a similar setup at the Air Force Academy. An existing finite element model is modified to reflect the characteristics of the UWAA truss and experimentally validated. A reduced order truss model suitable for simulation is developed and validated with the hardware. The formulation of linear and non-linear models for the AJT and tilting mirror actuators are explored. The design and implementation of the mirror and structural control is manifested in the form of proportional-integral (PI) feedback to a tilting control mirror to actively reject line of sight disturbances and velocity feedback to on-off AJT actuators to suppress large amplitude low frequency lateral structural vibrations. Good line of sight disturbance rejection is demonstrated for the first four lateral modes of the flexible truss structure. The AJT velocity feedback controller was used to suppress large amplitude low frequency oscillations to bring structural vibrational motions to within limited range of the tilting mirror platform. A baseline theoretical model of the reduced order truss and control actuators was constructed in SIMULAB and thoroughly validated. The simulation model provides a theoretical basis for future work on the UWAA planar truss. Theoretical design and practical implementation issues are explored and future research possibilities suggested.

## TABLE OF CONTENTS

<b>List of Figures</b>	<b>v</b>
<b>List of Tables</b>	<b>vii</b>
<b>Chapter 1 Introduction</b>	<b>1</b>
1.1 Background . . . . .	1
1.2 Problem Definition . . . . .	2
1.3 Hardware Description . . . . .	4
1.3.1 Truss . . . . .	5
1.3.2 Air-Jet-Thrusters . . . . .	5
1.3.3 Load Cell . . . . .	5
1.3.4 Accelerometers . . . . .	6
1.3.5 Laser . . . . .	6
1.3.6 Optics . . . . .	6
1.3.7 Piezo Controlled Tilting Mirror . . . . .	6
1.3.8 Photodetectors . . . . .	8
1.3.9 Reaction Mass Actuator . . . . .	8
1.3.10 Electro-Mike Position Sensor . . . . .	10
1.3.11 Analog Computers . . . . .	10
1.3.12 Dynamic Signal Analyzer . . . . .	10
1.4 Thesis Overview . . . . .	11
<b>Chapter 2 System Modeling</b>	<b>12</b>
2.1 Overview . . . . .	12
2.2 Truss Modeling . . . . .	12
2.2.1 The 63-DOF Constrained-Free Finite Element Model . . . . .	13
2.2.2 63-DOF Validation Via Beam Theory and Experimental Hard- ware . . . . .	17
2.2.3 Truss Model Reduction . . . . .	21

2.3	Air-Jet-Thruster Modeling . . . . .	25
2.3.1	AJT Theoretical Modeling . . . . .	26
2.3.2	Experimental Validation of AJT Model and Linear Model Development . . . . .	29
2.4	Piezo Actuated Mirror Modeling . . . . .	34
2.4.1	Experimental Validation of Tilting Mirror Platform . . . . .	35
2.5	Disturbance Mirror Characterization . . . . .	36
<b>Chapter 3</b>	<b>Classical Controller Design</b>	<b>39</b>
3.1	Overview . . . . .	39
3.2	Open Loop Synthesis Model . . . . .	40
3.2.1	SIMULAB Model Development . . . . .	40
3.2.2	Open Loop Synthesis Model Validation . . . . .	45
3.3	Controller Design Method . . . . .	49
3.4	Tilting Mirror Controller . . . . .	49
3.4.1	Theoretical Controller Design and Hardware Implementation . . . . .	49
3.4.2	Theoretical and Experimental Results . . . . .	52
3.5	Air-Jet-Thruster Control . . . . .	60
3.5.1	Controller Implementation and Results . . . . .	63
<b>Chapter 4</b>	<b>Conclusions and Recommendations for Future Work</b>	<b>68</b>
4.1	Overview . . . . .	68
4.1.1	Conclusions . . . . .	68
4.1.2	Recommendations for Future Work . . . . .	70
	<b>Bibliography</b>	<b>72</b>
	<b>Appendix A AJT Control Circuitry</b>	<b>74</b>
	<b>Appendix B Modal Damping Coefficients</b>	<b>80</b>
	<b>Appendix C Numerical Values Required for SIMULAB Simulation</b>	<b>83</b>
C.1	Four Degree of Freedom Linear Truss Model . . . . .	83
C.2	Non-linear AJT Parameters . . . . .	85

**Appendix D Required Inputs to MAPMODES for UWAA Planar Truss 86**

<b>Appendix E Equipment List</b>	<b>90</b>
E.1 Laser Hardware and Optical Bench . . . . .	90
E.2 Optics . . . . .	90
E.3 Custom Fabricated Optical Hardware . . . . .	91
E.4 Control Mirror and Accompanying Hardware . . . . .	91
E.5 Custom Fabricated Tilting Mirror Hardware . . . . .	91
E.6 Optical Sensing Equipment . . . . .	91
E.7 Custom Designed Sensing Hardware . . . . .	92
E.8 Instrumentation and Electronics . . . . .	92



## LIST OF FIGURES

1.1	Experimental Setup . . . . .	3
1.2	Arrangement of Experimental Hardware . . . . .	4
1.3	Tilting Mirror and Support Structure . . . . .	7
1.4	Power Spectrum of the Sensor Noise . . . . .	9
2.1	63 DOF Planar Truss . . . . .	15
2.2	Clamped-Free Euler Bernoulli Beam . . . . .	17
2.3	Normalized Bending Mode Shapes Comparison: Beam Theory (dotted), Finite Element Model (solid), and Hardware (dashed). . . . .	21
2.4	AJT Signals . . . . .	27
2.5	Non-Linear Block Diagram for AJT Model . . . . .	29
2.6	AJT Test Jig . . . . .	30
2.7	Experimental Data: Normalized Transistor Power Signal (dashed) Load Cell Data (solid) . . . . .	31
2.8	AJT Theoretical(solid) and Experimental(dashed) Normalized Frequency Response . . . . .	32
2.9	Mirror-Piezo System . . . . .	34
2.10	Experimental (dashed) and Theoretical (solid) Control Mirror-Piezo Tilting Platform Transfer Function ( $\frac{\Theta_{mirror}(s)}{V_{control}(s)} \frac{mrad}{volt}$ ). . . . .	37
3.1	Open Loop SIMULAB Block Diagram . . . . .	41
3.2	Hardware Implemented Control Input Limiter Circuit . . . . .	45
3.3	Theoretical (solid) and Experimental (dashed) Frequency Response from Accelerometer Output to AJT Control Signal Input . . . . .	46
3.4	Theoretical and Experimental Truss Free Decay Time Responses . . . . .	47
3.5	Theoretical and Experimental Truss Free Decay Time Responses . . . . .	48
3.6	Analog Control Circuit for PI Controller . . . . .	52
3.7	Controller Stability Margins . . . . .	53
3.8	Closed Loop Bandwidth . . . . .	54

3.9	Open (dashed) and Closed (solid) Loop Magnitude Plot . . . . .	55
3.10	Disturbance Rejection Curve With Curve Fit (dashed) . . . . .	56
3.11	Experimental Closed Loop Time Responses to Continuous Structural Disturbances . . . . .	58
3.12	Theoretical Closed Loop Time Responses to Continuous Structural Disturbances . . . . .	59
3.13	Time Responses to Structural and Non-structural White Noise Distur- bances . . . . .	60
3.14	Frequency Response Comparison Between Exact Integration (solid) vs. Approximate Integrator (dashed) . . . . .	63
3.15	Analog Implementation of AJT Controller . . . . .	64
3.16	Mode 1 Experimental and Theoretical Open and Closed Loop Re- sponses for AJT Controller . . . . .	65
3.17	Mode 2 Experimental and Theoretical Open and Closed Loop Re- sponses for AJT Controller . . . . .	66
3.18	Closed Loop SIMULAB Model . . . . .	67
A.1	Lead Network Circuit Diagram . . . . .	75
A.2	Lead Filter Frequency Response . . . . .	77
A.3	Accelerometer Circuit . . . . .	78
A.4	AJT Switching Circuit . . . . .	79
B.1	Rate of Decay of Oscillation Measured by Logarithmic Decrement . .	81
D.1	MAPMODES Coordinate Transformations . . . . .	87

## LIST OF TABLES

2.1	Theoretical and Experimental Lateral Vibrational Natural Frequencies	20
2.2	Experimentally Determined Damping Coefficients . . . . .	23
3.1	Truss Outputs for Linear SIMULAB Model . . . . .	42
3.2	SIMULAB Gain Blocks . . . . .	43
3.3	Mirror Parameters . . . . .	44
3.4	Modal Disturbance Rejection Values in dB . . . . .	57
C.1	AJT Rise Time Filter Parameter Values . . . . .	85
D.1	Average Mass and Stiffness Properties of Flexible Truss Members . .	86

## ACKNOWLEDGMENTS

I would like to express my appreciation to those that were instrumental in ensuring the completion of this thesis. First and foremost I thank my wife for putting up with the many late nights and lost weekends as I was completing my research and preparing this report, and for her love and support throughout my studies here at the University of Washington. Special thanks to Lt. Mike Shepherd who worked with me on the planar truss, helping to take data and helping solve many of the problems that were encountered. Thanks to Otto and Bill in the machine shop who spent many hours expertly constructing the precision parts required to set up and perform the experiment. Thanks to Bob Blair for his help and expertise in setting up the required electronics. Also, special thanks to Major Ken Barker for providing me with research ideas and getting me started on the modeling process. Finally, I would like to thank Professors Vagners for his help in funding the experiments and producing this thesis.

## Chapter 1

# INTRODUCTION

### *1.1 Background*

Since man first entered space over three decades ago, there has been an ever increasing demand for high bandwidth accurate pointing systems. Applications for these systems include communications, scientific research, and directed energy systems for programs such as the Space Defense Initiative (SDI). The pointing systems deployed in space usually consist of optical elements (mirrors, reflectors, etc...) which are mounted on a lightweight flexible structure. Disturbances often excite the flexible modes of the structure disrupting perhaps a communications relay, command signal to the space structure, or data acquisition. Sources of excitation for space systems include asymmetric solar heating, micro-meteorite impacts, space craft maneuvering, and onboard operations such as pump vibrations and radiator motions [7]. Though these structural excitations may be on the order of a few inches, a disturbed laser beam path that must travel hundreds of miles to its destination, may miss its target by many feet. These disturbances adversely affect the beam path and make targeting and tracking impossible without some form of disturbance rejection and/or vibration suppression.

There are many different methods that can be used to stabilize a laser beam path disrupted by excitation of the flexible support structure's vibrational modes. A high bandwidth fast steering mirror for disturbance rejection was investigated by Adams [1]. In his thesis, Adams investigated the effect of having a mirror reject small disturbances of the flexible optical structure. Modal vibration suppression was not analyzed and therefore, the structural disturbances were limited to the throw of the mirror. Hallauer and Lamberson [5] examined vibration suppression of a flexible optical structure using air-jet-thrusters (AJTs) and reaction mass actuators to actively suppress modal vibrations caused by excitation of the flexible structure's vibrational modes. Vibration suppression, though useful for increasing the inherent damping of

the structure, could not be used to control non-structural disturbances to the beam path including atmospheric interference and laser beam jitter or to perform small scale high speed target maneuvering. The control issue investigated in this thesis will combine disturbance rejection and vibration suppression. This thesis examines cooperative control efforts between the AJTs and a high bandwidth limited authority fast steering tilting mirror platform. The control scenario involves using the AJTs to suppress low frequency large amplitude excitations of the flexible structure to get the beam within the mirror's angular authority, then using the mirror platform for fine position control.

## *1.2 Problem Definition*

In the experimental setup shown in figure 1.1, a tilting mirror platform is mounted at the tip of the truss to simulate a space based pointing platform. A laser beam is directed from a source to a disturbance mirror. The beam is then directed to the control mirror, through a beam splitter, and finally through a cylindrical lens into a lateral axis photodetector. Non-structural optical disturbances are created with the mirror platform mounted on the optical bench. This mirror will be driven by white noise signals to simulate non-structural beam angle disturbances of which the control mirror has no information except the resulting position error at the sensor output. Tip AJTs are used to excite the lower lateral vibrational modes of the truss. The higher structural modes will be excited with a structurally borne reaction mass actuator (RMA). The tip mounted mirror will act as a the control actuator to actively reject structural and non-structural disturbances.

The air jet thrusters are mounted at the tip and the midstation of the truss. The tip thruster is the primary source of structural disturbances while both AJT's will be used as control actuators. Mounting the air-jets at these stations provides the best vibration suppression control of the flexible structure. At these locations occur the largest amplitude disturbances of the first and second modes, excitations which may exceed mirror angle authority.

The linear photodetector acts as a feedback sensor and as the primary measure of system performance. The optical photodetector has high resolution capabilities and performs extremely well at high frequencies. The cylindrical lens focuses the beam

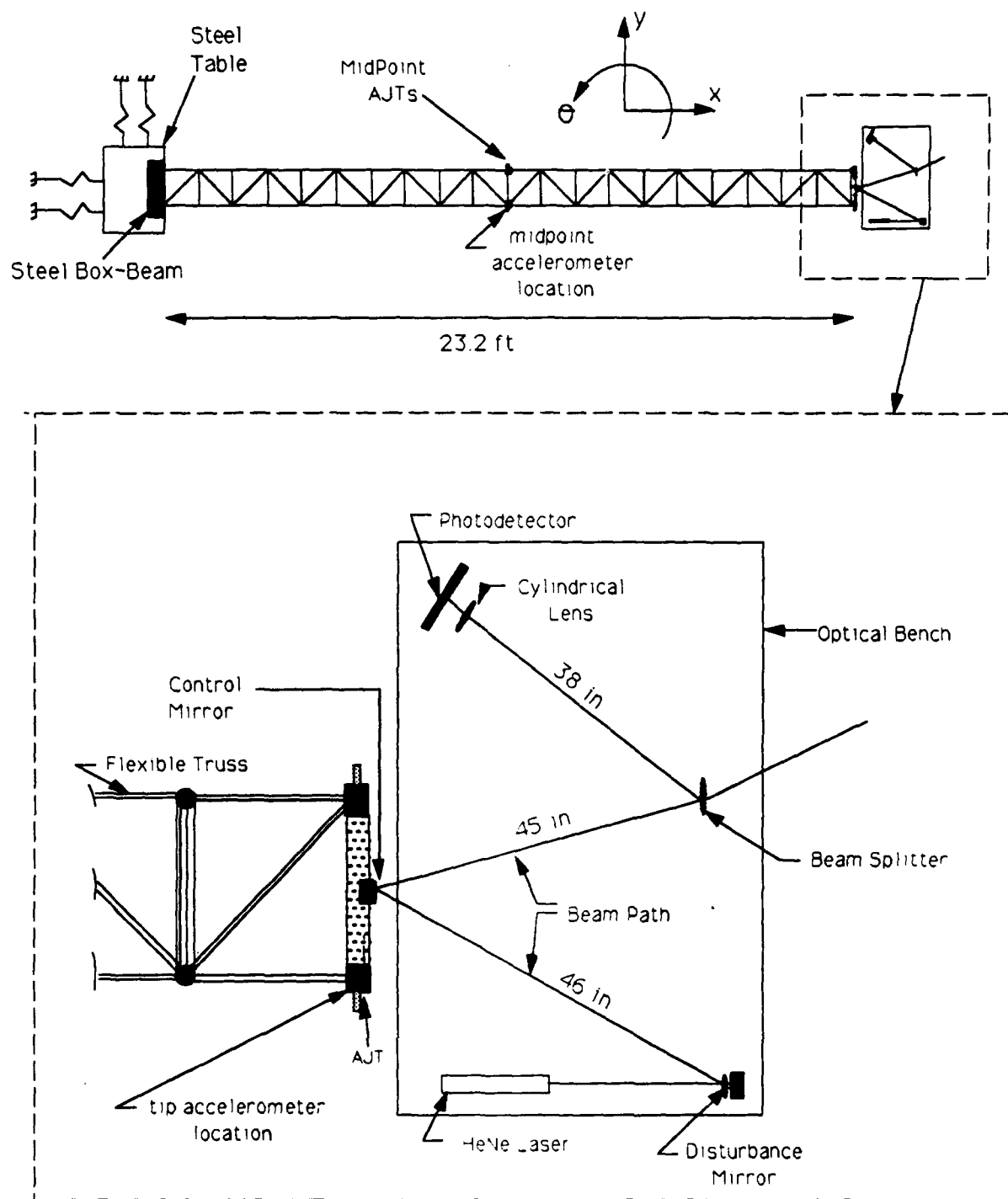


Figure 1.1: Experimental Setup

in the horizontal plane, and removes any out of plane motion. Another sensor is the servo accelerometer colocated with the air jets. The accelerometers measure lateral acceleration of the truss and are used in the feedback control loop with the AJTs for vibration suppression. All control laws for the classical design are implemented on analog computers to facilitate quick changes in control settings and structure. A two input one output dynamic signal analyzer provides data acquisition and analysis capabilities. Figure 1.2 displays a picture of the experimental setup in the University of Washington Controls Lab.

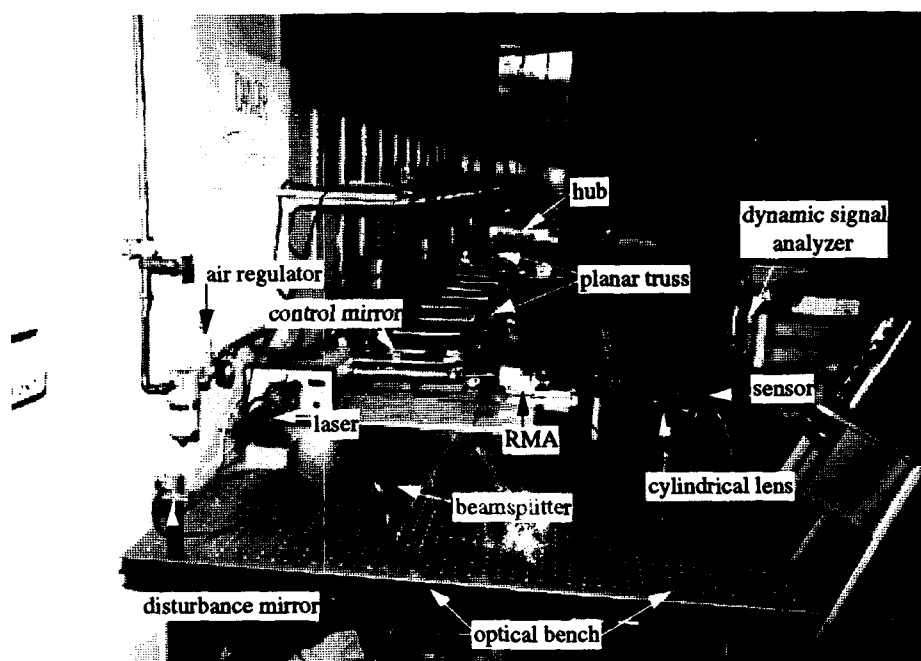


Figure 1.2: Arrangement of Experimental Hardware

### 1.3 Hardware Description

This section describes each hardware component used in this research. A complete concise listing of the optical hardware along with the manufacturer is presented in appendix E. A complete listing of truss and AJT actuator hardware is presented by Shepherd [13].



### *1.3.1 Truss*

The flexible planar truss structure is 23.2 feet long. The root of the truss is constrained by a steel box beam that is rigidly bolted to a heavy steel table which is anchored to the concrete floor. The cantilever structure contains 20 square bays, 1.161 feet on a side and 1.640 feet on the diagonals. Steel ball bearings, 19 mm in diameter, support the truss and allow planar motion with very little friction on small steel plates on the table top. The primary components of the 239 lb truss include aluminum truss members, threaded steel joints, and chordwise steel bars. The steel bars are added to increase the weight of the truss to keep positive contact between the ball bearings, to eliminate out of plane motion, and to reduce the natural frequencies of the structure by increasing its mass. The aluminum members and steel joints are standard components manufactured by the Mero Corporation. The 9.9 lb chordwise steel bars are 16.25×2×1 inches and were manufactured by the department machine shop.

### *1.3.2 Air-Jet-Thrusters*

Two pairs of air-jet-thrusters (AJTs), one mounted at the tip and the other at the midpoint of the truss, can be used to excite the lateral modes of the flexible structure. They can also be used to control the lower two modes of the truss. The primary component of the AJTs is a solenoid valve from Mac Valves, Inc. Model No. 113B 551BAAA. The AJT are non-linear bang-bang actuators driven by on-off triggered circuits. The air source is pressurized shop air regulated to approximately 65 psig.

### *1.3.3 Load Cell*

A MDB 2.5 load cell constructed by Transducer Techniques was used to measure the force output of the AJTs. The load cell was calibrated in compression and has a maximum range of 2.5 pounds. The force gage output is linear to 0.01 percent full scale. A Model TM-2 strain gage transducer amplifier/conditioner module is used to power the load cell and obtain force measurements. To reduce the noise output of the force gage the TM-2 transducer module is equipped with a DC-16 Hz filter. This will cause an appreciative phase lag above the cutoff frequency. The effect of this filter

was considered when the AJTs were modeled and removed from the resulting linear and non-linear AJT model.

#### *1.3.4 Accelerometers*

The lateral excitation of the structure's flexible modes can be monitored by two accelerometers mounted at the tip and mid stations of the truss. The accelerometers are Sundstrand Data Control Model QA-700 servo units. A 30 K $\Omega$  resistor is used to set the sensitivity of the accelerometers to output 38.8 volts/g corresponding to  $9.709 \frac{\text{in/sec}^2}{\text{volt}}$ . The accelerometers were used to deduce the natural frequencies of the truss. They are primarily used in closed loop with the AJTs to provide vibration suppression.

#### *1.3.5 Laser*

The beam source is a 5.0 mW Helium-Neon class IIIb laser obtained from Edmund Scientific. The beam diameter is 0.83mm at the origin and has a 1 mrad divergence. The laser emits a 632.8 nm wavelength red light with random polarization.

#### *1.3.6 Optics*

The optics used in this experiment include two mirrors, a beam splitter, and a planar convex cylindrical lens. One mirror is the Newport Corporation model 10D10, a one inch diameter pyrex mirror with a DM.4 HeNe coating. A smaller mirror, mounted to the control tilting platform, is a stock item from Physik Instrumente. The 15 mm diameter pyrex mirror came mounted to the S-226 tilting mirror platform. The beam splitter is a Newport Corporation model 20B10BS.1, a two inch diameter beam splitter with a general purpose coating for 480-700 nm wavelengths. The cylindrical lens is also a Newport item, model CKX100. The lens is a 50.8 $\times$ 50.8 millimeter square shaped lens with a 100 millimeter focal length.

#### *1.3.7 Piezo Controlled Tilting Mirror*

The tilting mirror platform is a high bandwidth fast steering mirror system. The piezo controlled tilting mirror was used to reject high frequency structural disturbances and

other external beam disturbance. The piezo actuated mirror platform, model number S-226, was designed and built by Physik Instrumente of Germany. The unit consists of a low voltage piezo translator, a 15 mm diameter mirror, and a strain gage bridge attached to the piezo to feed back piezo expansion and contraction. The strain gages are an internal sensor system used in closed loop to maintain a stable absolute position. The piezoelectric translator pushes against a spring flexure which is part of the tilting plate, causing the tilting motion. The mirror is mounted to the truss so that its one tilting axis is orientated with the lateral axis of the flexible structure. The piezo stack is driven by a P-864.00 Piezo Driver-Amplifier allowing the translator to be controlled using a 0-10 Volt external input. An E-808.00 controller module is used to close the control loop with the strain gages. The maximum peak to peak motion of the mirror is 2.2 mrad, which is enough to accomodate high frequency disturbances but not enough to stabilize the beam if the first two modes of the truss are excited to their maximum displacements. The control mirror which is mounted to the tip of the planar truss and its support structure are shown in figure 1.3.

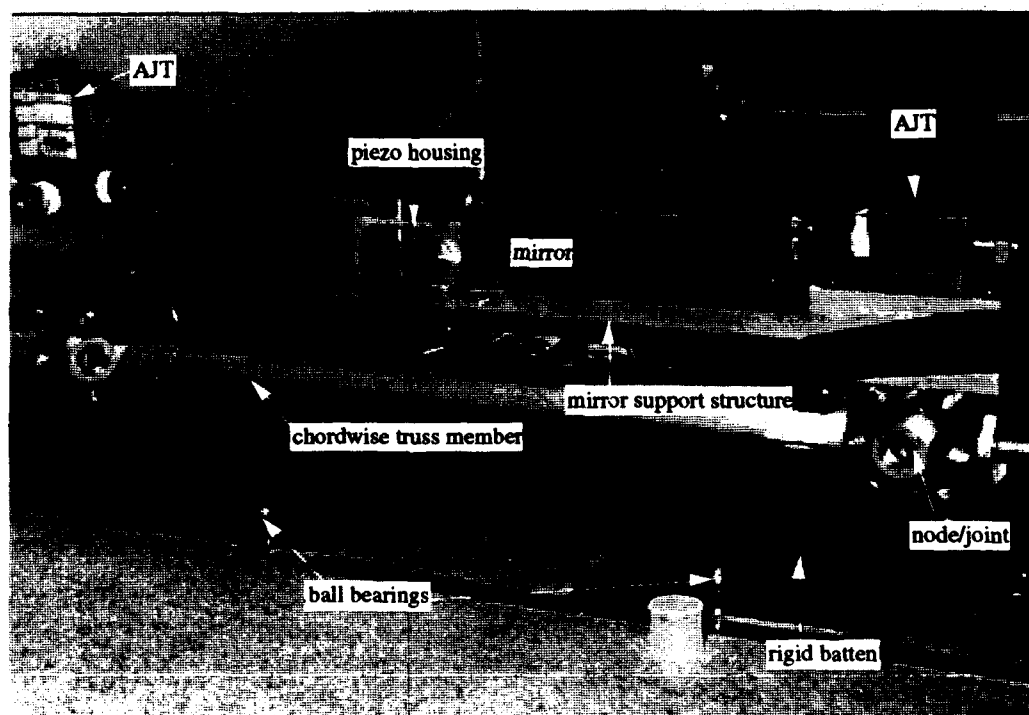


Figure 1.3: Tilting Mirror and Support Structure

Two S-226 tilting mirror platforms were used in this experiment. The 15mm diameter mirror that came with the system was removed from one of the platforms and replaced by the one inch diameter mirror. The procedure is explained in appendix F. This reduces the angular authority and lowers the resonant frequency of the platform in exchange for a larger mirror surface area. The tilting system with the larger mirror was used primarily to inject non-structural disturbances into the beam path.

### *1.3.8 Photodetectors*

Laser beam motion was monitored by a PIN-SL-76-1 optical single-axis position sensor element manufactured by United Detector Technology (UDT). The sensor is an analog optical positioning element accurate to 99.9 percent over 90 percent of its sensing area. The effective sensing area is  $76 \times 25$  mm. Responsivity is 0.6 amps per watt and the noise current for the photodetector is  $0.4 \text{ pA}/\text{Hz}^{\frac{1}{2}}$ . The rise time (10-90 percent) is typically  $30 \mu\text{s}$  while the position detection error is  $76 \mu\text{m}$ . The sensor element is used in conjunction with a Model 301 DIV conditioning amplifier also built by UDT. The amplifier interfaces with the sensor to provide 0 to  $\pm 10$  volt position outputs. A 0-10 volt sum output is also available and provides a measure of sensor illumination.

Similar sensor elements were used at the Air Force Academy by Adams [1]. Strong noise signals with peaks of  $120 + 60 \times N \text{ Hz}$ , where  $N$  is an integer  $\geq$  zero, were noticed in Adam's investigation. The source of the noise was the jitter in the room fluorescent lighting. The Controls Lab at the University of Washington (UW) does not have fluorescent lighting and we expect very little sensor noise. The power spectrum of the darkened photodetector was tested with results shown on figure 1.4 which illustrates the position signal noise peaks at  $60 + 60 \times N \text{ Hz}$ . The position signal noise is 0.0099 volts rms. This value is very small and will have little affect on controller effectiveness.

### *1.3.9 Reaction Mass Actuator*

A reaction mass actuator (RMA) is attached to the tip and was used to excite the fourth and higher vibrational modes of the truss. The RMA was not limited to a 50 Hz bandwidth as was the AJT. The RMA is Ling Dynamics V102 Shaker mounted on an aluminum base which rides on the same type of ball bearing suspension as the flexible

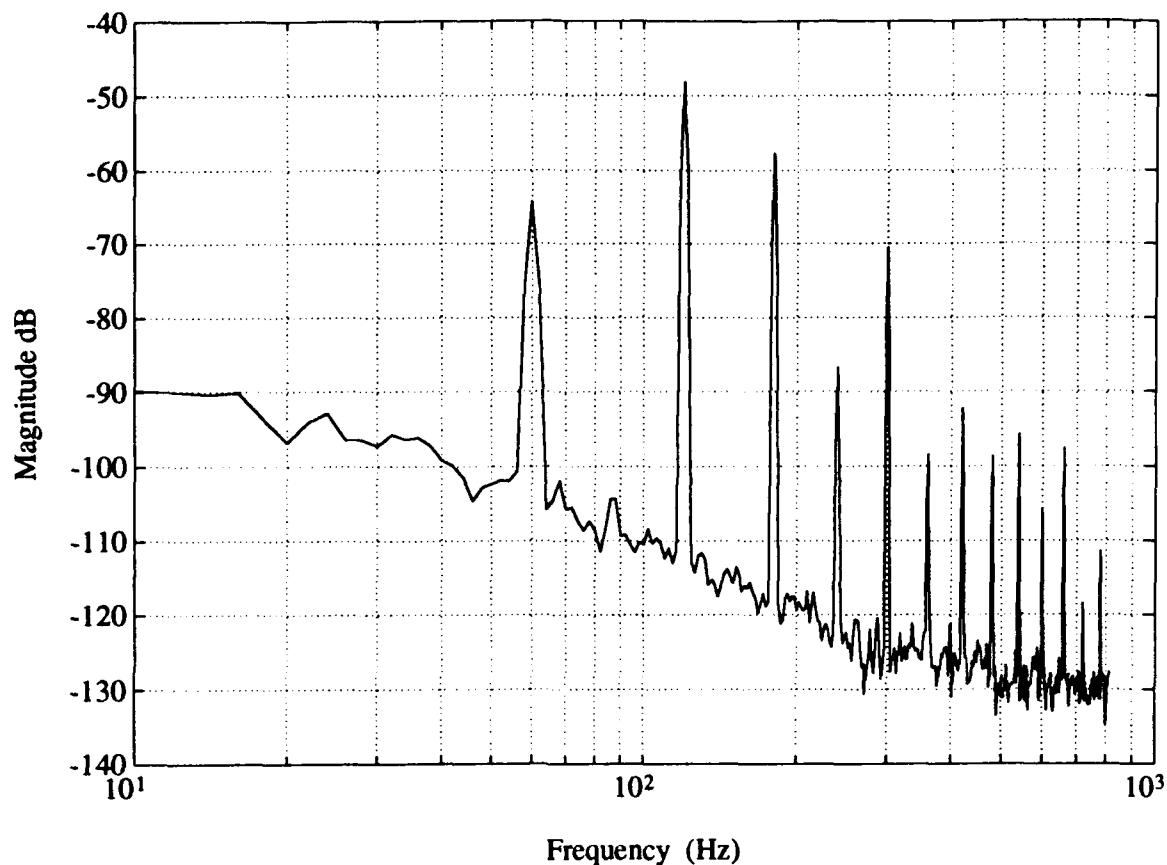


Figure 1.4: Power Spectrum of the Sensor Noise

planar truss. The shaker DC motor is connected to the tip truss node with a stinger. The stinger allows for slight misalignment of the RMA and the flexible truss's lateral motion. The RMA is powered by a model PA35 variable gain amplifier supplied by Ling Dynamics. An accelerometer is rigidly housed to the back of the RMA to sense RMA lateral motion. That accelerometer was not used in the experiment. The addition of the RMA to the truss changes the structure's modal frequencies, as we are essentially adding a concentrated mass to the end of the beam. However, the RMA was only connected and used in this experiment to adequately excite the higher lateral vibrational modes and evaluate the disturbance rejection performance of the mirror controller. The slight changes in truss behavior due to the addition of the RMA need

not be considered in this application. A complete discussion of the RMA and its capabilities was examined by Shepherd in his Master's Thesis [13].

#### *1.3.10 Electro-Mike Position Sensor*

The mode shapes of the truss were measured with a PA 11503 Electro-Mike Displacement Transducer (EMDT) manufactured by the Electro Corporation. The linear range of the transducer is 0.050 to 0.500 inches. The EMDT operates by generating a very low level radio frequency field in front of the sensor which creates eddy currents in any metal target the field intercepts. These induced eddy currents remove energy from the electric field reducing the Quality Factor ( $Q$ ) of the sensor coil. This change in  $Q$  is then translated into a signal output that is proportional to the distance from the target to the sensor. The resistivity of the target metal affects sensor linearity and sensitivity. Magnetic steel, which is used for the rigid truss battens, provides the best linearity, with an error on the order of 0.9 percent of full scale.

#### *1.3.11 Analog Computers*

The Electronic Associates, Inc. EAI TR-20 computer constructed in 1966 and the newer Comdyna GP-6 computer were used to implement the control laws in this experiment. The operations of the two computers are similar. Banana-plug leads and adjustable pots can be used to quickly build circuits on the available operation amplifiers and potentiometers. The linear operating range for the computers is  $\pm 10$  volts. No attempt was made to differentiate between the computers when implementing analog control circuitry.

#### *1.3.12 Dynamic Signal Analyzer*

Data acquisition and analysis was carried out using the Hewlett-Packard (HP) 35665A Dynamic Signal Analyzer. The analyzer is a two channel fast-fourier-transform (FFT) spectrum/network with a frequency range of DC to 100 kHz. The signal analyzer is a general purpose design tool for measurement and evaluation of electronic, electromechanical, and mechanical devices. The HP 35665A is primarily a frequency domain analyzer but can also be used to make time domain and amplitude domain

measurements. The analyzer's measurement capability is extended with the swept sine option. The swept sine mode is used primarily for device characterizations.

#### *1.4 Thesis Overview*

The dynamic characterization of the hardware is discussed in chapter 2. A linear model for each component was obtained. A more accurate non-linear model of the bang-bang AJT actuators was used in SIMULAB [11] to obtain more accurate time domain simulation. Chapter 3 discusses the design and implementation of simple classical control laws for disturbance rejection and vibration suppression. Chapter 3 also provides an extensive validation of the SIMULAB model. Chapter 4 concludes the thesis, summarizing the results and giving directions for possible future work. Appendices are included to explain some of the techniques used to characterize the hardware and set up control circuitry. The appendices also present the required numerical inputs to run the MAPMODES program and SIMULAB model.

## Chapter 2

# SYSTEM MODELING

### 2.1 Overview

System modeling plays an underemphasized role in controller design. Quite often a theoretical model is presented with little information on how it was obtained, the simplifying assumptions made, and how accurate the model is when compared to the actual hardware. The designer spends most of his effort in designing a good controller. However, when the control design is implemented on the hardware, the system often fails and considerable effort is spent modifying the model and controller to obtain satisfactory results. If time were initially taken to accurately model the system, validating the model with hardware before any actual controller design is accomplished, and the controller designed keeping in mind modeling constraints, one would better understand system dynamics and be able to identify and solve controller failures more easily. This chapter is devoted to the development, dynamic characterization, and validation of the flexible optical system model used in this research. The baseline system is composed of a flexible planar truss, a high bandwidth fast steering mirror to be used for fine pointing control and disturbance rejection, and AJT actuators to be used for excitation and control of the flexible structure's lower lateral vibrational modes.

### 2.2 Truss Modeling

Flexible optical systems intended for space use are constructed with light flexible truss assemblies which support the optical components. The planar truss used for this research was constructed in the Department of Aeronautics and Astronautics Controls Lab at the University of Washington. The truss is similar to the one constructed by W. L. Hallauer and S. E. Lamberson at the U.S. Air Force Academy in Colorado Springs, CO [6]. The flexible structure is modeled as a planar truss, constrained



at the base. A piezo actuated mirror and its support structure are attached at the tip. A finite element model (FEM) designed by Hallauer for the United States Air Force Academy (USAFA) truss, was modified to model our structure. Theoretical and experimental validation of the FEM results via beam theory and hardware data was performed on the U.W. structure.

### *2.2.1 The 63-DOF Constrained-Free Finite Element Model*

The most important step in matrix structural analysis is the formulation of a discrete-element mathematical model equivalent to the actual continuous structure [9]. This type of modeling is necessary to construct a model with a finite number of degrees of freedom, since control law design will be based on an ordinary differential equation model of the dynamic system. Furthermore, a low order finite structural model is desired to facilitate control law synthesis. The 63 degree of freedom (DOF) model will be used as a starting point for model reduction. Since the truss is built with discrete elements accurate model formulation poses relatively little difficulty. A truss structure lends itself ideally to analysis based upon algebraic manipulation of matrix equations in which the element forces and displacements may be identified as specific matrices [9].

The finite element model for the planar truss was developed using Matrix Algebra Package/Structural MODES (MAPMODES) developed by Professor W.L. Hallauer of Virginia Polytechnic Institute [4]. The undamped finite element model can be represented in the form of a matrix equation as

$$[M]\ddot{\mathbf{q}} + [K]\mathbf{q} = \mathbf{f} \quad (2.1)$$

where  $\mathbf{q}$  is the vector of generalized coordinates and  $\mathbf{f}$  is the vector of the force and torque inputs for each coordinate.  $[M]$  and  $[K]$  are the consistent mass and stiffness matrices respectively.

MAPMODES performs standard structural matrix algebra operations. It calculates the element stiffness and mass matrices for planar truss, grid, and frame structures consisting of straight one-dimensional structural elements. The element mass and stiffness matrices are assembled into a structure matrix. The structural dynamics eigenvalue-eigenvector solution is included to find the natural vibrational frequencies

and structural modes. A model of the flexible truss structure is shown in figure 2.1.

The actual structure is described in chapter one. The required inputs to MAPMODES for the UWAA planar truss are presented in appendix D.

To predict the natural frequencies and the mode shapes for the finite element model, the free vibration problem is considered

$$M\ddot{\mathbf{q}} + K\mathbf{q} = 0 \quad (2.2)$$

Since free oscillations are harmonic the displacements,  $\mathbf{q}$  can be written as

$$\mathbf{q} = \phi e^{i\omega t} \quad (2.3)$$

where  $\phi$  is the column matrix of the amplitudes of the displacements  $\mathbf{q}$ , and  $\omega$  is the frequency of the oscillations. Substituting into equation 2.2, cancelling the common factors and rearranging leaves

$$[K - \omega^2 M]\phi = 0 \quad (2.4)$$

Equation 2.4 has a non-trivial solution if and only if

$$\det[K - \omega^2 M] = 0 \quad (2.5)$$

Equation 2.5 is the characteristic equation which defines the natural frequencies  $\omega$ . Only for those values of  $\omega$  which solve equation 2.5 will there be a nonzero solution obtained for  $\phi$  in equation 2.4. The number of natural frequencies obtained will be equal to the number of degrees of freedom of the system. The values in the columns of  $\phi$  are the eigenvectors or mode shapes corresponding to each eigenvalue or natural frequency  $\omega$ . Equation 2.4 represents a homogeneous linear set of equations providing relative ratios of  $\phi$ . The mode shapes are normalized to facilitate easier comparisons between experimental and other theoretical results. MAPMODES numerically solves the free vibration eigenvalue-eigenvector problem to find the natural frequencies  $\omega_i$ , and the corresponding mode shapes  $\phi_i$  of the planar truss.

The longitudinal stiffness properties of the truss members, including the effects of the terminal bolt assemblies were measured [6]. As seen in figure 2.1, the hub of the truss is not truly fixed, but constrained by a steel box beam attached to a table,

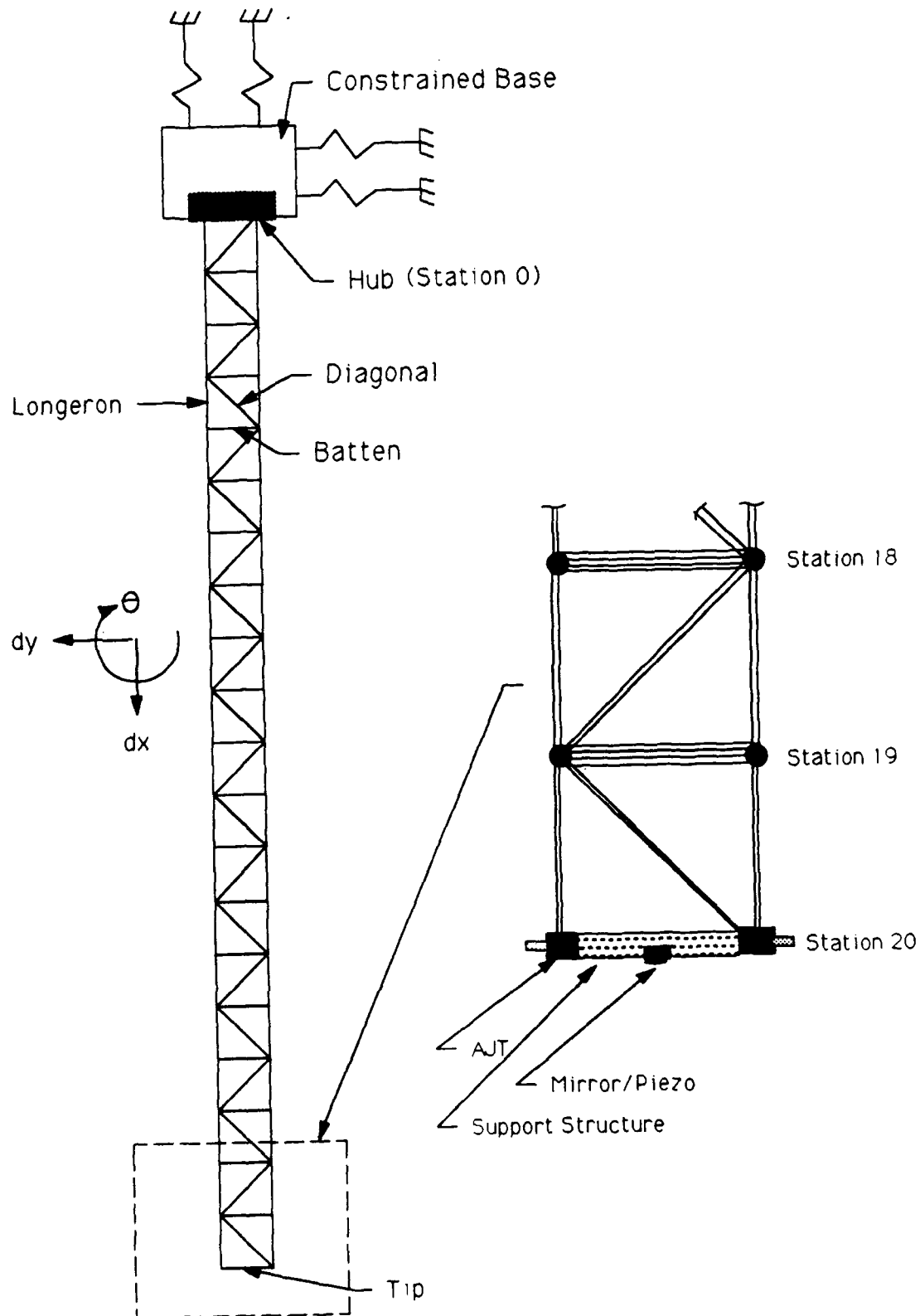


Figure 2.1: 63 DOF Planar Truss

essentially another flexible structure. The table is constructed of steel and is anchored into a concrete floor. The truss at the Air Force Academy is constrained by a similar table [6]. The natural frequencies of the Academy table were measured, and using the known table geometry, and the calculated mass and rotational inertia, the stiffness values for the transverse and longitudinal springs were inferred [6]. Because we did not measure the effect of the box beam on the U.W. truss, its effect is approximated in the mathematical model by using the data obtained by Hallauer at USAFA. The mass and stiffness matrices of the table model in the FEM were lowered significantly to better reflect the effect of the smaller rectangular constraining structure on the UW truss. The effects of the boxbeam were then fine tuned to better match experimental results.

Each longeron and diagonal of the truss is modeled as a simple planar truss element having no bending freedom using standard element stiffness and consistent mass matrices [9]. Each batten is modeled as a rigid bar element, with the masses of the concentrated steel joints and bolt assemblies, the servo accelerometers, the air-jet-thruster actuators, and the mirror assembly and support structure added appropriately to the inertia of the batten elements. Each steel joint is idealized to be rigid. The truss and rigid bar elements are connected at the intersection of their axes. The support table and box beam are modeled as a spring restrained rigid mass connected to the hub batten of the planar structure, station 0. The resulting finite element model has 63 degrees of freedom, three at each of the 21 battens, longitudinal translation  $x$ , transverse translation  $y$ , and rotation  $\theta$ , all about the batten center of gravity.

The finite element model of the constrained-free flexible structure was validated theoretically by simple Euler-Bernoulli beam theory as well as experimental measurements on the actual hardware. Simple beam theory provides a simple method for determining the upper bounds on the natural frequencies. It was used to determine the initial validity of the finite element model. Results of the validations are presented in the following sections and are summarized in table 2.1 and figure 2.3.

### 2.2.2 63-DOF Validation Via Beam Theory and Experimental Hardware

The 63-DOF finite element model for the planar truss was validated analytically via simple Euler-Bernoulli beam theory and experimentally with the hardware. Because of actuator and measurement constraints, only the first four lateral vibrational modal frequencies and the first three mode shapes were measured. In this section we develop the lateral vibrational natural frequencies and mode shapes via beam theory, display the results from the FEM and compare these results to experimental data.

A simple clamped-free Euler-Bernoulli beam is shown in figure 2.2. The partial

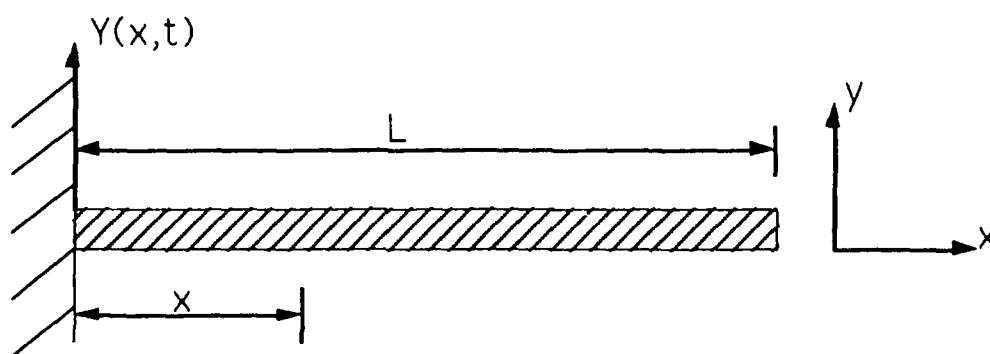


Figure 2.2: Clamped-Free Euler Bernoulli Beam

differential equation of motion governing the beam is

$$\frac{\partial^2}{\partial x^2} \left[ EI(x) \frac{\partial^2 y(x,t)}{\partial x^2} \right] + m(x) \frac{\partial^2 y(x,t)}{\partial t^2} = 0 \quad (2.6)$$

where  $EI(x)$  is the bending stiffness and  $m(x)$  is the mass per unit length. These values are constant for a uniform beam. The equation is based upon the assumption that the material is homogeneous, isotropic and obeys Hooke's law, and that the beam is straight and has a uniform cross section [10]. Equation 2.6 is valid for small deflections and for beams that are long compared to their cross-sectional areas. The effects of shear force and rotary motion are neglected. Their effects are small except when the curvature of the beam is large relative to its thickness; which is true for a beam that is short relative to its thickness or for a beam vibrating in its higher modes where the nodal points are closer together. Since we are dealing with only the first four lateral bending modes these forces can be neglected.

We assume a solution to equation 2.6 to be separable in both time and space,  $y(x, t) = Y(x)g(t)$ . Ordinary differential equations describing the mode shapes (equation 2.7) and the natural frequencies (equation 2.8) are easily obtained.

$$\frac{d^4 Y(x)}{dx^4} - k^4 Y(x) = 0 \quad (2.7)$$

$$\frac{d^2 g(t)}{dt^2} + \omega^2 g(t) = 0 \quad (2.8)$$

where

$$k^4 = \frac{m\omega^2}{EI}$$

and  $g(t)$  is the vector of modal coordinates and  $\omega$  is a vector of the natural frequencies. The problem of determining the values of  $\omega^2$  for which a homogeneous linear differential equation of type 2.7 has a nontrivial solution,  $Y(x)$ , satisfying homogeneous boundary conditions, is termed the eigenvalue problem [8]. The parameters  $\omega^2$  are the eigenvalues and the associated nontrivial solutions  $Y(x)$  are the eigenfunctions.

The four boundary conditions uniquely determine the shape of the solution to equation 2.7 [8]. The boundary conditions for the clamped-free Euler-Bernoulli beam are

$$Y(0) = 0 \quad (2.9)$$

$$\frac{dY(0)}{dx} = 0 \quad (2.10)$$

$$-EI(x) \frac{d^2 Y(L)}{dx^2} = 0 \quad (2.11)$$

$$-\frac{d}{dx} [EI(x) \frac{d^2 Y(L)}{dx^2}] = 0 \quad (2.12)$$

where  $x = 0$  and  $x = L$  are the clamped and free ends of the beam respectively.

The general solution to equation 2.7 is

$$F(x) = C \sinh kx + D \cosh kx + E \sin kx + F \cos kx \quad (2.13)$$

where the constants C, D, E, and F are determined by evaluating equation 2.13 at the boundary conditions. After applying boundary conditions, the frequency and modeshape equations become

$$\cosh kL \cos kL = -1 \quad (2.14)$$

$$\begin{aligned} Y_n(x) = & A_n[(\sin k_n L - \sinh k_n L)(\sin k_n x - \sinh k_n x) \\ & + (\cos k_n L + \cosh k_n L)(\cos k_n x - \cosh k_n x)] \\ & n = 1, 2, \dots, \infty \end{aligned} \quad (2.15)$$

The solution of the frequency equation consists of an infinite sequence of discrete eigenvalues related to the natural frequencies of the beam. To each natural frequency  $\omega_n$  corresponds a characteristic eigenfunction  $A_n Y_n(x)$ , where  $A_n$  is an arbitrary amplitude and  $Y_n$  is a unique mode shape associated with  $\omega_n$  [8]. The normal modes and the associated natural frequencies are dependent on the stiffness  $EI(x)$  and mass  $m(x)$  distributions in the beam as well as the four boundary conditions.

The planar truss is 278 inches long and weighs 239 pounds, giving  $m(x) = 2.237 \times 10^{-3} \frac{(lb_f - s^2)}{in^2}$ . The problem of predicting the natural frequencies and modeshapes becomes one of determining the bending stiffness  $EI(x)$ . The bending stiffness of the truss members was experimentally determined by Hallauer for the Air Force Academy truss [6]. The bending stiffness used was  $EI(x) = 1 \times 10^8 lb_f - in^2$ . The first four lateral vibrational natural frequencies are shown in table 2.1 and the normalized modeshapes in figure 2.3.

The experimental natural frequencies were obtained using the tip AJT and the sensor data from the tip and midpoint servo accelerometers. The structural-borne pair of back-to-back air-jet thrusters at the truss tip were used to excite the truss at frequencies near those initially projected by the finite element model. For each lateral vibration mode, the periodic frequency was adjusted in the vicinity of resonance until the steady state response amplitude of the accelerometer data was a maximum. The air-jets were then turned off to allow the structure to decay freely. A clean decay devoid of any beating or other symptoms of non-modal response indicates that the mode had been excited with reasonable accuracy. These experimental results

Table 2.1: Theoretical and Experimental Lateral Vibrational Natural Frequencies

Mode	Natural Frequencies (Hz)		
	Beam Theory	FEM	Truss Hardware
1	1.53	1.51	1.48
2	9.62	8.89	8.88
3	26.92	23.30	23.32
4	52.71	41.40	41.75

were later verified using the swept sine instrumentation mode of the dynamic signal analyzer.

The measured natural frequencies show close agreement with those predicted by analytical methods. There is less than a two percent discrepancy between the FEM and hardware model for each of the measured natural frequencies. Simple beam theory results, though accurate for the lower modes, begin to lose their accuracy at higher frequencies. Simple beam theory provides us with a convenient method for determining the initial validity of the finite element model. However, ignoring the effects of rotary motion and shear force is no longer a valid assumption at the higher modes.

Figure 2.3 shows the normalized mode shapes of the FEM, simple beam theory, and experimental data. The mode shapes were measured by exciting the truss at a modal frequency with the air-jets and then measuring the peak to peak displacement of the rigid batten at each station of the truss with the position sensor. The data collected were normalized to facilitate easy comparison between experimental and theoretical results. Only the first three mode shapes were experimentally determined. The limited bandwidth of the AJT and the resolution of the Electro-Mike position sensor precluded measuring the fourth mode shape with any accuracy. From figure 2.3, we can see that the normalized mode shapes of the FEM and experimental data match almost exactly. Simple beam theory again provides useable information for the lower modes, but as shear forces and rotary motion effects become more prevalent simple beam theory loses its validity in predicting mode shapes.



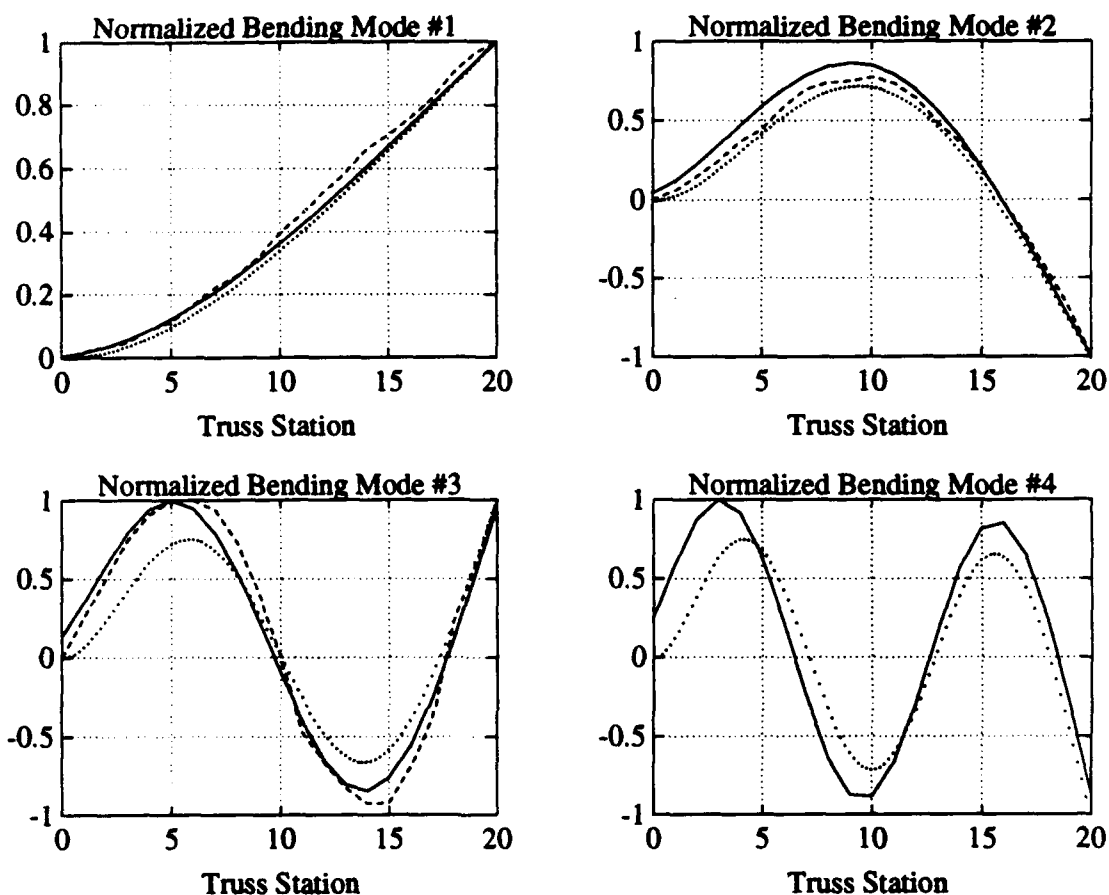


Figure 2.3: Normalized Bending Mode Shapes Comparison: Beam Theory (dotted), Finite Element Model (solid), and Hardware (dashed).

### 2.2.3 Truss Model Reduction

The primary objective in model reduction is to achieve accurate approximations of higher order systems with lower order models. A 63-DOF model is impractical for disturbance rejection and vibration suppression control design and analysis. A low order model that preserves the dynamic characteristics of the full order system is desirable to reduce the complexities involved in designing a working controller. A low order model is easier to work with and allows the designer to develop a controller to handle the truss dynamics of interest. When designing an optimal full state feedback controller the order of the controller will be at least as high as the model order.

Thus a low order model is necessary for any practical implementation of an optimal controller.

The full order model will be reduced to order  $2n_r < 2n$  using a procedure that exactly preserves the dynamic response of the full order model for the  $n_r$  selected DOF and the  $n_r$  selected modes [2]. With this procedure we can reduce the 63 DOF model to a four DOF model, retaining the first four lateral vibrational modes.

The procedure requires that the generalized free vibration eigenvalue problem be solved

$$[M]\ddot{\mathbf{q}} + [K]\mathbf{q} = 0 \quad (2.16)$$

This problem was solved with the MAPMODES program. The vector of the natural frequencies/eigenvalues can easily be made into a matrix of eigenvalues,  $\Lambda$ , where

$$\Lambda = \text{diag}(\omega_1^2, \omega_2^2, \dots, \omega_n^2) \quad (2.17)$$

The corresponding eigenvector matrix,  $\Phi$ , is mass normalized and referred to as the modal matrix

$$\Phi^T M \Phi = I \quad (2.18)$$

The model reduction procedure, known as modal truncation, extracts from the modal matrix  $\Phi$  the  $n_r \times n_r$  reduced modal matrix  $\phi_r$ , where the rows correspond to the  $n_r$  selected degrees of freedom and the columns to the  $n_r$  selected modes [2]. The DOF must be chosen so  $\phi_r$  is non-singular. Similarly we extract from the matrix of eigenvalues the  $n_r$  selected modes. The reduced set of system equations becomes

$$[M_r]\ddot{\mathbf{q}}_r + [K_r]\mathbf{q}_r = \mathbf{f}_r \quad (2.19)$$

where  $\mathbf{f}_r$  is the reduced vector of inputs corresponding to  $\mathbf{q}_r$ . The reduced order mass and stiffness matrices are formed from the reduced modal and natural frequency matrix

$$M_r = \phi_r^{-T} \phi_r^{-1} \quad (2.20)$$

$$K_r = \phi_r^{-T} \Lambda_r^2 \phi_r^{-1} \quad (2.21)$$

Table 2.2: Experimentally Determined Damping Coefficients

Mode	Damping Coefficient ( $\zeta_r$ )
1	0.0120
2	0.0047
3	0.0090
4	0.0160

The planar truss is a lightly damped structure and this damping must be considered to obtain accurate dynamic responses of the truss model. The structural damping of the truss is modeled as linear viscous damping. The effects of the nonlinear coulomb damping caused by the frictional force between the ball bearings and truss structure are not accounted for. Since these frictional forces are low, their nonlinear damping effects will be negligible except at small velocities where nonlinear Coulumb damping is noticeable. This effect shows up primarily in the first mode [6]. Viscous damping can be introduced into equation 2.19 by selecting damping coefficients  $\zeta_r$  for each mode in the reduced order model. These coefficients were experimentally determined for the planar truss by the logarithmic decrement method described in appendix B. The average damping values for the first four lateral vibrational modes are shown in table 2.2.

The modal damping matrix is of the form of

$$[2\zeta\omega] = \text{diag}(2\zeta_s\omega_s) \quad (s = 1, 2, \dots, n_r) \quad (2.22)$$

The reduced viscous damping matrix is

$$[C_r] = \phi_r^{-T} [2\zeta\omega] \phi_r^{-1} \quad (2.23)$$

The final reduced order system model including viscous damping becomes

$$[M_r]\ddot{\mathbf{q}}_r + [C_r]\dot{\mathbf{q}}_r + [K_r]\mathbf{q}_r = \mathbf{f}_r \quad (2.24)$$

This method assumes that the damping does not couple the undamped vibrational modes.

The DOF retained in the reduced order model were chosen on the basis of actuator and sensor location, and controllability and observability of the first four lateral vibrational modes. The tip and midpoint lateral DOF were retained because that is the location of the AJT actuators and accelerometer sensors. The tip and midpoint are selected for actuator location because of controllability and observability issues. The first mode is best controlled and observed at the tip of the structure. The midpoint and the tip are antinodes of the second mode and provide the best opportunity to observe and control the vibration caused by excitation of the second lateral mode. The accelerometers are mounted at the tip and midpoint to provide a colocated feedback control design. The tip rotation,  $\theta_{tip}$ , is retained to simulate rotational motion affecting beam path. Because we wish to retain the first four lateral vibration modes in our model, one more DOF is necessary. The lateral DOF at station number 14 is chosen. This is nearly at the antinode of the third and fourth modes. From experimental and theoretical plots (figure 2.3) of the mode shapes, we can see that the midpoint is a node of the third mode. Observing and controlling the third mode at this point is not feasible.

Structural engineers are most familiar with the form of Equation 2.24. Controls engineers prefer a state-space or transfer function model of the system. The reduced order equation can be made into a multi-input multi-output (MIMO) state-space model

$$\dot{\mathbf{x}} = \mathbf{Ax} + \mathbf{Bu} \quad (2.25)$$

$$\mathbf{Y} = \mathbf{Cx} + \mathbf{Du} \quad (2.26)$$

where  $\mathbf{x}$  are the states corresponding to the retained DOF in the reduced order model,  $\mathbf{u}$  is the vector of the force inputs into the model, and  $\mathbf{Y}$  is a vector of the outputs that the designer specifies.

Equation 2.24 is easily transformed into state-space form by breaking the second order linear equation into two first order equations. The first step is to premultiply by  $\mathbf{M}_r^{-1}$  to isolate the highest derivative,  $\ddot{\mathbf{q}}_r$ .

$$\ddot{\mathbf{q}}_r = -M_r^{-1}C_r\dot{\mathbf{q}}_r - M_r^{-1}K_r\mathbf{q}_r + M_r^{-1}\mathbf{f}_r \quad (2.27)$$

The state vector  $\mathbf{x}$  can now be defined

$$\mathbf{x} = \begin{bmatrix} \mathbf{x}_1 \\ \mathbf{x}_2 \end{bmatrix} = \begin{bmatrix} \dot{\mathbf{q}}_r \\ \mathbf{q}_r \end{bmatrix} \quad (2.28)$$

where  $\mathbf{x}_1$  and  $\mathbf{x}_2$  are each four element vectors corresponding to the specific generalized coordinates and their velocities,  $\mathbf{q}_r$  and  $\dot{\mathbf{q}}_r$ , retained in the reduced order truss model. The resulting linear state equations are

$$\begin{aligned} \dot{\mathbf{x}}_1 &= M_r^{-1}C_r\mathbf{x}_1 - M_r^{-1}K_r\mathbf{x}_2 + M_r^{-1}\mathbf{f}_r \\ \dot{\mathbf{x}}_2 &= \mathbf{x}_1 \end{aligned}$$

Therefore, equation 2.24 is put into final state-space form

$$\frac{d}{dt} \begin{bmatrix} \mathbf{x}_1 \\ \mathbf{x}_2 \end{bmatrix} = \begin{bmatrix} -M_r^{-1}C_r & -M_r^{-1}K_r \\ I_4 & O_4 \end{bmatrix} \begin{bmatrix} \mathbf{x}_1 \\ \mathbf{x}_2 \end{bmatrix} + \begin{bmatrix} M_r^{-1} \\ O_4 \end{bmatrix} \mathbf{f}_r \quad (2.29)$$

where  $I_4$  and  $O_4$  are  $4 \times 4$  identity and null matrices respectively. The C and D matrices are determined by the designer, selecting the output as the motion variables of interest. The numerical values used for the final reduced order model are presented in appendix C.

### 2.3 Air-Jet-Thruster Modeling

The air-jet-thrusters (AJTs) are the primary source of excitation and control of the flexible structure's lower vibrational modes. Theoretical and experimental modeling of AJT's has been previously accomplished by Hallauer at USAFA and Shepherd at the University of Washington [5, 13].

Four AJTs are mounted at the tip and midpoint of the truss in back to back pairs. An AJT operates through the actuation of a solenoid valve. When a control signal is positive the valve is open and thrust is on. Conversely, when the control signal is negative the valve is closed and thrust is off. The bang-bang nature of the actuator

results from the on-off thrust characteristic of the AJT. The air jets are wired such that when one is off the other part of the pair is firing. This is done to permit sinusoidal excitation of the flexible structure and to provide a method for vibration control with the AJT. A circuit diagram of AJT wiring is presented in Appendix A.

### 2.3.1 AJT Theoretical Modeling

The ideal AJT would develop full force immediately after the valve is opened by the control signal. In hardware implementation, however, this is never the case. A rise time delay  $\tau_r$  results as the force of the AJT rises from zero when the control signal is applied to its steady state thrust value. The primary causes of such a delay are from the non-linear effects of pressurized air and the small delay of the electronic circuitry and the valve from the point when the control signal is applied to the point where the valve is fully open. The rise time of the AJT from control voltage input  $e(t)$  to steady state force output  $F_{ss}$  is for simplicity modeled as a second order critically damped system with natural frequency  $\omega_{nAJT}$ . The natural frequency of a second order critically damped system is [3]

$$\omega_n = \frac{6}{\tau_r} \quad (2.30)$$

where  $\tau_r$  is the time required for the system to reach 95 percent of its steady state value when subjected to a step input. The relationship between the input control signal  $e(t)$ , and the output force  $F(t)$  is

$$F(t) = F_{ss} \text{sgn}[e(t)] [1 - \exp(-\omega_n(t - sw(t)))(1 + \omega_n(t - sw(t)))] \quad (2.31)$$

where the function  $sw(t)$  is defined as

$$sw(t) = t \text{ when } e(t) = 0 \quad (2.32)$$

and

$$\begin{aligned} \text{sgn}[e(t)] &= 1, & e(t) &> 0 \\ \text{sgn}[e(t)] &= -1, & e(t) &\leq 0 \end{aligned} \quad (2.33)$$

The transfer function form of the second order rise time delay filter is

$$G_{r_r}(s) = \frac{F_{ss}\omega_n^2}{(s + \omega_n)^2} \quad (2.34)$$

A new pulse is initiated whenever the control signal passes through zero in the direction of the control signal. The force acts in the positive direction when the control signal is greater than zero and in the opposite direction when the signal is less than zero. The switching function  $sw(t)$  was realized in hardware with transistors and high gain operational amplifiers (OP-AMPS). The circuitry for each pair of AJTs is setup such that a positive signal will cause one AJT of the pair to fire and conversely a negative control signal will cause the other jet to fire while simultaneously causing the first air-jet valve to close. A complete description of the wiring schematic for the AJTs is presented in Appendix A. The relationship between the control signal and rise time of the AJT is illustrated in figure 2.4.

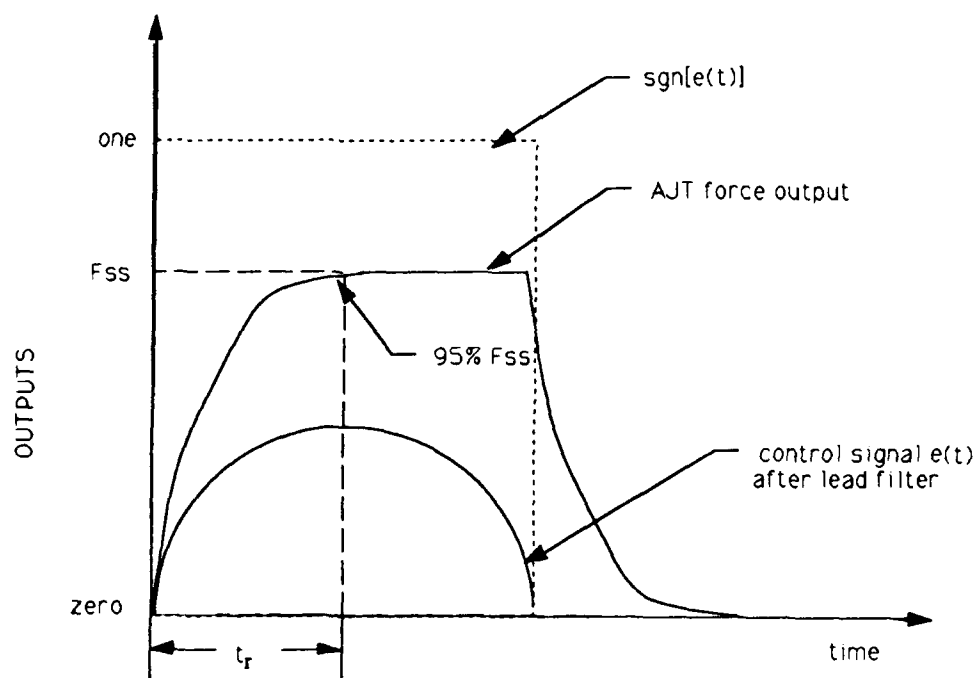


Figure 2.4: AJT Signals

Equation 2.31 approximates the magnitude of the output force of the air-jet

thruster. However, it is not possible to relate the force of the AJT thruster to the magnitude of the input switching signal  $e(t)$ . Because of the non-linear nature of the solenoid valve and transistors, a control signal of 0.1 volts will produce the same output force as a 10 volt input. Despite this inherent limitation a linear transfer function relationship was determined for use in initial design analysis and is discussed in section 2.3.2.

The phase of the AJT is much easier to describe. As proposed by Shepherd [13] the phase lag associated with the rise time delay is described with a second order system transfer function

$$\phi_r = \angle \frac{F_{ss}\omega_n^2}{(j\omega + \omega_n^2)} \quad (2.35)$$

An additional factor that affects the phase relationship of the AJTs is not a result of the air-jet dynamic operation. A low bandwidth lead filter is implemented in the electronic circuitry of the AJT thruster to prevent stray DC voltages from inadvertently causing the AJTs to fire. A complete description of the filter is presented in the Appendix A. Only the results of the analysis will be presented here. The lead filter is described by the transfer function

$$G_{LF}(s) = \frac{0.5s}{s + 1.5} \quad (2.36)$$

Combining the phase affects of the rise time and the lead filter yields

$$\phi = \phi_r + \phi_{lf} \quad (2.37)$$

Many linear algebra matrix packages work best when the roots of a system are ordered. For convenience we depart slightly from achieving critical damping for the AJT time delay filter (equation 2.34) and offset the filter poles slightly. To do so equation 2.34 becomes

$$G_{tr}(s) = \frac{F_{ss}\omega_n^2}{(s^2 + 2\zeta\omega_n s + \omega_n^2 - n)} \quad (2.38)$$

where the damping ratio  $\zeta$  will be just less than one. Equation 2.38 separates the poles of the rise time filter with negligible affects on the phase characteristics of the AJTs as long as  $\zeta$  is approximately equal to one.



The non-linear block diagram used in SIMULAB to determine initial design effectiveness is

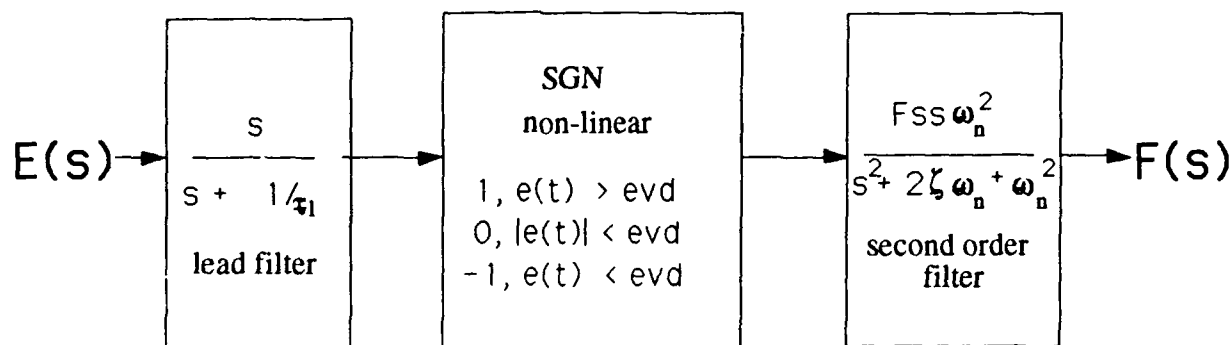


Figure 2.5: Non-Linear Block Diagram for AJT Model

Though not part of the AJT dynamics, a dead zone was designed into the AJT circuitry (Appendix A) to properly implement the velocity feedback controller for the AJTs. The controller is described in Chapter 3. The dead zone is implemented with the OP-AMPS in the AJT circuitry and cannot be separated from AJT operation. Therefore, the small dead bandwidth is included in both open and closed loop simulation. The dead zone was found to have little effect on open loop AJT performance. The lead filter implemented in the non-linear block diagram shown in figure 2.5 is not the same as the lead filter presented in equation 2.36. The dead zone was implemented in hardware taking into account the lead filter's control magnitude reducing effect. In the hardware, the lead filter and OP-AMPS combine to form the dead zone. In SIMULAB these entities are made separate for ease in programming and the change has no effect on either open loop or closed loop operation. That is why there is no longer a 0.5 in the numerator of the filter. See Appendix A for a complete explanation of the AJT control circuitry.

### 2.3.2 Experimental Validation of AJT Model and Linear Model Development

Validation of the theoretical model of the AJT was performed by Mike Shepherd and myself at the University of Washington [13]. A quick-run through of the experimental method and an analysis of the results are presented here for completeness.

An AJT is placed in a test jig attached to a load cell for measuring the output thrust. The test jig is shown in figure 2.6. The signal analyzer was used to inject a sinusoidal control signal to the AJT. Though the signal to the jet was sinusoidal, the control signal affected the thruster as a square wave would because of the on-off nature of the AJT. The rise time delay for the air-jets were measured by comparing the output force time responses from the load cell to the periodic control signal sent to the solenoid.

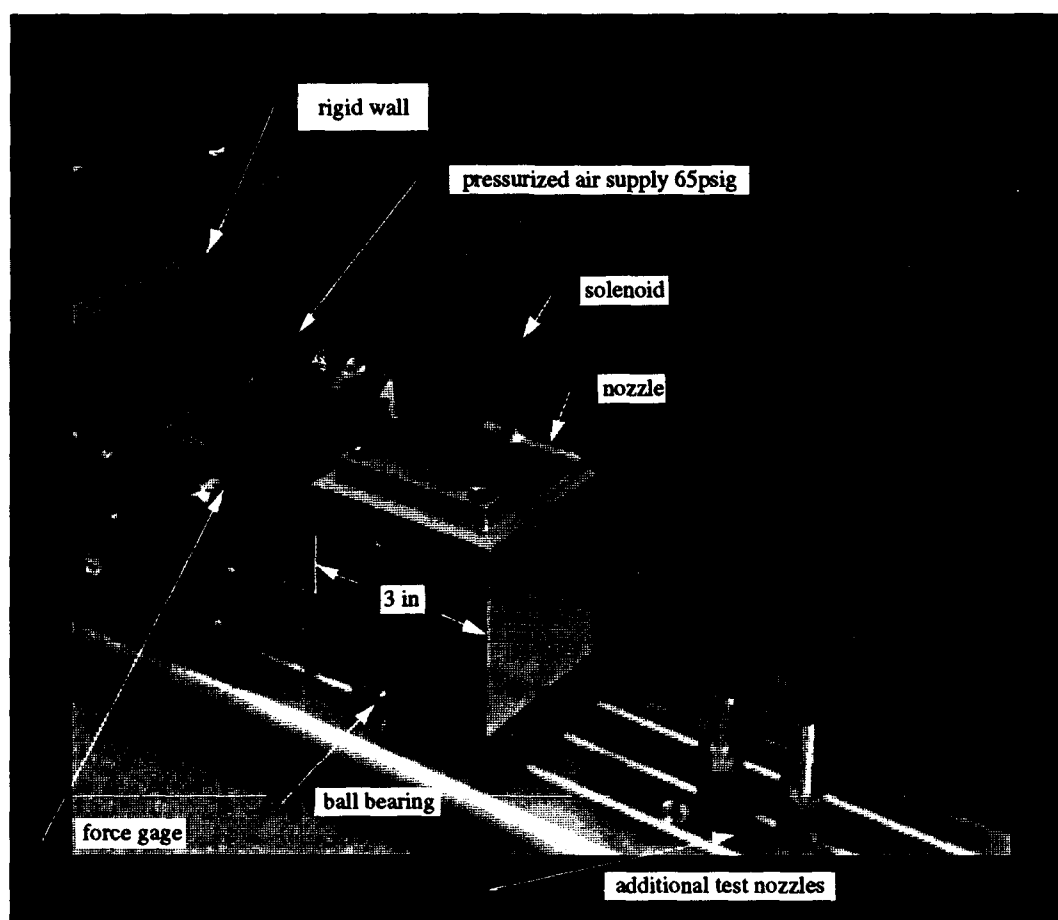


Figure 2.6: AJT Test Jig

The test jig configuration allows for the measurement of the air-jet thrust when the solenoid is opened by the periodic electronic control signal  $e(t)$ . The rise time delay  $\tau_r$  of the AJT was measured by comparing the output time response of the AJT

to the square wave power signal to the solenoids from the transistors. The control input signal is a periodic sinusoid and the square wave results from the switching action of the transistors as the AJT is turned on and off.

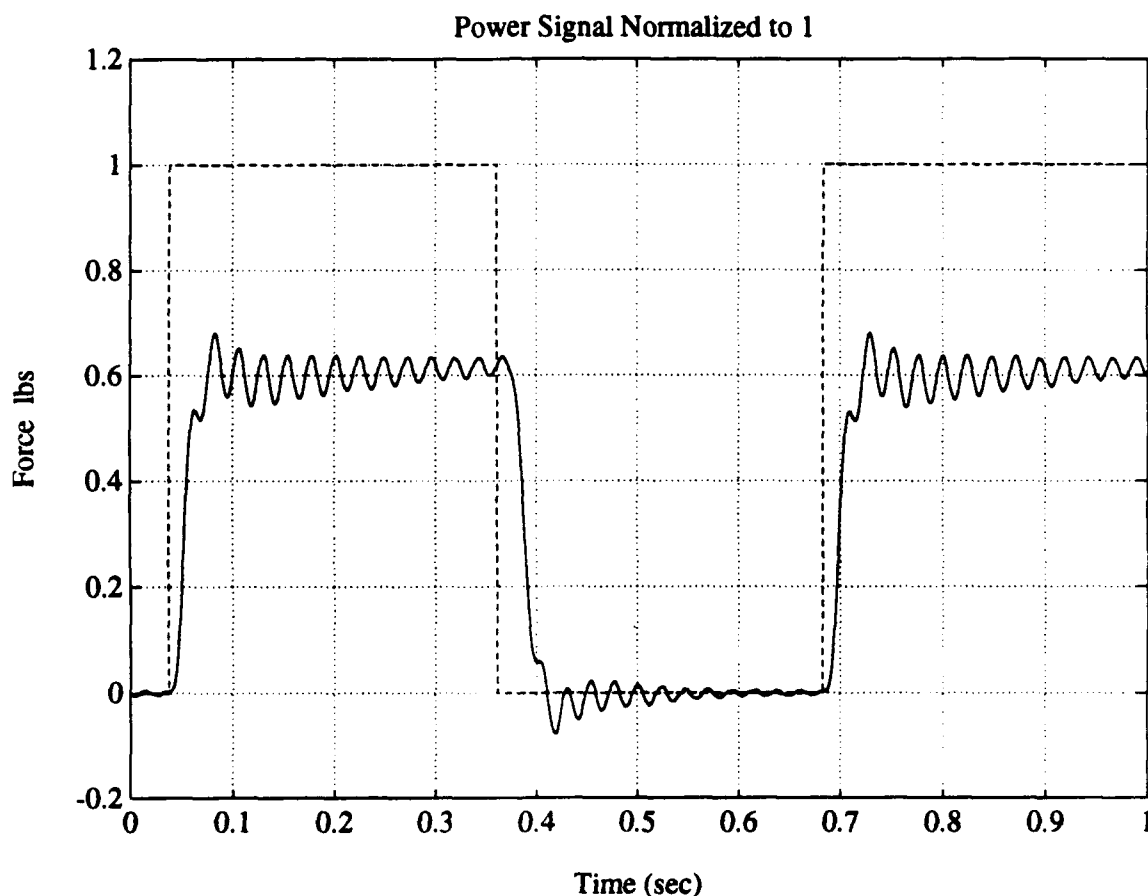


Figure 2.7: Experimental Data: Normalized Transistor Power Signal (dashed) Load Cell Data (solid)

Data was taken at many frequencies within the limited 0-50 Hz bandwidth of the AJT. A typical experimental plot is shown in figure 2.7. The input signal to the AJT circuit for this plot was a 1.55 Hz sine wave. The load cell was calibrated to produce -1 volt output for a one pound compression force. The steady state force output was 0.6  $lb_f$ . The average measured rise time constant for the AJT was  $\tau_r = 30ms$ . The rise time was defined as the amount of time required for the AJT to reach 95 percent

of its steady state force output after the control signal was applied to the transistors. The natural frequency for the rise time filter is then easily found using equation 2.30. The filter natural frequency is  $\omega_n = 200\text{ms}$ .

A frequency response plot of the AJT was obtained by exciting the AJT control circuit with white noise from the signal analyzer. The random noise signal was set to one volt peak input and spanned a range of 1 to 50 Hz. The fast fourier transform of the output was taken to obtain the plots shown in figure 2.8.

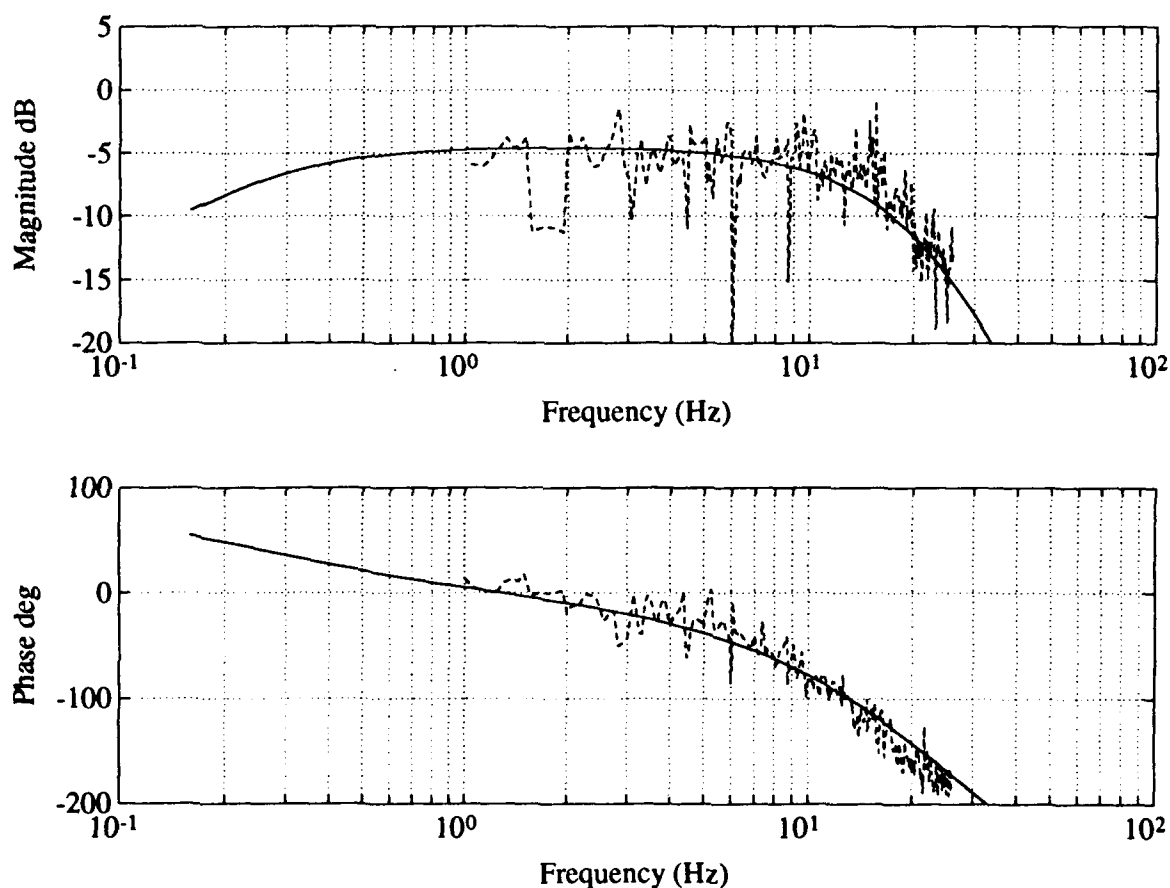


Figure 2.8: AJT Theoretical(solid) and Experimental(dashed) Normalized Frequency Response

The magnitude portion of the frequency response plot was scaled so that one volt input equals the  $0.6\text{ lb}_f$  steady state force output. This scaling is arbitrary and was

done for convenience as the output force of the AJT is independent of the control signal magnitude as long as the small control dead zone is overcome. The shape of the magnitude plot confirms the validity of the theoretical model. It is of importance to note that the first order behavior of the force gage filter is reflected in the experimental data and is added to the theoretical plot to maintain validity. The frequency response provides us a gage of the effectiveness of the AJT when used to excite and possibly control the first four lateral modes of the planar truss. The AJTs are effective for the first two bending modes which lie below 10 Hz. For the higher lateral modes the time delay associated with the AJTs reduces the effective bandwidth and prevents them from adequately controlling high frequency vibrations.

The phase plot shown in figure 2.8 is fortunately easier to compare to the theoretical results. The AJT phase relationship is shown in equation 2.37 and does not have the scaling problems associated with the magnitude plot. The experimental phase response matches theoretical modeling very well. Again it is important to note that the theoretical phase plot also includes the effects of the second order force gage filter present in the experimental data.

A completely linear transfer function model of the AJTs is developed from the frequency response plots shown in figure 2.8. A third order model is used to reflect the theoretical development of the rise time filter and the lead filter developed in section 2.3.1 and Appendix A respectively. A linear model is obtained by combining the lead filter and the second order rise time filter model and then using the appropriate scale factors to make a one volt input equal to 0.6 lb<sub>f</sub>. The resulting linear transfer function from AJT force output to control signal input  $\frac{F(s)}{E(s)}$  is

$$\frac{F(s)}{E(s)} = \frac{F_{ss}\omega_n^2 s}{(s + 1.5)(s^2 + 2\zeta\omega_n s + \omega_n^2)} \quad (2.39)$$

where  $\zeta$  is chosen to be 0.95 to order the roots.

The model described by equation 2.39 cannot be used to design a controller for the AJTs using linear techniques. The results would be misleading and most likely not realizable in the hardware. However, the linear model of the AJTs can be used to assess the performance of other controllers implemented on the UWAA planar truss. The AJTs are used to excite the truss and as an input port for white noise. Experimental data may be scaled against open loop responses of the linear model

and compared to closed loop data using the same scaling. The linear model was primarily used for frequency response comparisons to provide an initial insight into the feasibility of the linear controller designed for the tilting mirror. The development of the mirror controller is detailed in chapters 3. The input/output relationship obtained from figure 2.8 is useful for determining the rise time filter validity and the development of a linear model for use in initial closed loop design for other control actuators, but one must consider the obvious magnitude scaling problems when using the linear transfer function model (equation 2.39). Accurate time domain simulation may only be achieved using the AJT non-linear block diagram shown in figure 2.5 which takes into consideration the non-linearities inherent in the AJTs.

#### 2.4 Piezo Actuated Mirror Modeling

The first step in modeling the mirror-piezo plant is to analyze the physical properties of the system and define the basic mathematical relationships. The system has a resonant frequency of 9 kHz, well beyond the range of interest in this experiment. A schematic is shown in figure 2.9.

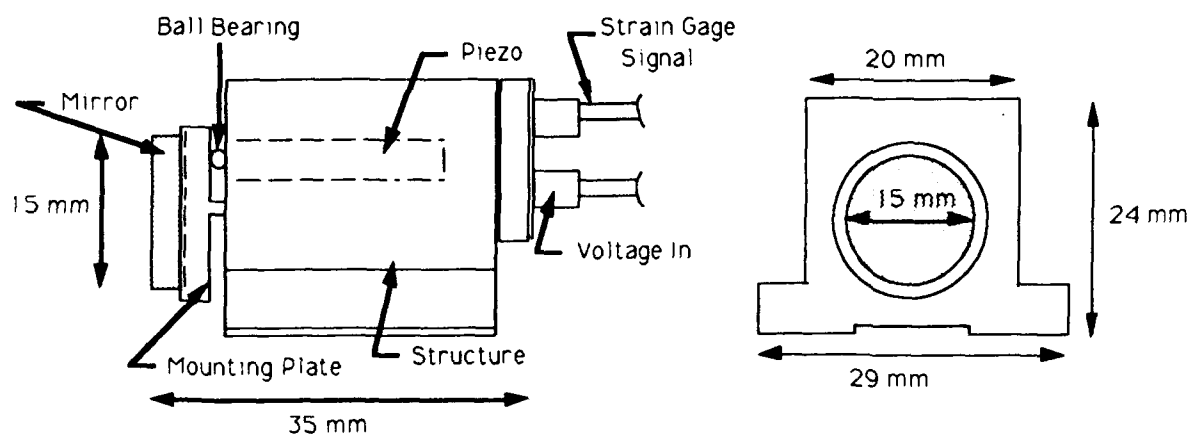


Figure 2.9: Mirror-Piezo System

The pyrex mirror is attached to an invar mounting plate with a thermal adhesive. The mounting plate is then attached to the piezo housing structure as shown in figure 2.9. Invar is a flexible metal and is used to allow the piezo to easily deflect the

mirror without any overshoot. The mirror can be tilted in one axis about its centroid by the low voltage ceramic piezo stack. Since the piezo stack is extremely susceptible to damage from shear forces a small ball bearing is placed between the housing and the mounting plate to keep those forces to a minimum. The piezo expands and contracts as the supply voltage from the amplifier is increased and decreased respectively. The piezo is fully contracted at zero volts while maximum expansion of the piezo occurs at 100 volts. The amplifier output to piezo voltage input transfer function,  $V_{amp}(s)/V_{piezo}(s)$ , can be considered a gain of 10. This limits the control input to lie between zero and ten volts.

The calibration data was supplied by the manufacturer and verified in the lab. The mirror, with the strain gage sensor loop closed, has a resolution of 10  $\mu$ rad. The tilting angle of the mirror increases linearly at a rate of 0.22 mrad per volt up to a peak tilt of 2.2 mrad for a 10 volt control signal. The dynamic behavior of the plant comes from the mirror mounting plate. The plate acts as a stiff spring and is the only source of damping for the platform. The transfer function from the amplifier control voltage input to the mirror angle output in milliradians for the tilting mirror platform takes the form of a second order spring-mass-damper system with very high damping.

$$\frac{\Theta_{mirror}(s)}{V_{control}(s)} = \frac{K_m \omega_m^2}{s^2 + 2\zeta_m \omega_m s + \omega_m^2} \quad (2.40)$$

An optical gain from the mirror angle to the beam angle present in the system as the angle of incidence is equal to the angle of reflection.

$$\Theta_{beam} = 180^\circ - \Theta_{incidence} - \Theta_{reflection} = 180^\circ - 2 \times \Theta_{incidence} \quad (2.41)$$

As the angle of incidence is changed by  $\Delta$ , the beam angle changes by  $2 \times \Delta$  and therefore, a gain of 2 between the mirror angle and the beam angle results.

#### 2.4.1 Experimental Validation of Tilting Mirror Platform

Experimental validation of the tilting mirror platform transfer function (equation 2.40) was performed using the swept sine mode of the dynamic signal analyzer. The primary objective of the swept sine test is to characterize the gain and phase of a test device by measuring only the fundamental component of the input signal and only

the fundamental component of the output signal. Swept sine data is updated point by point as the analyzer measures spectral energy at discrete frequencies. A one volt peak analyzer input was sent to the piezo amplifier and the corresponding beam motion was measured on the photodetector. The integration time was 5 cycles as was the settling time. The measurements from 10 to 100 hz were taken as the analyzer performs a 201 point logarithmic sweep.

The piezo amplifier was preset to 50 volts in order to position the mirror for a  $\pm 1.1 \text{ mrad}$  throw corresponding to a  $\pm 5$  volt signal input. This prepositioning of the piezo element is necessary to prevent damage to the piezo from negative voltage signals and enable the mirror to tilt both left and right. Most control signals combine positive and negative outputs and the optical photodetector senses positive and negative positions in relation to the center of the element (zero volts). The prepositioning was used throughout the experiment.

Figure 2.10 displays the comparison of the experimental transfer function to the theoretical model. The parameters used for the theoretical model are  $K_m = 0.22$ ,  $\omega_m = 2300 \times 2\pi \text{ rad/sec}$ , and  $\zeta_m = 0.9$ . The linear theoretical model compares very well with hardware as expected. Damping of the system is high as is seen by the lack of any peaking near the cutoff frequency. The tilting mirror has an effective bandwidth of over 1000 Hz which should be more than enough to handle any high frequency disturbance of interest.

## 2.5 Disturbance Mirror Characterization

The disturbance mirror platform characterization was accomplished to provide a suitable model for simulation. The same method used to characterize the control mirror was incorporated for the disturbance mirror platform. The small 15 mm diameter mirror was removed and replaced with a larger 1 inch diameter mirror to reduce the likelihood that the beam would oscillate off the mirror face. The static tilt of the mirror was determined to be 0.141 milliradians per volt. However, hysteresis was introduced. The piezo was not effective at control inputs below 4 volts. The effective input voltage range had been reduced from 0 to 10 volts to 4 to 10 volts. This does not pose any problem when using the platform as a source of beam path disturbance, as the mirror can be preset to 70 volts on the amplifier and controlled using  $\pm 3$



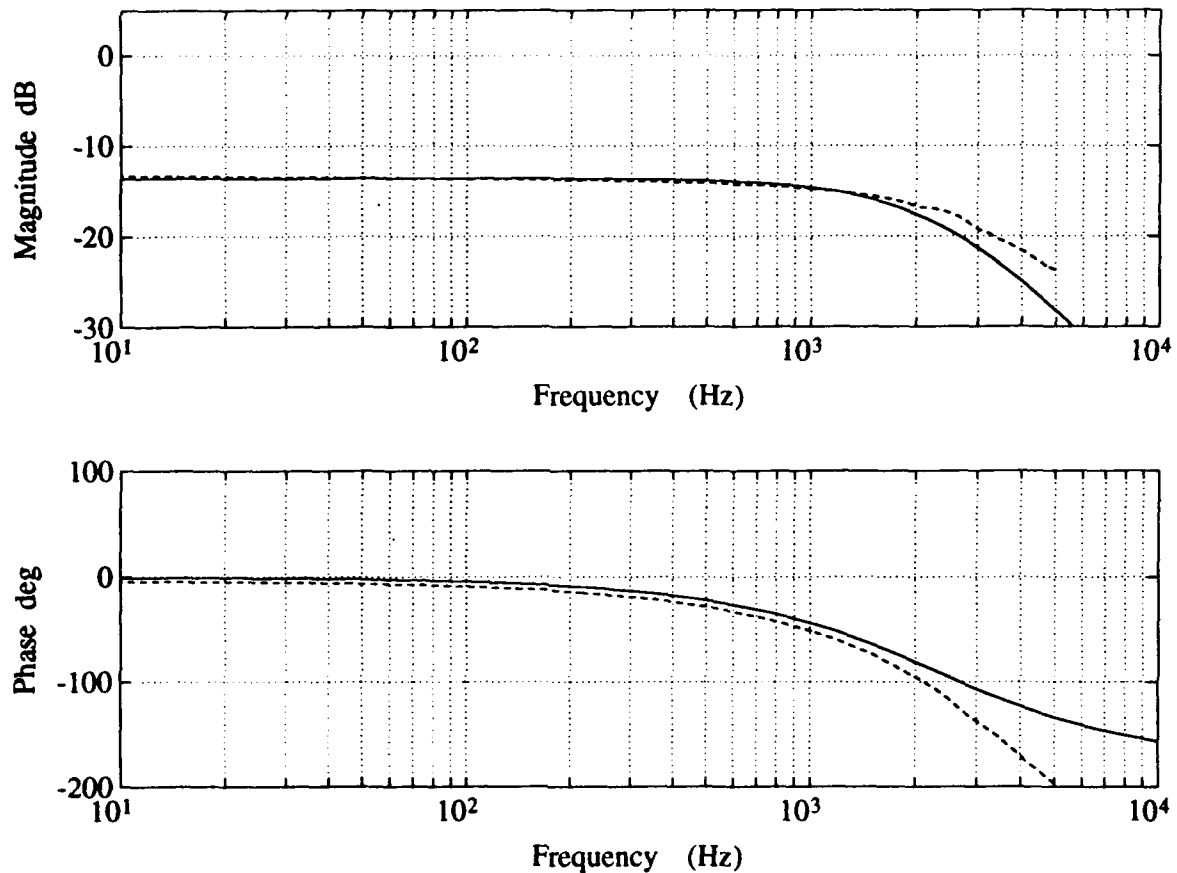


Figure 2.10: Experimental (dashed) and Theoretical (solid) Control Mirror-Piezo Tilting Platform Transfer Function ( $\frac{\Theta_{\text{mirror}}(s)}{V_{\text{control}}(s)} \frac{\text{mrad}}{\text{volt}}$ ).

volt control signals. However, if the mirror were to be used as control actuator the larger mirror should be replaced with a mirror with nearly the same dimensions as the original mirror. The advantage obtained with a larger mirror surface does not compensate for the loss in tilting authority and the introduction of hysteresis.

The disturbance mirror was characterized using the same method described in sections 2.4 and 2.4.1. The mirror platform control voltage was preset to 60 volts and a sine sweep from 10 to 5000 Hz using a 1 volt peak input level was performed. The linear transfer function governing the disturbance mirror model is

$$\frac{\Theta_{mirror}(s)}{V_{control}(s)} = \frac{K_m \omega_m^2}{s^2 + 2\zeta_m \omega_m s + \omega_m^2} \quad (2.42)$$

The experimentally determined parameters for the disturbance mirror tilting platform were  $K_m = 0.141$ ,  $\omega_m = 1700 \times 2\pi$  rad/sec, and  $\zeta_m = 0.45$ .

## Chapter 3

# CLASSICAL CONTROLLER DESIGN

### 3.1 Overview

The primary focus of this chapter is the design and evaluation of the effectiveness of classically designed controllers to reduce the effects of disturbances on an optical beam path. A small high bandwidth tilting mirror was used to reject both structural and non-structural disturbances to properly position a laser beam on a target. Often, after a high speed large angle slew or impact with floating space debris, the first and/or second vibrational modes of the truss structure are excited beyond the throw of the control mirror. These large amplitude vibrations must be significantly reduced before the mirror can be effective. The use of AJTs to increase the inherent damping of the planar truss is explored.

A mathematical synthesis model combining the individual elements modeled in Chapter 2 was created and evaluated against the experimental hardware. The design, theoretical analysis, implementation, and experimental evaluation of a proportional-integral (PI) controller for the tilting mirror platform was accomplished. Bandwidth, actuator limitations, noise, and robustness issues were examined. The tilting mirror has a limited throw and the use of AJT control actuators was necessary to increase the inherent structural damping of the lower two modes of the planar truss. A velocity feedback controller was implemented with the AJT to eliminate large amplitude low frequency structural vibrations. The mirror and air-jet controllers were then combined; using the AJTs to quickly dampen first and second mode vibrations and once within range of the tilting mirror, switching to the mirror platform for fine pointing control.

### 3.2 Open Loop Synthesis Model

The SIMULAB [11] block diagram model was the primary theoretical tool for gaging controller performance. This section discusses the construction and open loop validation of the SIMULAB model. Because of its non-linear capabilities, the SIMULAB simulation model enables one to closely match the characteristics of the experimental hardware, providing the designer with accurate simulation data prior to the implementation of control designs on hardware. Spending the time developing and validating the synthesis model helps the designer develop a good controller before hardware implementation and provides a baseline model useful in future design work. A discussion of the elements of the simulation model and its validation follows in sections 3.2.1 and section 3.2.2.

#### 3.2.1 SIMULAB Model Development

SIMULAB is a general purpose mathematical time domain simulation package which allows modeling of non-linear as well as linear aspects of the hardware. The modeling and characterization of the hardware was discussed in chapter 2. This section presents the numerical inputs required to run the SIMULAB simulation and describes any of the SIMULAB blocks not previously discussed in this thesis. All the numerical values required to use SIMULAB are presented in this section and Appendix C for easy reference.

Figure 3.1 shows a block diagram for the open loop simulation model used in SIMULAB. Table 3.1 displays the outputs of the truss and the corresponding units.

The linear truss model can be described by a set of state equations

$$\begin{aligned}\dot{\mathbf{x}} &= \mathbf{A}_r \mathbf{x} + \mathbf{B}_r \mathbf{u} \\ \mathbf{Y} &= \mathbf{C}_r \mathbf{x} + \mathbf{D}_r \mathbf{u}\end{aligned}\tag{3.1}$$

where  $\mathbf{x}$  and  $\mathbf{Y}$  represent the state and output vectors respectively and  $\mathbf{u}$  is the vector of force inputs corresponding to the retained degrees of freedom in the reduced order model. The numerical values for the state matrix  $\mathbf{A}_r$  and input matrix  $\mathbf{B}_r$  retained from the full 63-DOF model developed in MAPMODES are presented in Appendix

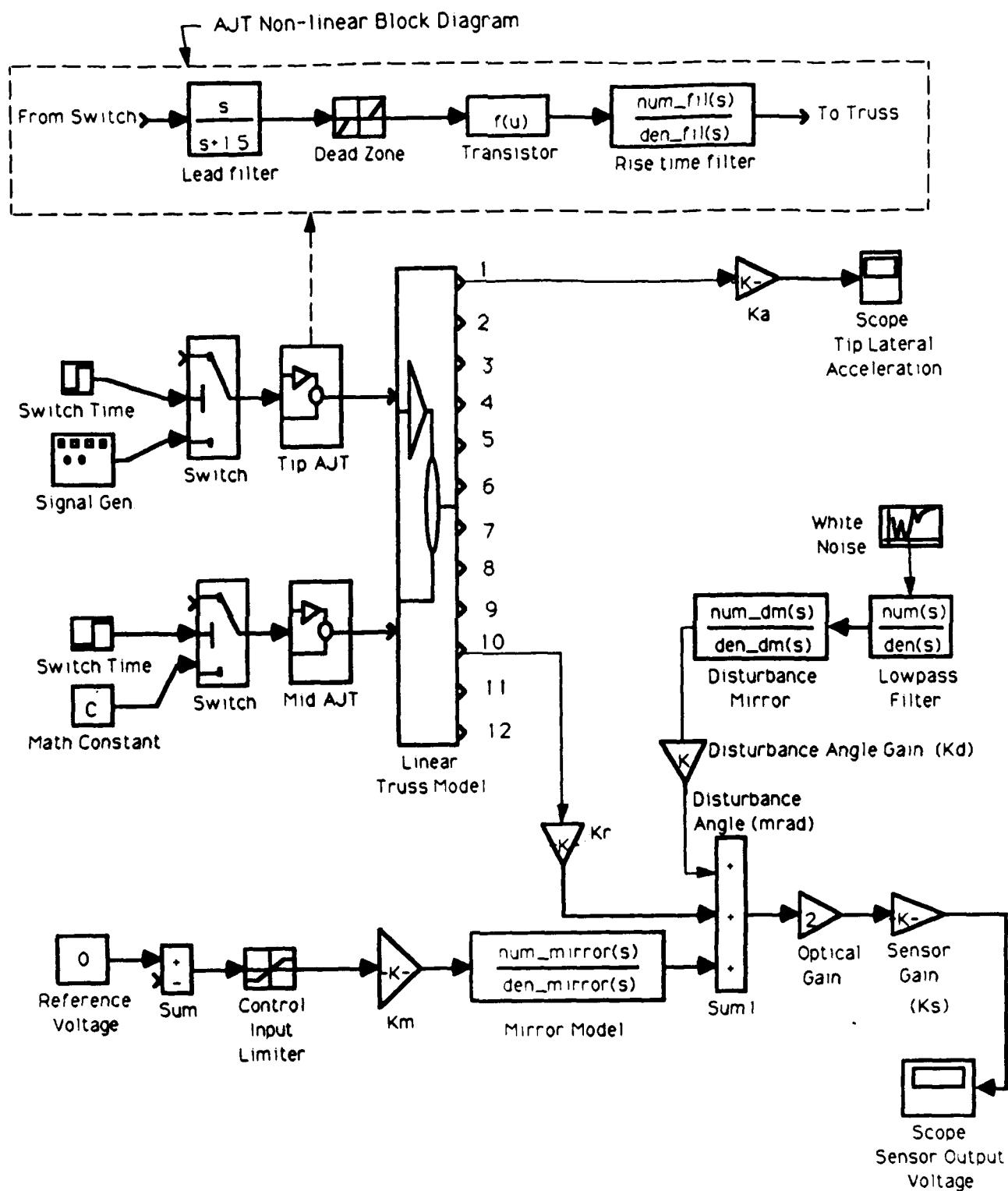


Figure 3.1: Open Loop SIMULAB Block Diagram

Table 3.1: Truss Outputs for Linear SIMULAB Model

Number	Output	Units
1	Tip Lateral Acceleration	in/sec <sup>2</sup>
2	Tip Angular Acceleration	in/sec <sup>2</sup>
3	Mid Lateral Acceleration	rad/sec <sup>2</sup>
4	Station 14 Lateral Acceleration	in/sec <sup>2</sup>
5	Tip Lateral Velocity	in/sec
6	Tip Angular Velocity	rad/sec
7	Mid Angular Velocity	in/sec
8	Station 14 Lateral Velocity	in/sec
9	Tip Lateral Displacement	in
10	Tip Angular Displacement	rad
11	Mid Lateral Displacement	in
12	Station 14 Lateral Displacement	in

C. The vector  $\mathbf{Y}$  consists of the acceleration for each retained DOF in the reduced order linear truss model along with the states.

The AJT non-linear block diagram was developed in chapter 2 and the accompanying circuitry is discussed in appendix A. The transistor was implemented mathematically using the non-linear function

$$f(u) = \frac{|u|}{u + \epsilon} \quad (3.2)$$

where  $u$  is the input signal to the transistor. The function  $f(u)$  behaves similarly to a transistor, returning 1 and hence firing the positive AJT when the control signal is positive, 0 when the signal is within the dead zone of the analog circuitry, and -1 when the control signal is negative. A small  $\epsilon$  is required to prevent SIMULAB from trying to evaluate the quantity 0/0. The switch blocks work in the same manner as the three position switch implemented in hardware. However, this switch can only generate a signal with the tip AJTs, then, at the designated switch time, switch either to free vibrational decay of the planar truss in open loop or dampen modal vibrations

with the AJT controllers in closed loop. The math constant  $C$  connected to the mid-station AJTs is required because the SIMULAB switch operator tends to drift if a zero input is applied to the switch. The drifting would eventually inadvertently switch on the mid-station AJTs. The constant  $C$  is chosen to be well within the dead zone, thus preventing the mid-station AJT pair from firing unexpectedly. The open port on the switch block is where the AJT controller output will connect to when evaluating closed loop performance.

The numerical gains ( $K_i$ s) spread throughout the block diagram are there to change from one unit of measurement to another. The accelerometer gain ( $K_a$ ) converts lateral truss accelerations from inches per second-squared to volts.  $K_m$  is part of the tilting mirror platform, previously determined in section 2.4.1, and converts the mirror control voltage to a mirror control angle in milliradians. The sensor gain ( $K_s$ ) converts beam angles to the appropriate sensor voltages. The sensor gain depends on the distance of the tilting platform from the sensing element. The disturbance angle gain ( $K_d$ ) is combined with the sensor gain to properly convert disturbance mirror angles in milliradians to sensor voltage.  $K_r$  converts truss angular displacements from radians to milliradians. The gain values are listed in table 3.2.

Table 3.2: SIMULAB Gain Blocks

Gain	Value (Hz)	Conversion
$K_a$	0.101	in/sec <sup>2</sup> to volts
$K_m$	0.22	volts to milliradians
$K_d$	1.35	none
$K_s$	9.46	milliradians to volts
$K_r$	1000	radians to milliradians

The bandwidth filter in front of the disturbance mirror block is used to shape the frequency range of the white noise generator. A low pass second order filter with a cutoff frequency of 100 Hz was used to simulate high frequency non-structural disturbances to the beam path. A transfer function representation of the filter is presented in equation 3.3.

$$TF_{bw}(s) = \frac{\omega_c^2}{(s + \omega_c)^2} \quad (3.3)$$

The filter cutoff frequency,  $\omega_c$ , is  $100 \times 2\pi$  radians per second.

Both of the tilting mirror platforms used in this experiment were dynamically characterized using the methods described in section 2.4. The governing transfer function for both of the tilting mirror platforms is

$$\frac{\Theta_{mirror}(s)}{V_{control}(s)} = \frac{K_m \omega_m^2}{s^2 + 2\zeta_m \omega_m s + \omega_m^2} \quad (3.4)$$

The parameter values used in equation 3.4 for the control mirror and the disturbance mirror are presented in table 3.3.

Table 3.3: Mirror Parameters

	$K_m$	$\zeta_m$	$\omega_m(\text{rad/sec})$
Control Mirror	0.22	0.90	$2300 \times 2\pi$
Disturbance Mirror	0.141	0.45	$1700 \times 2\pi$

The variable  $K_m$  for the control mirror is separated from the mirror transfer function only so that a scope can be placed there in SIMULAB to view the angle command to the control mirror.

As discussed in Chapter 2, the control tilting mirror can be deflected only  $\pm 1.1 \text{ mrad}$ , corresponding to  $\pm 5$  volt input signals, beyond which no further movement of the mirror surface is possible in spite of increasing control signals. Voltages greater than  $\pm 7$  volts have the potential to damage the ceramic piezo stack. To prevent damage to the tilting mirror platform caused by spurious voltages and large control voltages, a voltage limiter was constructed in hardware. The input limiter was constructed using two zener diodes and a resistor on a circuit board. The circuit diagram implemented in hardware is shown in figure 3.2.

The diodes open at 4.7 volts and have a power rating of 1 watt. The use of the  $350\Omega$  resistor in conjunction with the  $100 \text{ k}\Omega$  impedance of the mirror amplifier limits



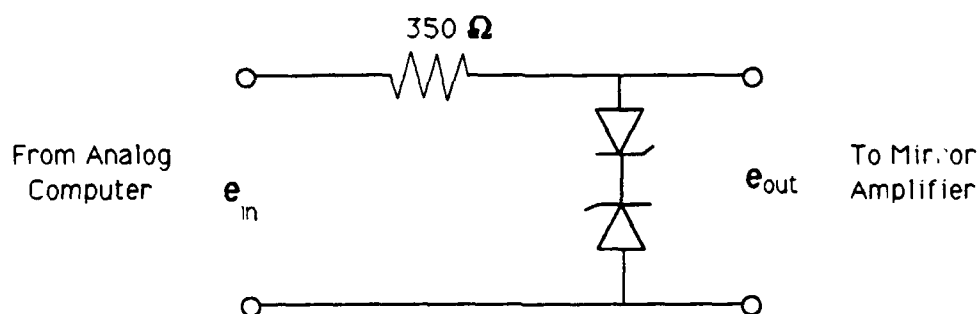


Figure 3.2: Hardware Implemented Control Input Limiter Circuit

the maximum control voltage to approximately 5 volts. The error to the control signal caused by adding the  $350\ \Omega$  load to the circuit is on the order of 3 millivolts.

### 3.2.2 Open Loop Synthesis Model Validation

The open loop plant model includes the reduced order truss model, the control and disturbance tilting mirror models, beam angle and sensor output gains, as well as linear and non-linear models for the air-jet-thrusters. The AJT linear model was used for initial controller design and frequency response analysis. The non-linear model was used with SIMULAB to provide more accurate non-linear time domain simulation of open and closed loop models. This section provides the open loop model validation necessary to obtain an understanding of modeling short comings.

Figure 3.3 shows the theoretical and experimental frequency response plots for the planar truss using the tip AJTs for the input and the servo accelerometer as the output signal. The theoretical plot employed the linear AJT model. Though the magnitude plot shows close agreement with the theoretical results, it must be remembered that the magnitude scaling for the linear AJT model is arbitrary due to the inherent non-linear effects of the actual AJT components. However, the phase information for the model, as shown in figure 3.3, is valid and not subject to any non-linear scaling problems. The experimental data was obtained using the sine sweep option on the signal analyzer. The AJT control input was swept from 1 to 50 Hz using a 1 volt peak input level. The frequency response plots show the validity of the truss and AJT modeling performed in chapter 2, and illustrates the magnitude scaling problems when using the linear AJT model for analysis.

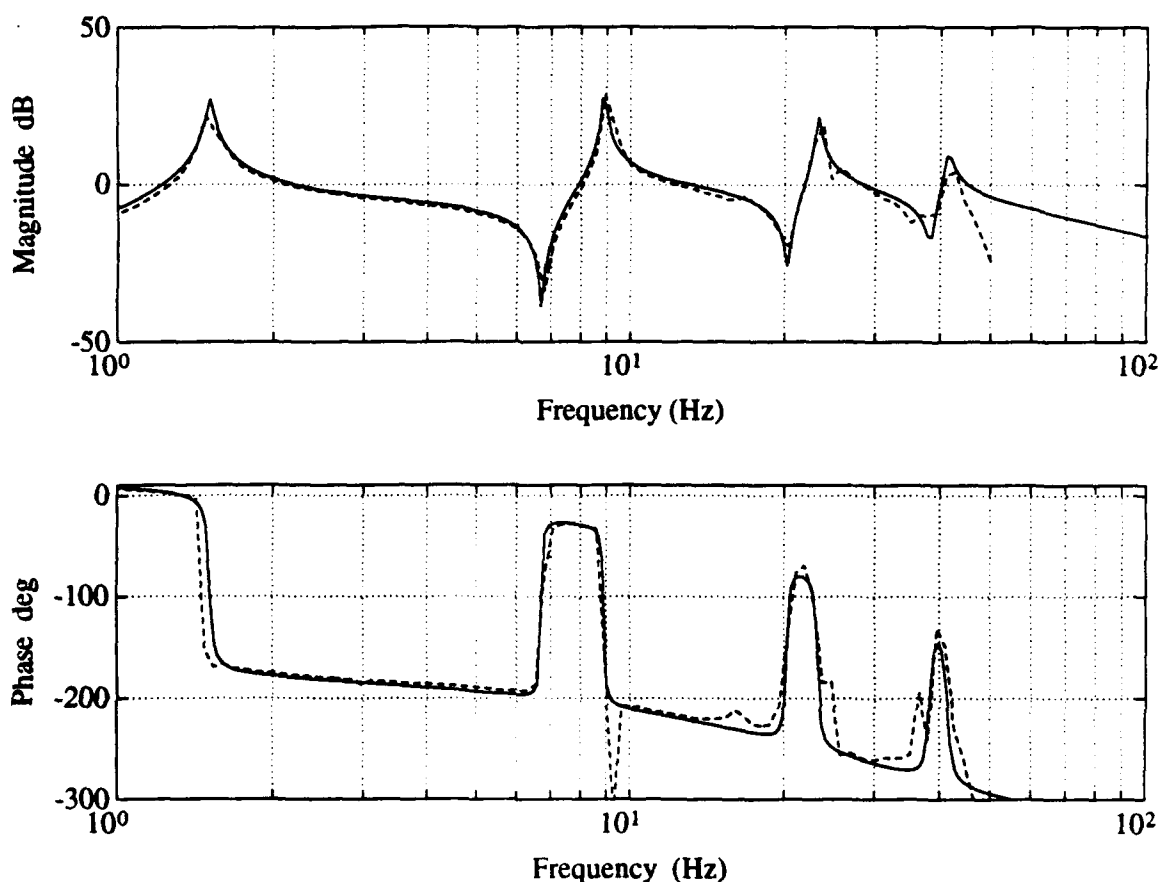


Figure 3.3: Theoretical (solid) and Experimental (dashed) Frequency Response from Accelerometer Output to AJT Control Signal Input

Figures 3.4 and 3.5 compare the open loop free vibrational decay responses of the planar truss's first four lateral modes of experimental and SIMULAB results. The plots were obtained by exciting the tip station of the truss with a sinusoidal input at each modal frequency except for the first mode where the tip of the truss was displaced 0.5 inches from the equilibrium position and released. The output was the acceleration in inches per second squared. The SIMULAB generated plots were obtained by exciting the tip of the truss at each modal frequency until the amplitudes of the experimental responses were matched. The AJTs were then turned off and the truss allowed to decay freely. As shown in figures 3.4 and 3.5 there is

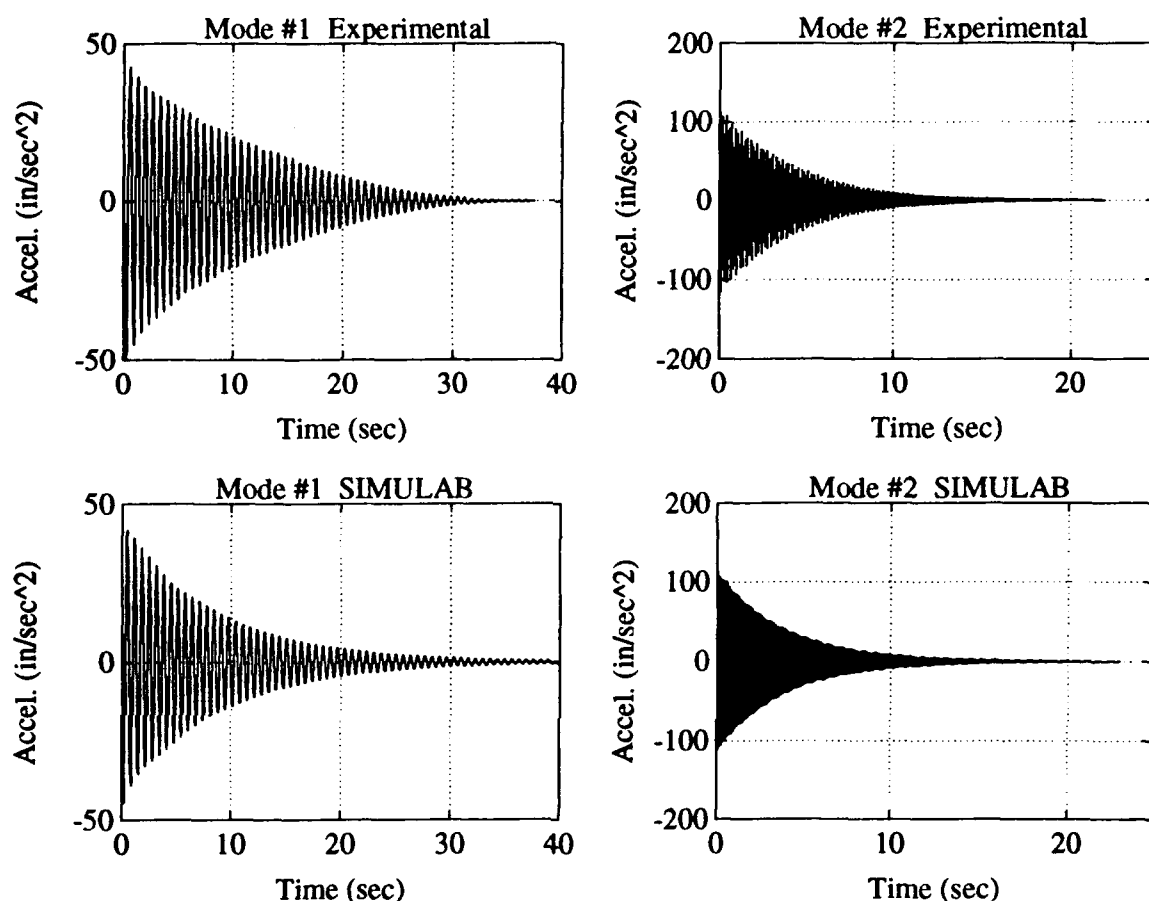


Figure 3.4: Theoretical and Experimental Truss Free Decay Time Responses

good agreement between theoretical and experimental results. The traces for mode four show the problems of using the AJTs above their effective bandwidth. Though the free decay responses of the truss were similar, the non-linear AJT model used in SIMULAB was able to excite the planar truss resonant frequencies to a much greater extent than the actual hardware. This discrepancy results primarily from the ability of SIMULAB to excite the exact modal frequency of the truss to many significant figures. Such accuracy could not be accomplished on the truss hardware. Temperature effects, which cannot be accounted for in the finite element model of the truss, also play an important factor in modeling. Truss amplitudes were reduced and modal frequencies shifted slightly as the Seattle rainy season began, bringing with it

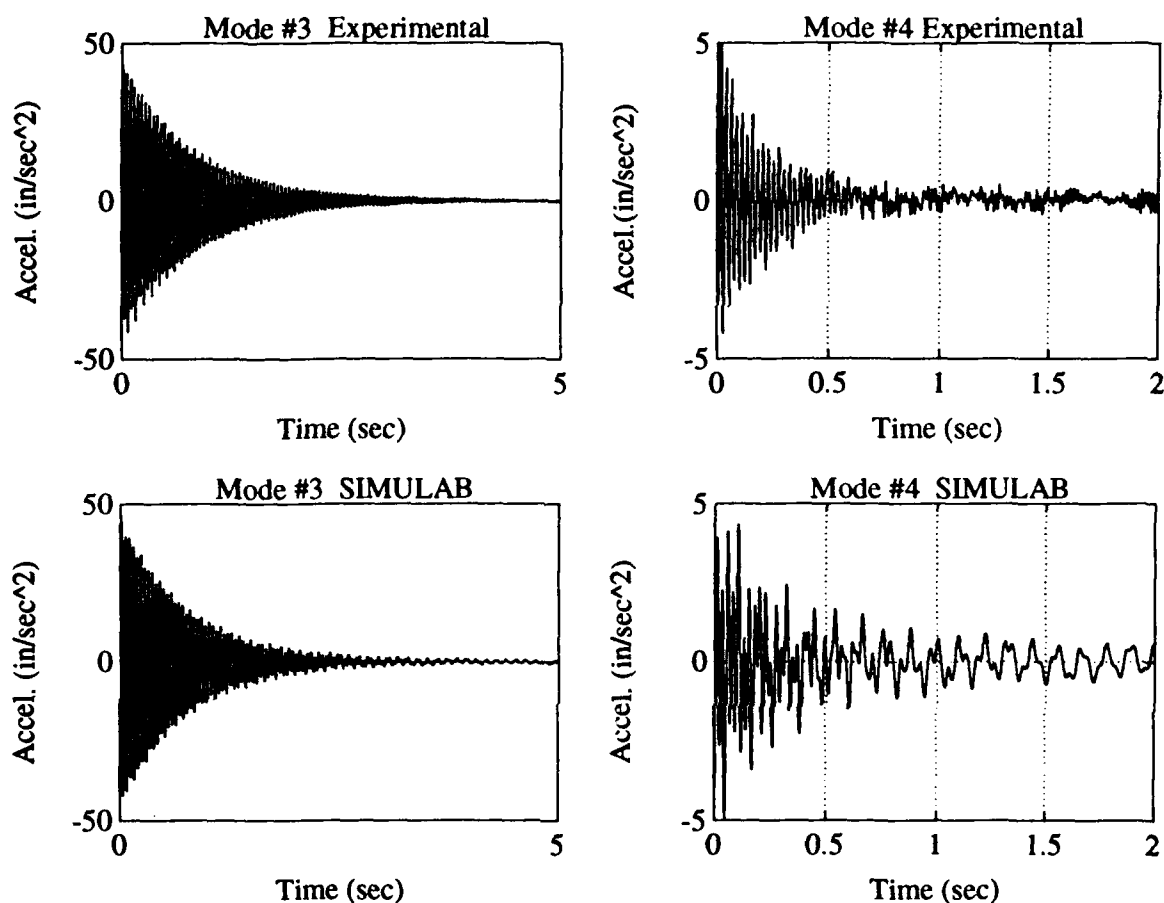


Figure 3.5: Theoretical and Experimental Truss Free Decay Time Responses

cooler temperatures. The cooler air increased the stiffness of the flexible members, thus slightly changing truss characteristics, and resulting in lower amplitude lateral vibrations. Other contributing factors to theoretical and experimental discrepancies are the linear viscous damping approximation and experimental modal coupling.

The large amplitude vibrations do not pose a problem when designing a vibration damping system for the truss as one wishes to design a controller for worst case scenarios. However, when designing a controller for the tilting mirror platform, in order to examine control mirror effectiveness at low displacements, the truss could not be allowed to vibrate outside the mirror throw. In hardware, exciting the first and sometimes the second (in warmer temperatures) lateral modes would cause the

truss to vibrate beyond the range of the mirror. A simple solution to the problem was to arbitrarily lower the amplitude of the disturbance to the laser beam path caused by the angular motion of the tip of the truss when evaluating the performance of the stand alone tilting mirror controller. This was accomplished for the first two lateral modes in SIMULAB where truss vibrations exceeded mirror throw. When examining the effectiveness of the combined AJT and mirror platform controller, reduction in truss tip amplitude was not necessary.

### *3.3 Controller Design Method*

Once all of the modeling and open loop validation of the synthesis model was completed, controller design for the mirror and AJT actuators could finally commence. The design method is iterative. The initial design was accomplished by analyzing closed loop frequency characteristics using the linear model of the AJTs for excitation of the lateral vibrational modes of the truss. Time domain performance was analyzed on SIMULAB using the more accurate non-linear model for the AJTs and mirror control signal limiter. The theoretical analysis provided an initial parameter range for controller gains. These gains were fine tuned during hardware implementation in order to obtain the best results. Then it was back to the theoretical model for further validation of the SIMULAB model using experimental results.

### *3.4 Tilting Mirror Controller*

The tilting mirror is primarily used to reject low amplitude structural oscillations caused by high and low frequency vibrations as well as non-structural disturbances to the beam path. There are no structural interaction problems as the small tilting mirror platform could never generate a torque large enough to effect the truss. The controller was designed to generate the best rejection performance, considering noise, implementation issues, and to a some extent robustness.

#### *3.4.1 Theoretical Controller Design and Hardware Implementation*

The compensator is designed using proportional and integral (PI) control. The use of derivative control was considered, but the noise characteristics of implementing

derivative control on an analog computer outweighed the benefits. Proportional feedback is used to reject structural and other optical disturbances and integral control is necessary to eliminate steady state errors. The transfer function for the PI controller is of the form

$$PI(s) = K_p + \frac{K_i}{s} \quad (3.5)$$

where  $K_p$  is the proportional gain and  $K_i$  is the integral gain. Equation 3.5 can be manipulated such that only one parameter need be varied. The PI controller becomes

$$PI(s) = \frac{s + \alpha}{s} \quad (3.6)$$

where

$$\alpha = \frac{K_i}{K_p}$$

The placement of the PI controller zero determines the closed loop characteristics of the tilting mirror platform. As the value of  $\alpha$  is increased the zero is moved further out on the left-half plane. The performance of the mirror increases with the increase in bandwidth. The drawback is that the stability of the mirror platform suffers with increasing gain as the poles of the mirror plant return towards the imaginary axis and become less damped.

When designing a controller using only theoretical techniques one sometimes ignores modeling errors and implementation issues in search of a stable design that produces the best theoretical performance. These 'excellent' theoretical designs often do not work well when implemented on hardware. The designer must consider the weaknesses and limitations of the hardware while designing a controller using theoretical techniques. A limiting factor in this particular case is the analog computer. The operational-amplifiers of the computer are linear to  $\pm 10$  volts and overload if more than fifteen volts is applied. To get the best performance out of the tilting mirror platform high gains are required to increase the effective bandwidth. However, very high gains pose a problem for the analog computer as one of the OP-AMPs in the controller may go beyond its linear range, even though the final output is well within

the  $\pm 10$  volt linear range of the analog computer. Another source of error is the small noise term induced by the implementation of the control limiter with the zener diodes. Care was taken not to design the controller to be effective inside the noise level of the hardware.

Theoretically, to achieve maximum disturbance rejection, the controller zero should be placed as far in the left half of the s-plane as possible while still maintaining actuator stability. However, the analog computer and to some extent noise from the position sensor and zener diodes limit the size the control gains. Theoretical analysis provided a suitable starting point for  $\alpha$ . The controller was then implemented on the hardware and the gains fine tuned to produce the best performance possible, in the face of noise, modeling uncertainties, and the limitations of the analog computer. The final PI controller implemented on the hardware was

$$PI(s) = \frac{s + 8000}{s} \quad (3.7)$$

This choice for  $\alpha$  provides good disturbance rejection for the first four lateral modes of the truss and fast response to any initial steady state tracking error as will be shown in section 3.4.2. The values used for the integral and proportional gains were 8000 and 1 respectively. Figure 3.6 shows the wiring diagram for the analog implementation of the PI controller.

The robustness of the closed loop design was analyzed in terms of a single loop gain and phase margin. From figure 3.7 the gain and phase margin for the PI controller were determined.

$$\begin{aligned} \text{Gain Margin} &= \pm\infty \text{ dB} \\ \text{Phase Margin} &= 89 \text{ deg} \end{aligned} \quad (3.8)$$

Equation 3.8 indicates that the system is extremely stable and controller gains could be increased almost without bound and the stability of the closed loop system would remain intact. However, hardware implementation issues prevent this.

Another important aspect of the controller to examine is its command following properties. This is accomplished by determining the closed loop bandwidth of the linear PI controller. The higher the bandwidth the better able is the system to reject

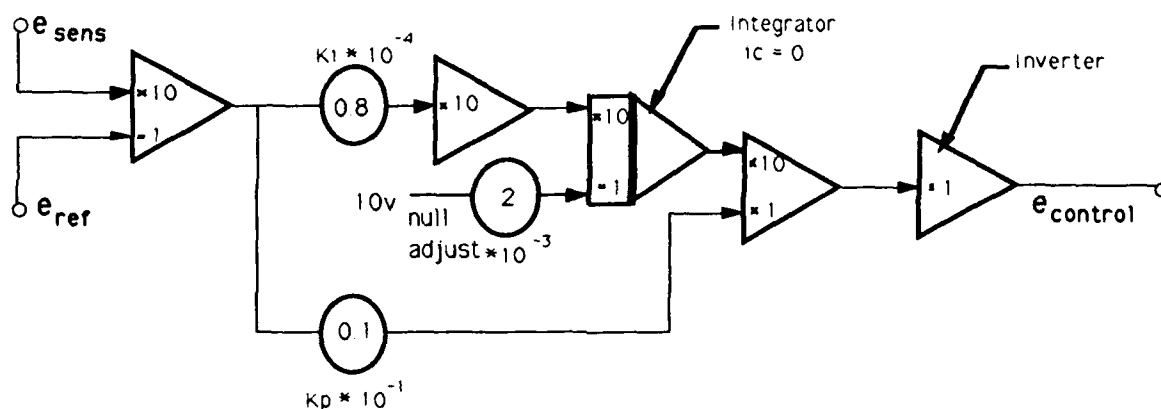


Figure 3.6: Analog Control Circuit for PI Controller

beampath disturbances and the faster it eliminates tracking errors. The command bandwidth was experimentally determined by injecting a sinusoidal control input to the  $e_{ref}$  input of the analog controller (figure 3.6). A sine sweep from 10 to 1000 Hz was performed using a 1 volt peak input. This simulates a movement corresponding to 0.1 volts on the sensor. The bandwidth of the system is found using  $-3dB$  as the cutoff frequency. From figure 3.8 the experimental bandwidth is 200 Hz. The closed loop bandwidth is high with respect to the modes of the truss and should provide good disturbance rejection properties and quick elimination of any steady state errors.

### 3.4.2 Theoretical and Experimental Results

The rejection of line-of-sight disturbances caused by excitation of the flexible structure is a primary design goal. The disturbance rejection capabilities are analyzed by exciting the truss with a sinusoidal sweep and comparing the open and closed loop beam motion. The sine sweep option on the signal analyzer was used to sweep the planar truss from 5 to 40 Hz using the tip AJTs. Because the AJTs begin to lose their effectiveness above the third mode, an RMA mounted to the tip of the truss was used to excite the fourth and subsequent modes. The RMA was swept from 40 to 100 Hz with a one volt peak input. The amplifier gain for the RMA was set to four. Figure 3.9 shows the corresponding magnitude plot in the frequency domain for the



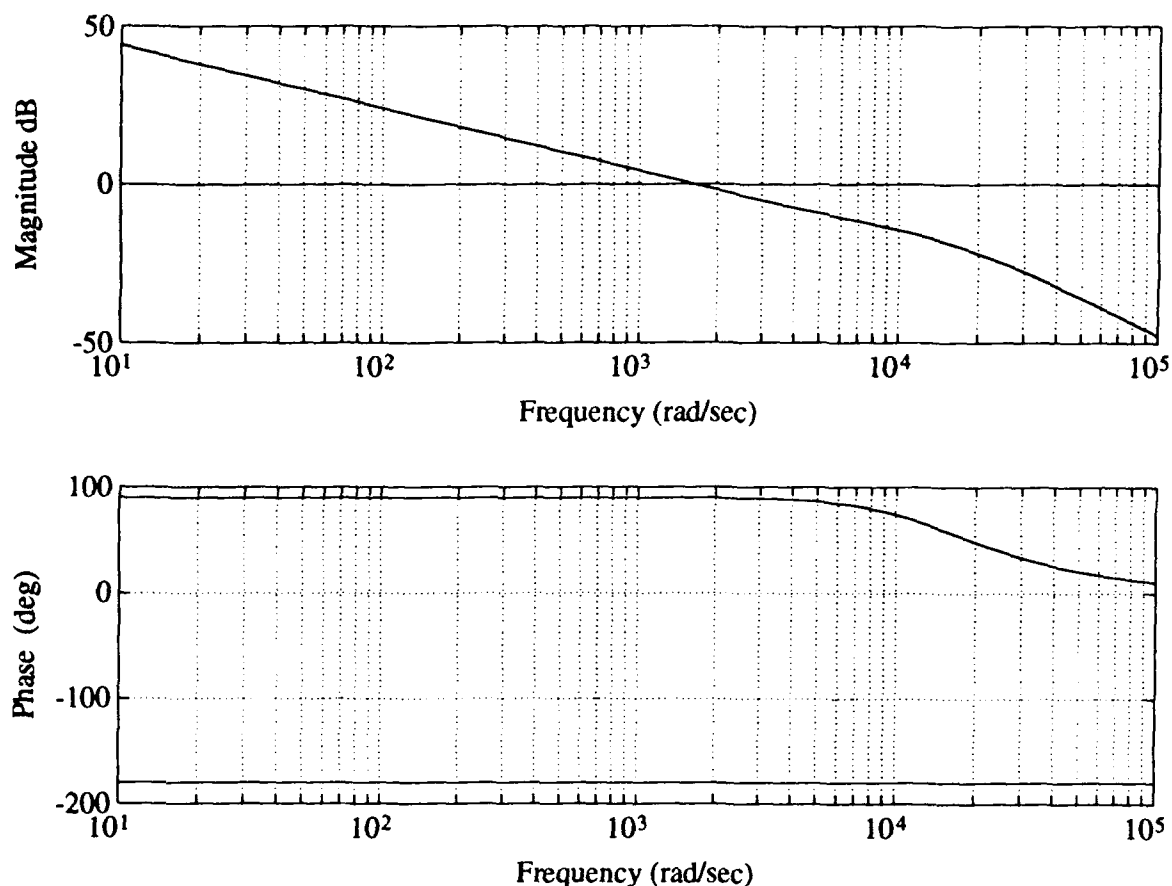


Figure 3.7: Controller Stability Margins

open and closed loop systems displaying the input-output relationship from excitation input voltage to sensor output voltage. The AJT data can readily be combined with the RMA data as our interest lies not in the magnitude of the outputs, but rather the difference between the open and closed loop responses.

Figure 3.9 was used to determine a disturbance rejection curve for the closed loop system from 1 to 100 Hz. The disturbance rejection value for the first resonant lateral mode, for excitations remaining within the mirror's range of motion, was extrapolated from the available data. The transfer functions from excitation voltage to sensor voltage for both the open loop and closed loop cases were used to derive the disturbance rejection properties for the closed loop system. The relevant open and

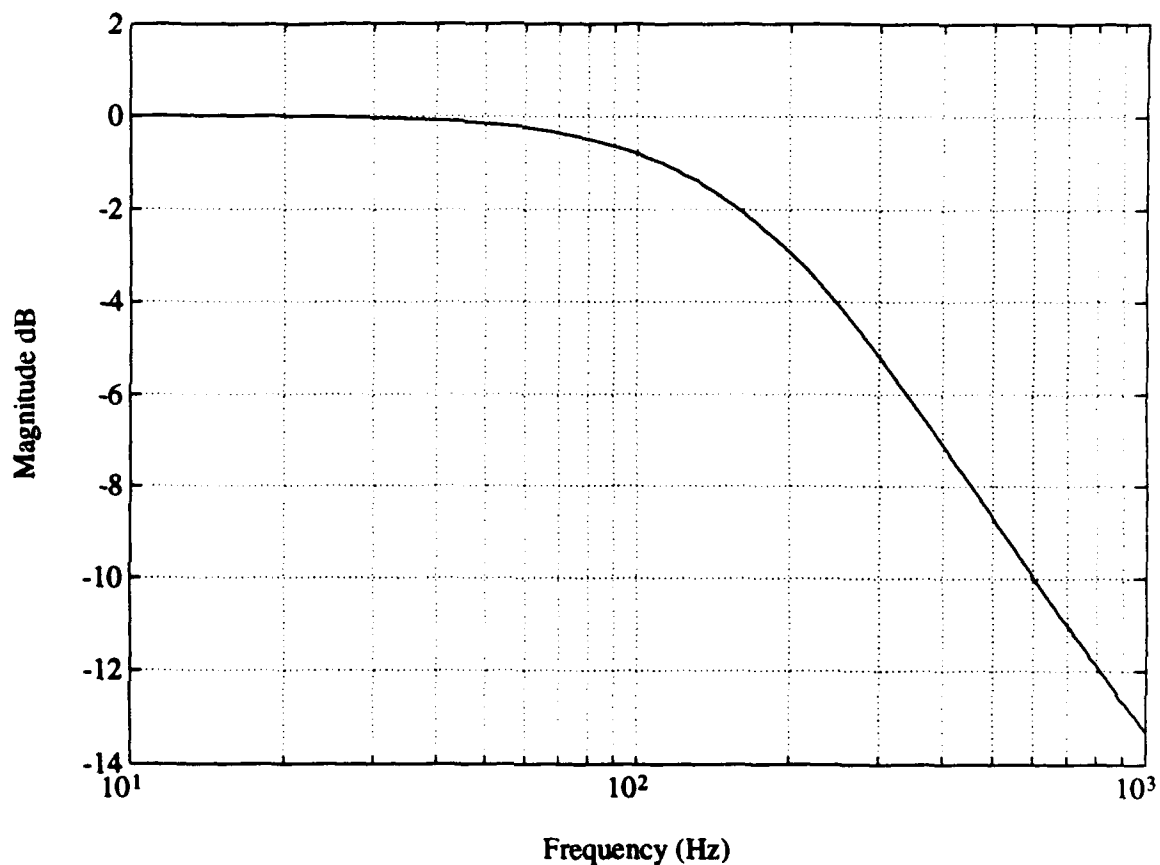


Figure 3.8: Closed Loop Bandwidth

closed loop relationships are:

$$\frac{\left(\frac{V_{beam_{OL}}}{V_{excitation}}\right)}{\left(\frac{V_{beam_{CL}}}{V_{excitation}}\right)} = \frac{V_{beam_{OL}}}{V_{beam_{CL}}} = \frac{K_{beam}\Theta_{CL}}{K_{beam}\Theta_{OL}} = \frac{\Theta_{CL}}{\Theta_{OL}} \quad (3.9)$$

where  $\Theta$  is the beam angle and  $K_{beam}$  is the gain that converts a sensor voltage to a beam angle in milliradians. Also note that  $V_{beam} = V_{sensor}$ . Equation 3.9 is manipulated to produce

$$20 \times \log_{10}\left(\frac{\Theta_{CL}}{\Theta_{OL}}\right) = 20 \times \log_{10}(\Theta_{CL}) - 20 \times \log_{10}(\Theta_{OL})$$

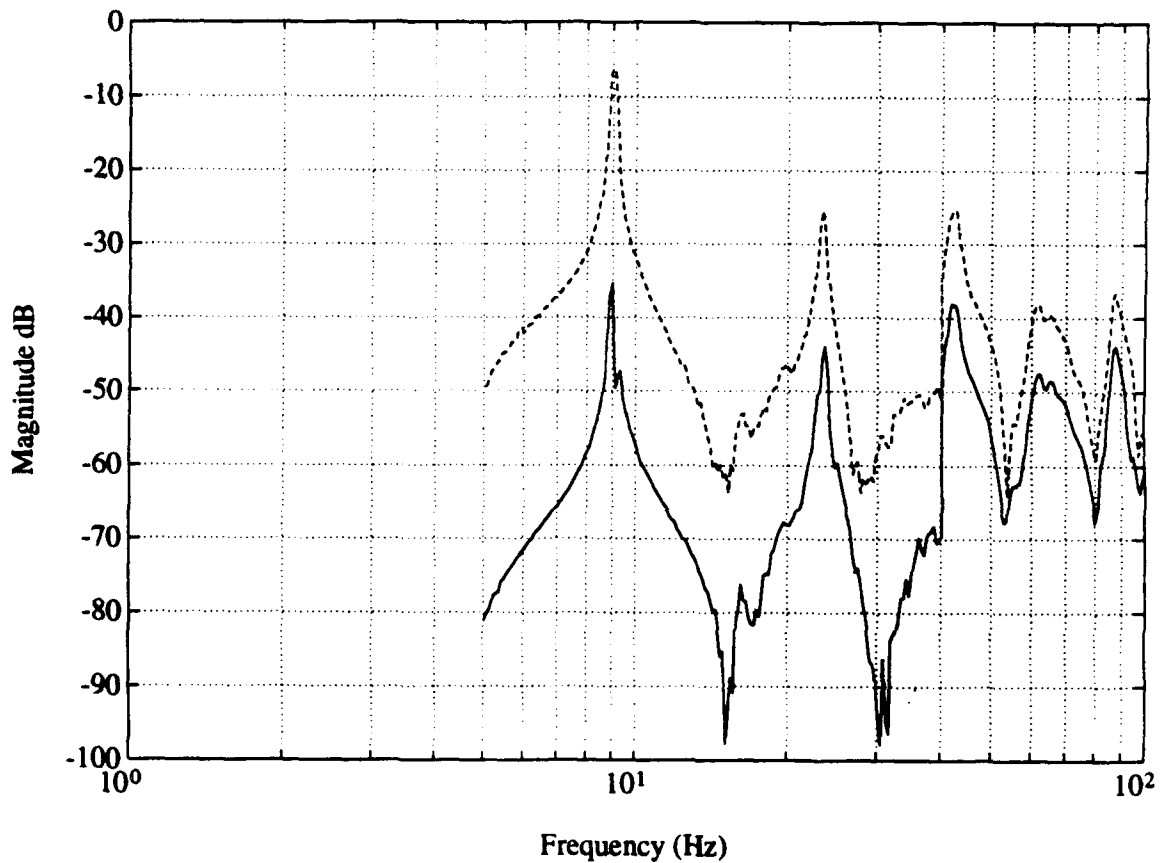


Figure 3.9: Open (dashed) and Closed (solid) Loop Magnitude Plot

$$= \frac{V_{beam_{OL}}}{V_{excitation}}(dB) - \frac{V_{beam_{CL}}}{V_{excitation}}(dB) \quad (3.10)$$

The magnitude plot of the open loop transfer function can be subtracted from the magnitude plot of the closed loop transfer function to find the disturbance rejection curve in the frequency domain. Figure 3.10 shows the disturbance rejection curve generated from equation 3.10. The dashed line indicates a linear curve fit to the data when examined with a logarithmic frequency axis.

The largest disturbances experienced by the beam occur when the flexible structure is excited at its resonant modes. Table 3.4 shows the disturbance rejection values for the first six lateral modes of the truss. The frequencies for the fourth and subsequent

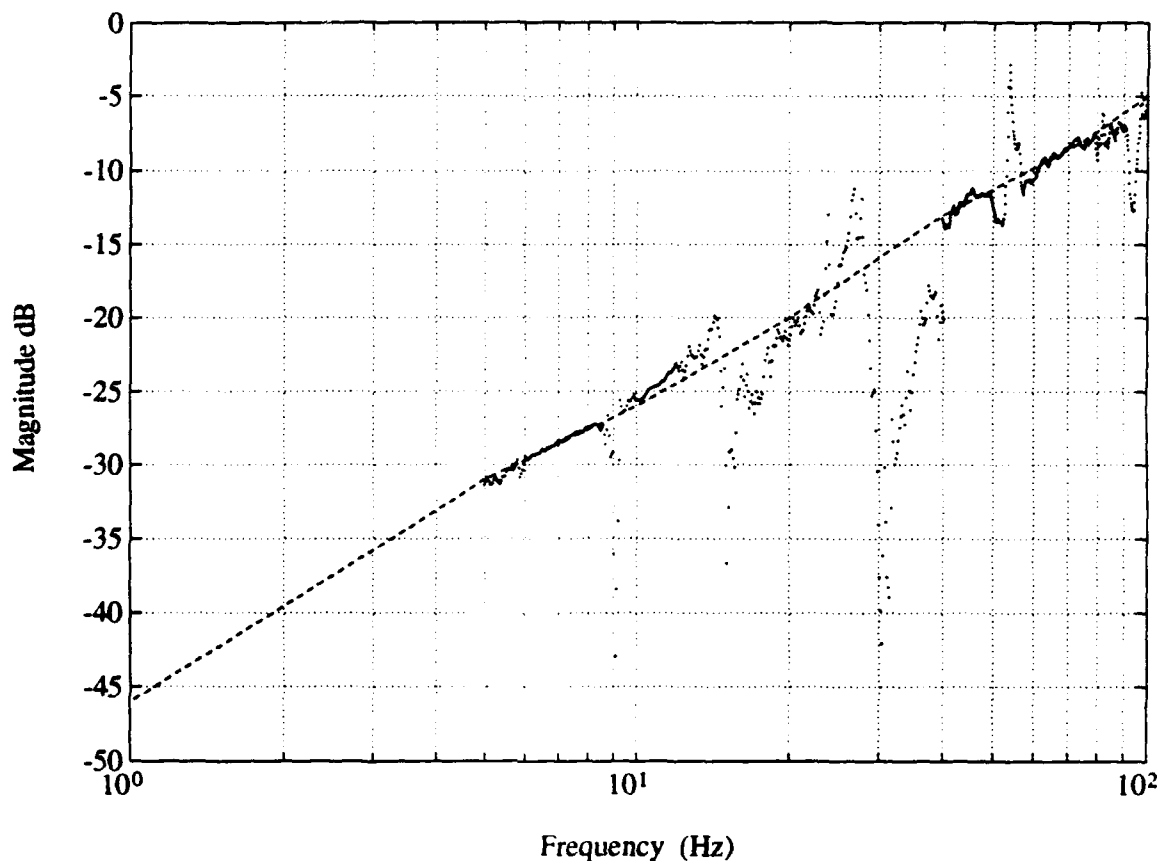


Figure 3.10: Disturbance Rejection Curve With Curve Fit (dashed)

lateral modes of the truss shifted somewhat when an RMA was used for excitation. Adding the tip RMA is similar to adding a mass to the tip of the truss, thus slightly shifting the resonant modes. This is not a problem since we are concerned only with an open and closed loop response comparison at each mode and not with the actual location of the mode. With the RMA, data for the fifth and sixth lateral modes were also obtained and are presented for completeness.

The closed loop system demonstrates good disturbance rejection for the lower lateral modes of the truss. Performance at the lowest modes is critical as they cause the largest displacements of the beam and hence the greatest targeting and tracking errors.

Table 3.4: Modal Disturbance Rejection Values in dB

Mode	Frequency (Hz)	Rejection (dB)
1	1.55	-42
2	8.89	-27
3	23.3	-19
4	42	-13
5	71	-8
6	87	-7

Frequency domain analysis provides a good indication of the overall rejection properties of the PI controller. Time domain analysis of the mirror controller to structural and non-structural white noise disturbances and to constant disturbances at specific modal frequencies was also conducted. This was accomplished to further validate the theoretical SIMULAB model and as a comparison to the results presented in table 3.4. Disturbance rejection responses from the excitation with the tip AJTs of the first four discrete structural modes of the planar truss were examined. Time responses to structural and non-structural white noise disturbance inputs from the AJTs and disturbance mirror were also analyzed.

Figures 3.11 and 3.12 show the experimental and SIMULAB time responses of the PI mirror controller to continuous structural disturbances at the first four lateral modes of the planar truss. The vibrational modes were excited by the tip AJTs using a sinusoidal control signal at each resonant frequency. To provide accurate comparison between experimental and theoretical results, the output tip angular amplitude of the linear truss model in SIMULAB was arbitrarily scaled for the first two resonant modes so the sensor displacements remain within the mirror throw. The experimental results for the first mode were obtained by displacing the planar truss the length of the mirror and switching on the PI controller when the position error on the sensor was within the throw of the mirror. Figures 3.11 and 3.12 indicate good rejection to continuous disturbances. The effect of the integral action is evident in the third and fourth mode responses as the location of the disturbance, after the controller

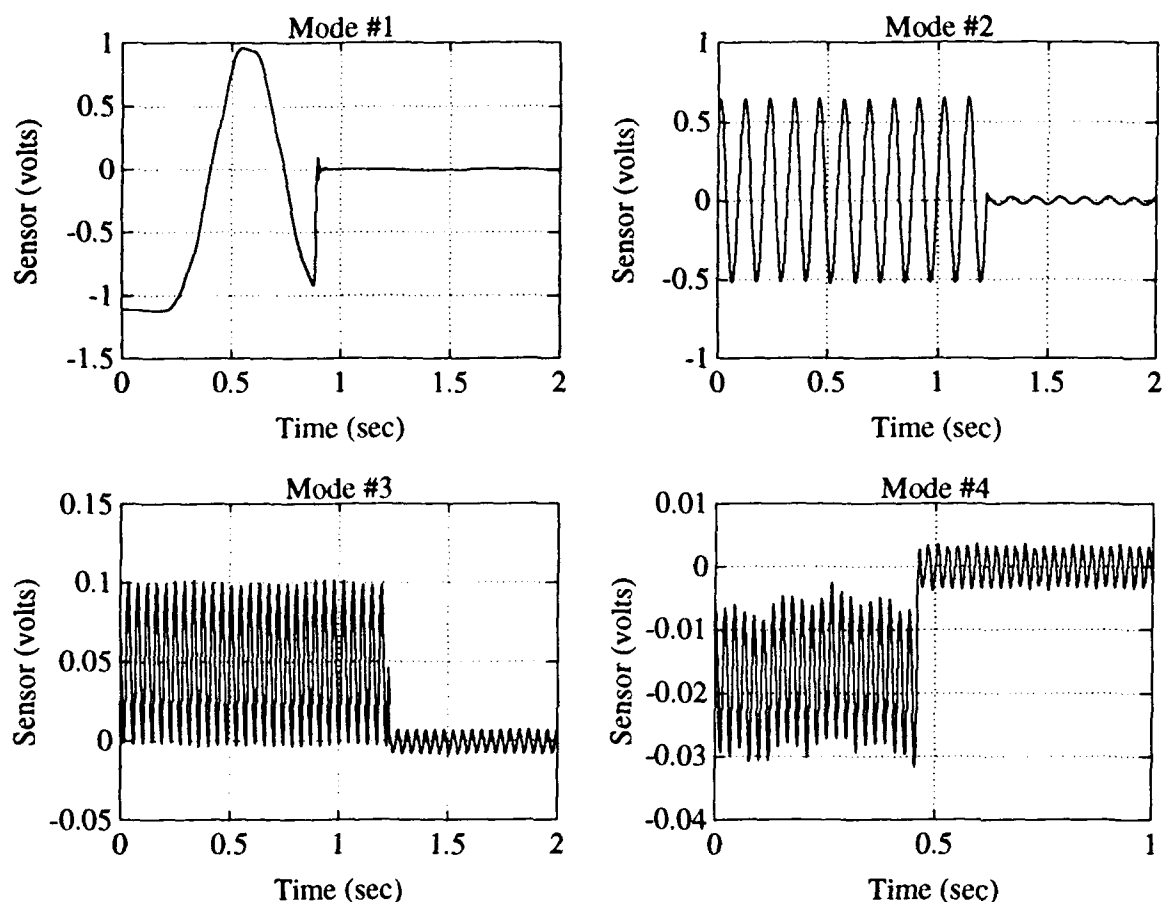


Figure 3.11: Experimental Closed Loop Time Responses to Continuous Structural Disturbances

is switched on, is moved from off center to be centered around zero volts which corresponds to zero position error. A rejection value of  $-20dB$  indicates that the disturbance to the beam path has been reduced by a factor of ten after closing the PI control loop. The results from the time response plots agree very well with the discrete rejection responses shown in table 3.4. The SIMULAB generated response of the fourth lateral mode illustrates the ineffectiveness of the AJT actuator at higher frequencies and model reduction inaccuracies. The modal coupling effects can be seen in the fourth mode. The coupling is a result of retaining only four degrees of freedom in the reduced order truss model. More accurate results could be obtained by retaining more DOFs in the reduced order model. However, this would increase

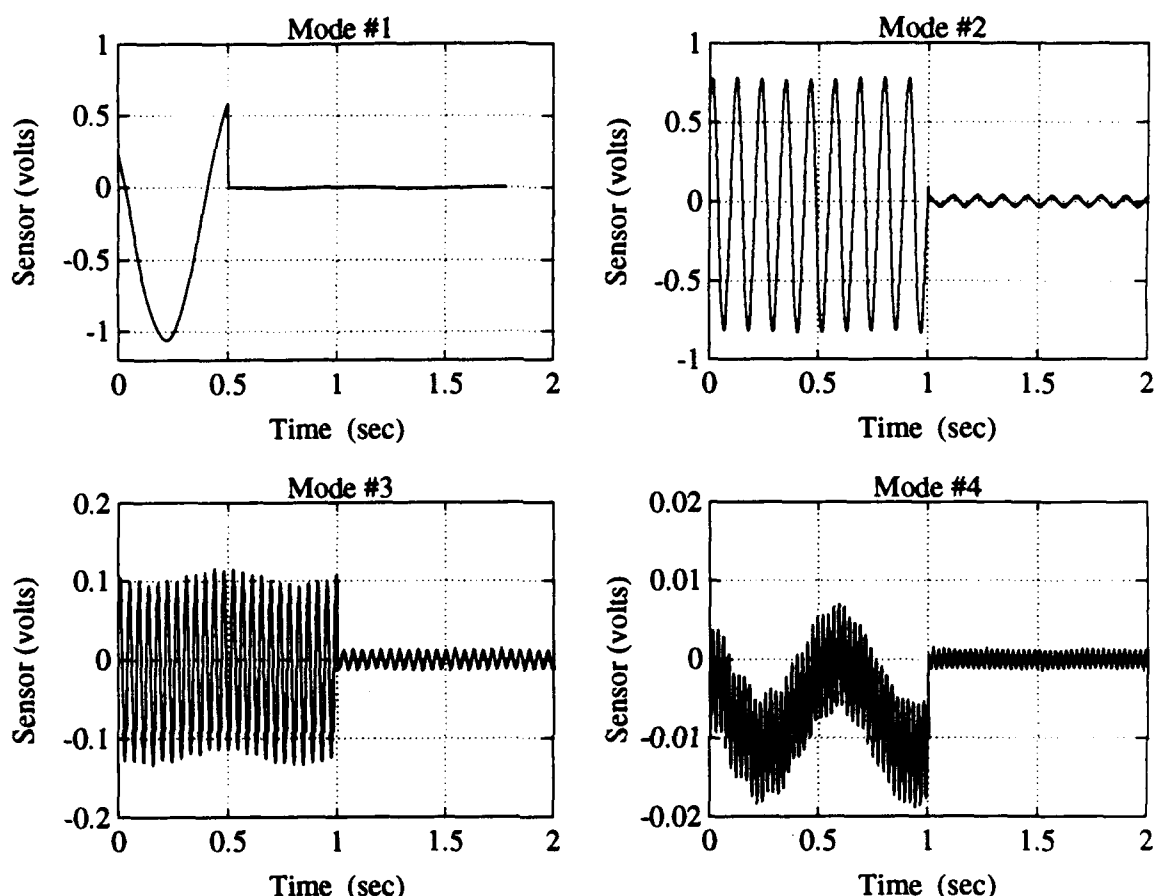


Figure 3.12: Theoretical Closed Loop Time Responses to Continuous Structural Disturbances

the size of the system.

Figure 3.13 shows the time responses of the sensor output for the control system when subjected to white noise disturbances to the structure and beampath. The structural disturbances were generated by sending a white noise control signal ranging from 0 to 50 Hz from the signal analyzer to the tip AJTs. The non-structural beam path disturbance was generated by sending a 2 volt peak random noise input to the disturbance mirror from 0 to 100 Hz to show high frequency disturbance rejection properties. Note that lower frequency disturbances are more effectively rejected by the control mirror, which was expected. The SIMULAB generated results are similar to experimental results and hence we continue the validation of the theoretical model

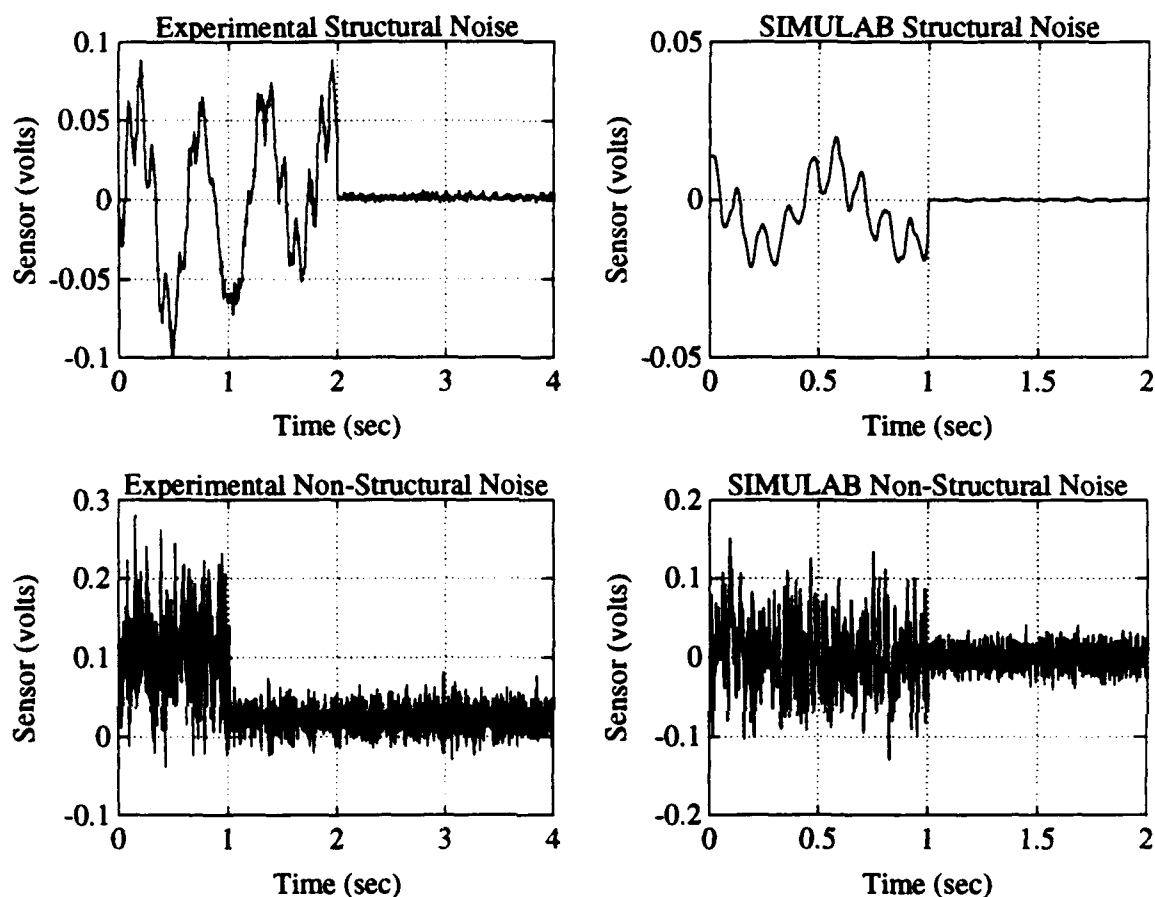


Figure 3.13: Time Responses to Structural and Non-structural White Noise Disturbances

which can then be effectively used in future design work. The only discrepancy is in the magnitude of the structural disturbance in SIMULAB. The reason for the discrepancy is unknown.

### 3.5 Air-Jet-Thruster Control

The tilting mirror platform functions well for any small amplitude lateral vibrations. The PI controller for the mirror can easily perform disturbance rejection, command following, and steady state error elimination functions. However, when the first, and occasionally the second, mode are excited, perhaps after a high speed large angle slew



or impact with space debris, the  $\pm 1$  mrad throw of the control mirror cannot take care of the large amplitude vibration. When the first mode is sufficiently excited the lateral motions are large enough that the beam path oscillations leave the face of the mirror. When this occurs the mirror controller would lose its feedback signal entirely. A need for a separate control actuator and sensor is evident. The AJT controller was designed to act directly on the truss, suppressing low frequency structural lateral vibrations to bring the oscillatory amplitudes quickly within the range of the tilting mirror platform.

Back-to-back pairs of AJTs were mounted at the tip and midstation of the planar truss. Colocated accelerometers are attached at the tip and midstations along with the air-jets to monitor lateral vibrational motions and provide the necessary feedback signal for the AJT controller.

A simple type of vibration control using on-off actuators is active damping that emulates ideal coulomb friction. The sign of the damping force is always opposite that of the velocity. The AJTs provide a force opposite to the direction of the velocity of the truss to quickly dampen the unwanted vibrations of the flexible structure. The velocity controller used in this experiment was first used by Hallauer and Lamberson on a similar structure at the U.S Air Force Academy [5].

The ideal control law using the AJT actuators and colocated sensors is

$$F_i = -F_{s,s} \text{sgn}(v_i) \quad i = 1, 2 \quad (3.11)$$

where  $v_i = \dot{q}_i$  is the velocity,  $f_i$  is the bipolar force generated by the AJT pair, and  $F_{s,s}$  is the steady state thrust of the air-jets. The  $i$  subscripts correspond to the tip and midpoint truss locations respectively. However, time delays in the AJTs and sensor noise make this type of ideal implementation unrealizable in hardware. It is necessary to provide a dead bandwidth to prevent the system from continuously chattering once the velocity falls within the noise level of the sensors and electronic circuitry. The dead band affects controller operation by cutting off the control signal to the AJTs once the velocity falls within a certain threshold. The operation performed by each analog control circuit is

$$ef_i = \begin{cases} -E & ev_i > ev_d \\ 0 & |ev_i| \leq ev_d \\ E & ev_i < -ev_d \end{cases} \quad (3.12)$$

where  $ev_d$  is the voltage signal corresponding to the deadband halfwidth and  $ef_i$  and  $ev_i$  are the voltage signals corresponding to  $f_i$  and  $v_i$  respectively. A satisfactory deadband is  $ev_d = 9mv$  corresponding to a velocity of 0.09 inches per second. This value is larger than the accelerometer noise level yet small enough to have little effect on controller effectiveness.

The velocity signal  $ev_i$  is easily obtained through the integration of the servo accelerometer signal. An approximate integrator is necessary because exact integrators tend to drift and are susceptible to small DC voltages that are never completely purged from the electronic circuitry. Small DC offsets will grow and eventually ruin the feedback signal. A second order approximate integrator was used so that zero DC gain can be achieved. The differential equation describing the approximate integrator is

$$e\ddot{v}_i + \Omega_r e\dot{v}_i + \Omega_r^2 ev_i = \frac{1}{RC} ea_i \quad (3.13)$$

A transfer function representation of the above system was easily formulated. Taking the Laplace transform and setting all initial conditions equal to zero leaves

$$(s^2 + \Omega_r s + \Omega_r^2) ev_i(s) = s ea_i(s) \quad (3.14)$$

The transfer function for the approximate integrator is thus

$$G_{integrator}(s) = \frac{ev_i(s)}{ea_i(s)} = \frac{s(\frac{1}{RC})}{s^2 + \Omega_r s + \Omega_r^2} \quad (3.15)$$

Notice that when  $s = j\omega = 0$  the value of the approximate integrator is also zero. Stray DC voltages have been effectively eliminated. The numerical values for  $\Omega$  and  $RC$  are  $0.2\pi \frac{rad}{sec}$  and 1 sec respectively. The frequency responses of exact integration and the approximate integrator are shown in figure 3.14. Approximate integration is essentially the same as exact integration at frequencies above 1 Hz.

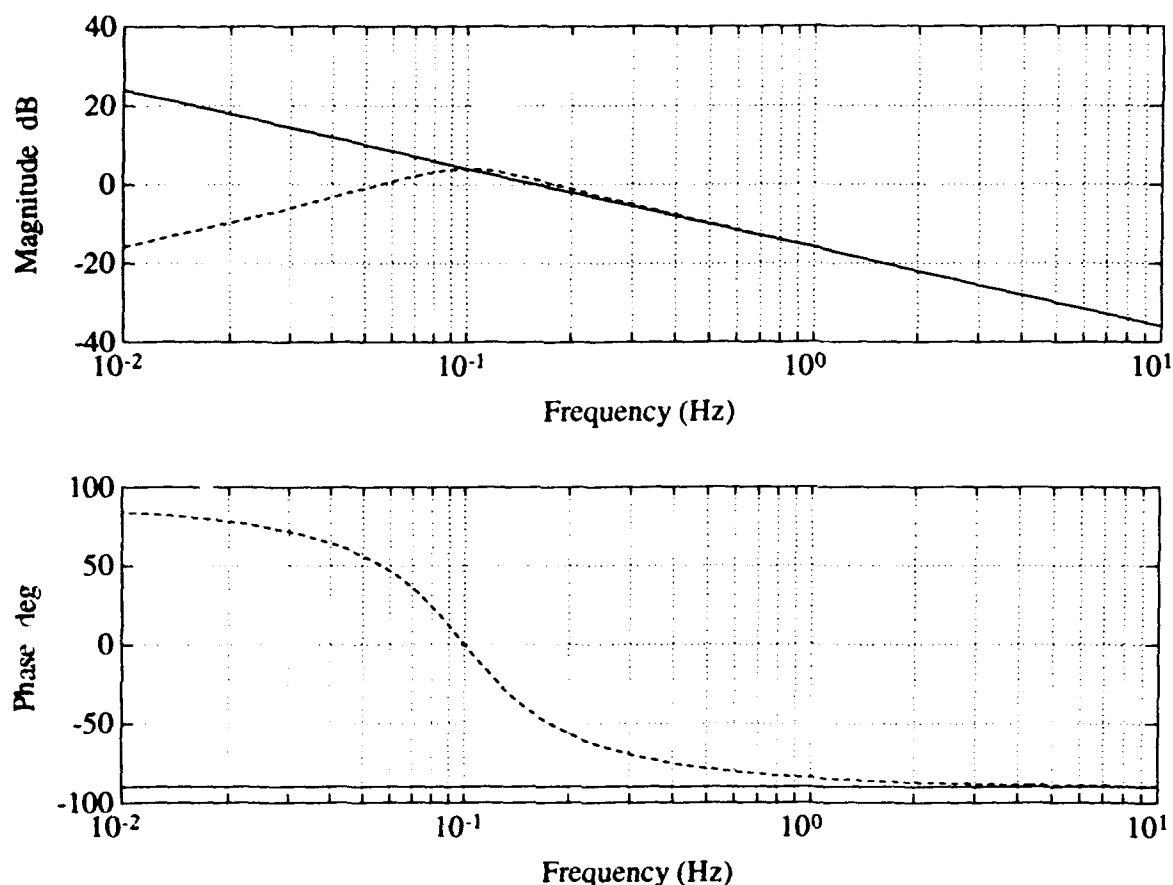


Figure 3.14: Frequency Response Comparison Between Exact Integration (solid) vs. Approximate Integrator (dashed)

### 3.5.1 Controller Implementation and Results

The approximate integrators were implemented on an analog computer for the tip and mid span pair of AJTs. The analog circuitry is shown in figure 3.15.

Because of the unevenness of the lab floor, the table that the truss lies on is not completely level. The high sensitivity of the accelerometers and the lopsideness of the floor leads to a small constant DC offset voltage resulting from gravity, when the planar truss rests in its equilibrium position. Instead of zeroing the accelerometer with resistors as is commonly done, it was much easier to zero out the accelerometer offset voltage using a pot on the analog computer.

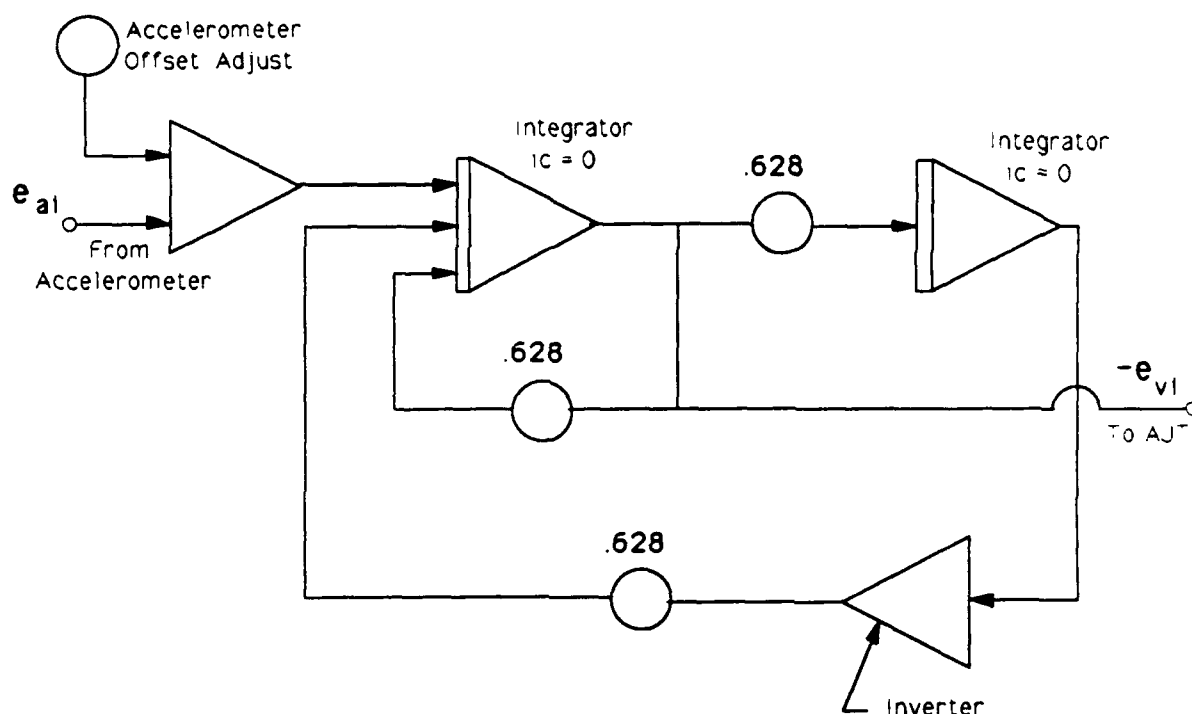


Figure 3.15: Analog Implementation of AJT Controller

Active damping performance of the AJT control system was evaluated experimentally in tests of free vibration response. The AJTs were used to excite the truss at a resonant modal frequency. After achieving a sufficient steady state amplitude the switch was moved into the *Control* position, closing the loop with the approximate integrator. Figure 3.16 and 3.17 show the experimental and theoretical open and closed loop responses of the AJT controllers for the first two lateral modes of the planar truss. The output voltage measures beam position on the sensing element. The large dips in the experimental sensor output result as the truss vibrational amplitudes become large enough that the laser beam goes beyond the width of the control mirror, thus the position of the beam path can no longer be determined. The straight lines passing through the data at  $\pm 1$  volts mark the amplitude at which the beam motion is within the mirror throw.

The AJT controller reduces considerably the time required for the truss oscillations to get within the tilting mirror's range for the first mode. The AJTs are also very

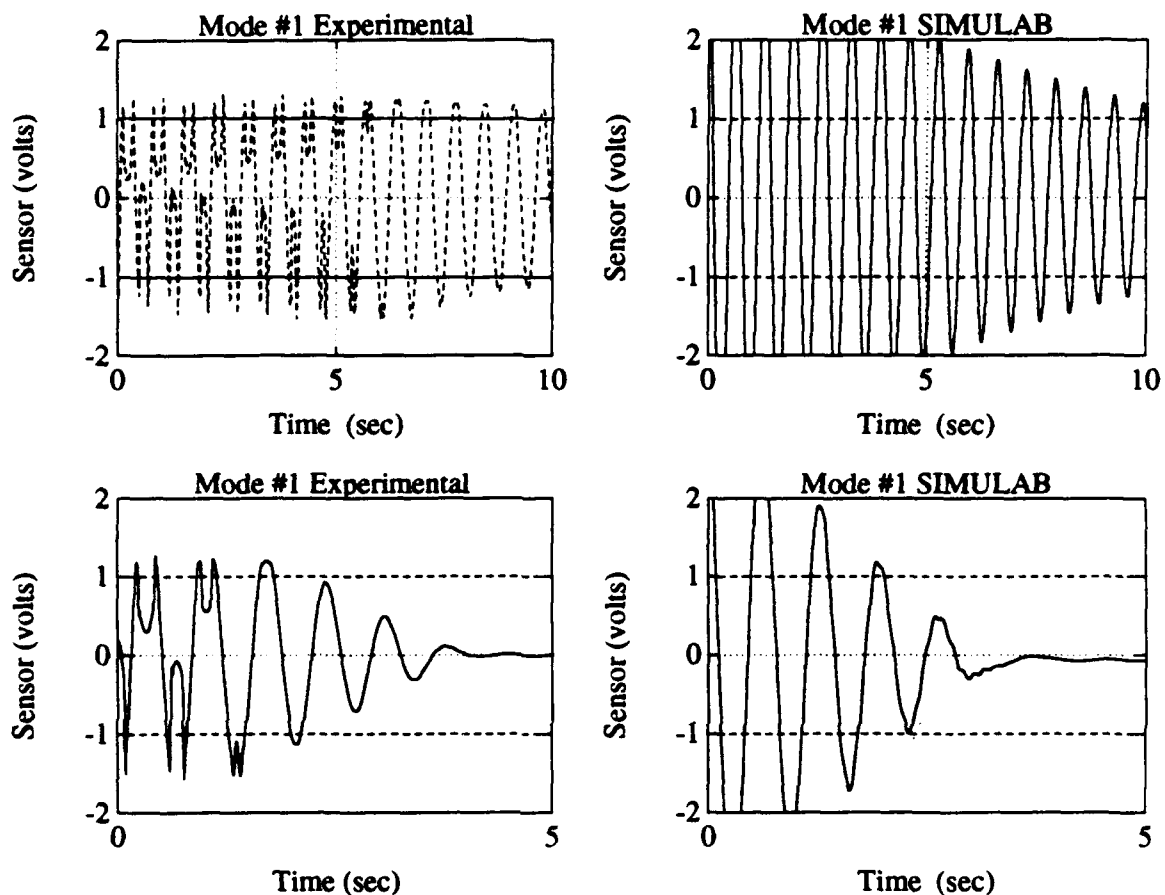


Figure 3.16: Mode 1 Experimental and Theoretical Open and Closed Loop Responses for AJT Controller

effective at the second vibrational mode. These are the primary modes at which the lateral vibrations of the truss may exceed the range of the tilting mirror. The AJTs are effectively used to quickly dampen the first two vibrational modes of the planar truss.

The AJT controller works well for the first and second mode of the truss. At these lower lateral modes the AJT controller is necessary to get the mirror platform back into its tilting envelope. Then the mirror platform effectively rejects the disturbance to the beam path and the AJTs can be turned off. If a limited air supply is not a problem the AJTs can be left on to quickly dampen lower modes of the truss and help the tracking error return quickly back to zero.

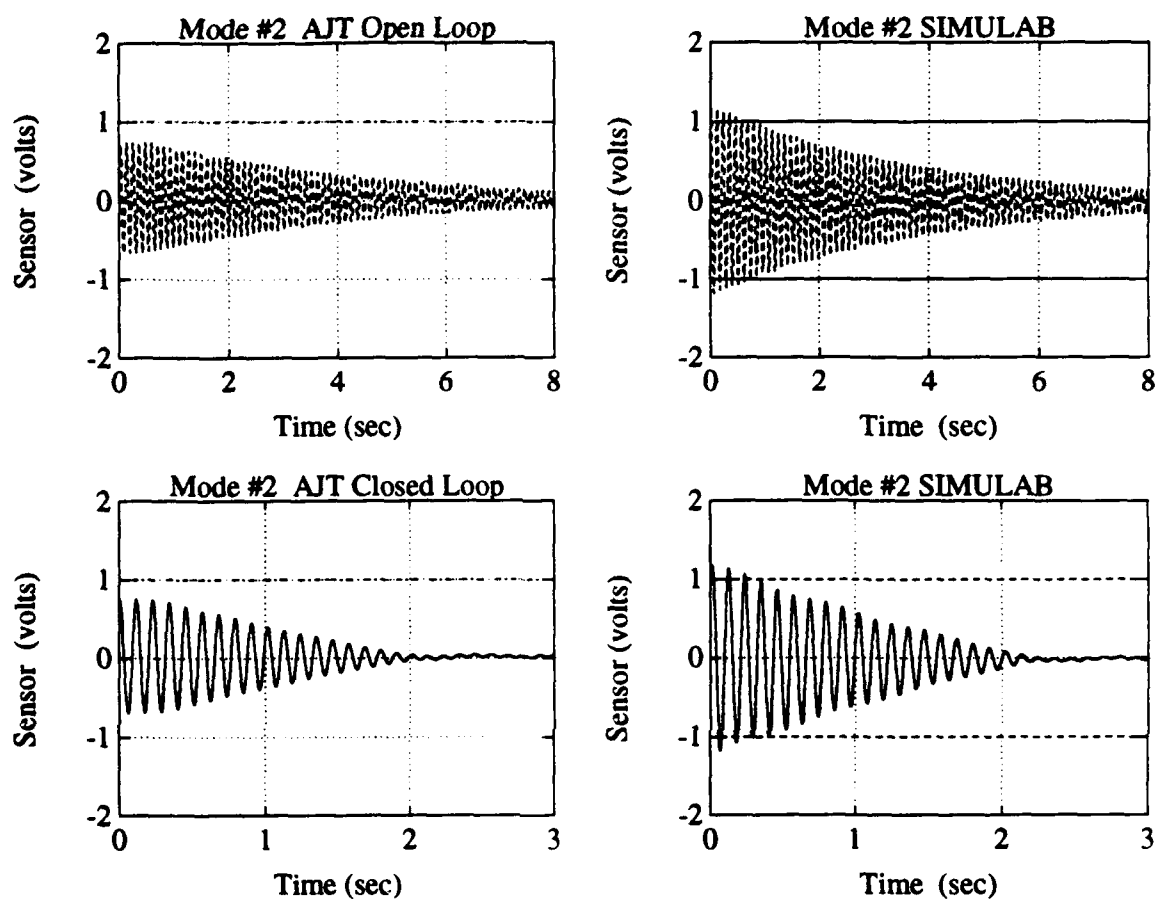


Figure 3.17: Mode 2 Experimental and Theoretical Open and Closed Loop Responses for AJT Controller

Figure 3.18 presents the closed loop SIMULAB model suitable for time domain simulation. The numerical outputs from the truss model are the same as described in table 3.1 in section 3.2.2.



## Chapter 4

# CONCLUSIONS AND RECOMMENDATIONS FOR FUTURE WORK

### 4.1 Overview

The setup, characterization, and control of a flexible structure and an optical beam-path is described in this thesis. This chapter discusses the conclusions obtained from the analysis and suggests future work that could be accomplished on the University of Washington Aeronautics and Astronautics (UWAA) truss testbed.

#### 4.1.1 Conclusions

The primary purpose of this thesis was to report the characterization of a flexible optical system and the investigation of classical control laws implemented to target a laser beam subjected to structural and non-structural disturbances. Another goal was to develop and validate a suitable simulation model using SIMULAB to provide a baseline theoretical model for future study of the UWAA truss testbed.

A linear model of the 20-bay truss was developed using MAPMODES and experimentally validated for the first four lateral vibrational modes. Excellent agreement between the finite element model and hardware lateral mode shapes and frequencies was found. The 63-DOF order FEM was reduced to four, retaining the tip lateral, tip angular, midpoint lateral, and station 14 lateral degrees of freedom. Modal damping of the flexible structure was approximated for the first four lateral vibrational modes with experimentally determined linear viscous damping coefficients for each resonant mode. The reduced order model used in simulation was validated in hardware, examining the free decay response at each lateral mode. Good agreement was found between the theoretical SIMULAB model and experimental data.

Linear and non-linear models of the AJT actuators were developed for use in control design. The linear model does not account for the bang-bang nature of the AJT and was of very limited use. The non-linear model of the AJT was used in



SIMULAB to provide accurate time domain simulation to test the effectiveness of the tilting mirror controller. The non-linear model of the AJTs was used in the design and simulation of velocity feedback controllers for the tip and mid span AJT pairs.

The tilting mirror platforms were the easiest to characterize because of their highly linear nature. The use of a larger mirror with the piezo actuated platform, as was done in this experiment, is not recommended in any future work. The increase of mirror area does not nearly compensate for the loss of angular authority and introduction of hysteresis into the tilting mirror.

Successful design and implementation of a disturbance rejection system for a structurally borne mirror platform was demonstrated. A proportional-integral (PI) controller was implemented on an analog computer to effectively reject structural and other optical disturbances to a laser beam path. The bandwidth of the closed loop system was 200 hz, a value that represents a compromise between good command following and disturbance rejection properties, analog implementation issues and noise considerations. The magnitudes of the disturbances were reduced by more than a factor of 100 for the first mode and by approximately factors of 20 and 10 for the second and third lateral modes respectively. The excitation of these modes provides the greatest amplitude errors on the sensing element so good rejection performance at these lower modes was critical.

Though the closed loop mirror system performed very well rejecting the first two lateral vibrational modes of the planar truss, the limited throw of the tilting mirror precluded it from being able to handle any large amplitude vibrational motion which is common when the first and second resonant modes of the truss are excited. Large amplitude excitation of the first mode causes the laser beam to miss the control mirror entirely. The tip and midstation AJT pairs along with their colocated accelerometers were used to suppress low frequency large amplitude structural vibrations and bring the beam disturbances back within the tilting mirror's range. Implementing a velocity feedback controller with an approximate integrator and a dead zone to reduce AJT chatter, the AJTs were able to quickly suppress any low frequency oscillation. The mirror platform was then used for fine positioning control once the truss vibrations were sufficiently damped with the AJT controller.

All of the experimental data were compared to SIMULAB generated results to

further validate the theoretical model. The SIMULAB model can be used as basis for designing new controllers for the UWAA truss testbed.

#### *4.1.2 Recommendations for Future Work*

The results presented in this thesis provide a good starting point for future projects and more advanced study of structural and optical control. The experimentally validated SIMULAB model can be used as a theoretical design basis.

The next step should be the digital implementation of the control laws reported in this thesis with LABVIEW or another I/O capable software/hardware package. The use of digital control would allow for a higher closed loop controller bandwidths as the analog limited controller gains could be increased to improve mirror performance. The controller designed in Chapter 3 did not tax the limits of mirror range or stability. The designer should be able to increase the performance of the control mirror to the noise level of the position sensing element. Digital implementation is also recommended when implementing any kind of higher order optimal or a non-linear control law.

Most practical space targeting applications require that the flexible structure be slewed. The planar truss can be fitted with casters and pinned at the hub instead of rigidly constrained to enable the truss to slew about its hub. The AJT actuators can be used to slew the truss and the tilting mirror used as a fine pointing controller once the target has been acquired.

The tilting mirror used in this experiment could never develop enough torque to cause any control-structure interaction problems. Large space based tilting mirrors may impart a reaction torque into the structure as the mirror moves to acquire the target. These reaction torques vibrate the truss and effect controller performance. A control structure interaction experiment can be designed with the existing hardware and another actuator that would use the control signal to the mirror and impart disturbances to the flexible structure based on control mirror motions.

Optimal control strategies incorporating full state feedback,  $H_2/H_{inf}$ , or SANDY based controllers can be designed for the truss system. The control strategy would involve a linear optimization of the truss and actuator states. Since the AJT can not be effectively modeled as a linear system, the AJT switching function could be optimized in the time domain or linear actuators, such as an RMA, could be used.

The AJT problem would be to determine the optimal time that the AJTs should be switched on and off to provide the best performance.

While the experimental setup described in this report is limited to one degree of freedom, it may be expanded to two degrees of freedom by using a second mirror as a control mirror in the vertical axis. In this case a dual axis quadrant photodetector could be used for feedback in two separate control loops. An experimental setup incorporating two degrees of freedom is necessary for most practical targeting and tracking applications. The single axis experiment serves as the baseline for more complicated applications.

## BIBLIOGRAPHY

- [1] Adams, R. J. Controller Design for a Laser Steering Mirror on a Flexible Structure. MS. Thesis, University of Washington, 1990.
- [2] Barker, K. J. Toward the Robust Control of High Bandwidth High Precision Flexible Optical Systems. PhD Dissertation, University of Washington, 1991.
- [3] Franklin, G. F., Powell, D. J., and Emami-Naeini, A. **Feedback Control of Dynamic Systems**. Addison-Wesely Publishing, 1991.
- [4] Hallauer, W. L. **MAPMODES** User's Guide. *Private Publication*, 2 February 1989.
- [5] Hallauer, W. L. Jr. and Lamberson S. E. *Experimental Active Vibration Damping of a Plane Truss Using Hybrid Actuation*. **AIAA** Paper 89-1169, *30th Structures, Structural Dynamics and Materials Conference, Mobile, AL*, April 3-5, 1989.
- [6] Hallauer, W. L. Jr. and Lamberson S.E. *A Laboratory Planar Truss for Structural Dynamics Testing*. Unpublished Paper, 1988.
- [7] Hughes, R. O. *Conceptual Design of Pointing Control Systems for Space Station Gimballed Payloads*. **AIAA** Paper 86-1986, August, 1986.
- [8] Meirovitch, L. **Analytical Methods in Vibrations**. Macmillan Publishing Co., 1967.
- [9] Przemieniecki, J. S. **Theory of Matrix Structural Analysis**. McGraw-Hill, 1968.
- [10] Harris, C. M. **Shock and Vibrations Handbook**. McGraw-Hill Inc., 1988.

- [11] **SIMULAB** The Mathworks, Inc. Version 3.5., Cochituate Place. 24 Prime Park Way. Natick, MA, 1991.
- [12] Shepherd, M. J. *Damping Characteristics of a 20-Bay Planar Truss*. Engineering Mechanics 499 Paper, United States Air Force Academy, 1990.
- [13] Shepherd, M. J. Studies in Control for Vibration Suppression of the UWAA 20-Bay Planar Truss. MS. Thesis, University of Washington, 1991.
- [14] Thompson, W. T. **Theory of Vibration With Applications** . Prentice Hall, 1988.

## Appendix A

### AJT CONTROL CIRCUITRY

Unlike the tilting mirror, an amplifier module was not provided for the AJTs. The electronic circuitry to run and control the air-jets was built on a circuit board using capacitors, resistors, operational amplifiers (OP-AMPs) and other integrated circuit elements. Figures A.3 and A.4 show the circuit diagram from the servo accelerometer to the analog input and from the computer output all the way to the solenoid. The rationale for the use of groups of these circuits is discussed in this appendix.

The sensitivity and range of the servo accelerometer output is determined by selecting the proper resistor to place between the signal pin and ground. The value of the resistor was determined from the following equation

$$\frac{\left[ \frac{V_E - V_I}{g_{max}} \right]}{C.S.F.} = \Omega_r \quad (A.1)$$

where  $V_E$  is the excitation voltage, nominally at  $\pm 15$  volts,  $V_I$  is the internal voltage, approximately 2.5 volts, and  $C.S.F.$  is the current scale factor of the accelerometer, 1.3 milliamps per g. The choice of required resistor  $\Omega_r$  is based upon the maximum number of g's expected and output sensitivity desired of the accelerometer. Since the accelerometer maximum output is  $\pm 15$  volts and the analog computer is linear only from zero to  $\pm 10$  volts, the resistor chosen must slightly overestimate the maximum number of g's expected. After trying various resistors and examining accelerometer output for each modal frequency at the tip and midpoint truss stations, a  $30k\Omega$  resistor was chosen. This corresponds to a maximum of 0.35g and a sensitivity of 39 volts per g.

Figure A.4 shows the electronic circuitry after the analog implemented controller. A three way switch is included in the circuit to give an operator functional control of the AJTs. When the switch is in the *Source* position, a signal generator is connected to the input of the tip AJT controller circuit, allowing the tip mounted AJT to excite the truss structure. The midpoint AJT is grounded. When the switch is in the *Off*

position both AJT pairs are disabled allowing the truss structure to vibrate freely without any excitation or active control. When the switch is in the *control* position both AJTs are connected with their respective control circuits and are enabled as active dampers.

The velocity feedback controller was designed using an approximate integrator to insure that when the control loop is closed, a DC signal would not ruin the feedback properties of the controller. However, when the switch is in either the *Source* or *Off* position the analog computer circuit is disabled and stray DC voltages will cause problems for the air-jets because the high gain 741N OP-AMPS will amplify the signal and cause one air-jet to switch on inadvertently. To eliminate this problem a lead network or differentiating circuit is implemented immediately following the switch.

A transfer function for the lead filter is easily obtained by solving the circuit diagram shown in figure A.1.

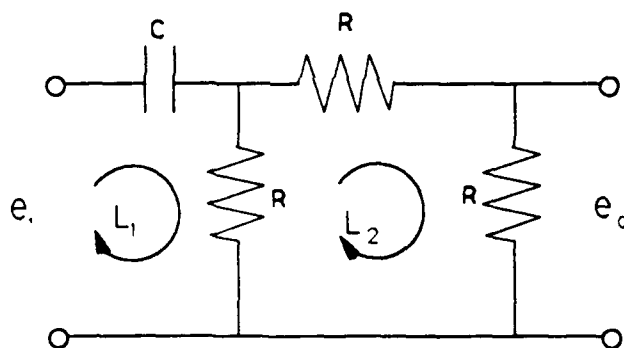


Figure A.1: Lead Network Circuit Diagram

Using Kirchoff's voltage law around loops  $L_1$  and  $L_2$  we obtain equations for the input and output potential voltages

$$e_i = \frac{1}{C} \int i_1 dt + R(i_1 - i_2) \quad (\text{A.2})$$

$$-e_o = R(i_2 - i_1) + Ri_2 = -Ri_2 \quad (\text{A.3})$$

where  $i_1$  and  $i_2$  are the currents flowing around loops  $L_1$  and  $L_2$  respectively. Taking the Laplace transforms of equations A.2 and A.3 we obtain

$$\begin{aligned}
 E_i(s) &= \frac{1}{Cs} I_1(s) + R(I_1(s) - I_2(s)) \\
 E_o(s) &= R(I_2(s) - I_1(s)) + RI_2(s) = -I_2(s)
 \end{aligned}
 \tag{A.4}$$

Solving for the currents  $I_1(s)$  and  $I_2(s)$  in terms of the other variable we have

$$I_1(s) = \frac{E_o(s)}{R} \quad I_2(s) = \frac{3E_o(s)}{R} \tag{A.5}$$

Substituting equation A.5 back into A.4 and examining the transfer function of output voltage to input voltage  $\frac{E_o(s)}{E_i(s)}$  and simplifying leaves

$$\frac{E_o(s)}{E_i(s)} = \frac{RCs}{3 + 2RCs} \tag{A.6}$$

The values of the resistance and capacitance were chosen so that the lead filter would have little effect on the frequencies at or above the first lateral vibrational mode of the truss. The first lateral mode of the truss is at 1.48 Hz corresponding to 9.3 radians per second. Based on these criteria the values of  $R$  and  $C$  were chosen to be 1 M $\Omega$  and 1  $\mu$ f respectively. Substituting in these values reduces the transfer function to

$$\frac{E_o(s)}{E_i(s)} = \frac{0.5s}{s + 1.5} \tag{A.7}$$

A frequency response plot for the lead filter is shown in figure A.2.

Figure A.2 shows that the magnitude reaches its steady state value at 1 Hz. However the control signal is cut in half. This gain reduction would be unacceptable for most linear controllers. The non-linear behavior of the AJT makes the output force independent of control signal magnitude as long as a dead zone is overcome. The dead zone is implemented keeping in mind the control magnitude reduction effects of the lead filter. An added benefit of the filter is a small phase lead at the first modal frequency which can improve control characteristics by reducing the lag time of the AJT in developing full force output.

Two 741N OP-AMPS were used in the AJT circuit. The AJTs are wired to provide bi-polar excitation and control of the planar truss. The circuit is set up so that one air-jet fires for a positive control voltage while the other fires for a negative voltage. A small dead zone is designed into the circuit as a necessary control element



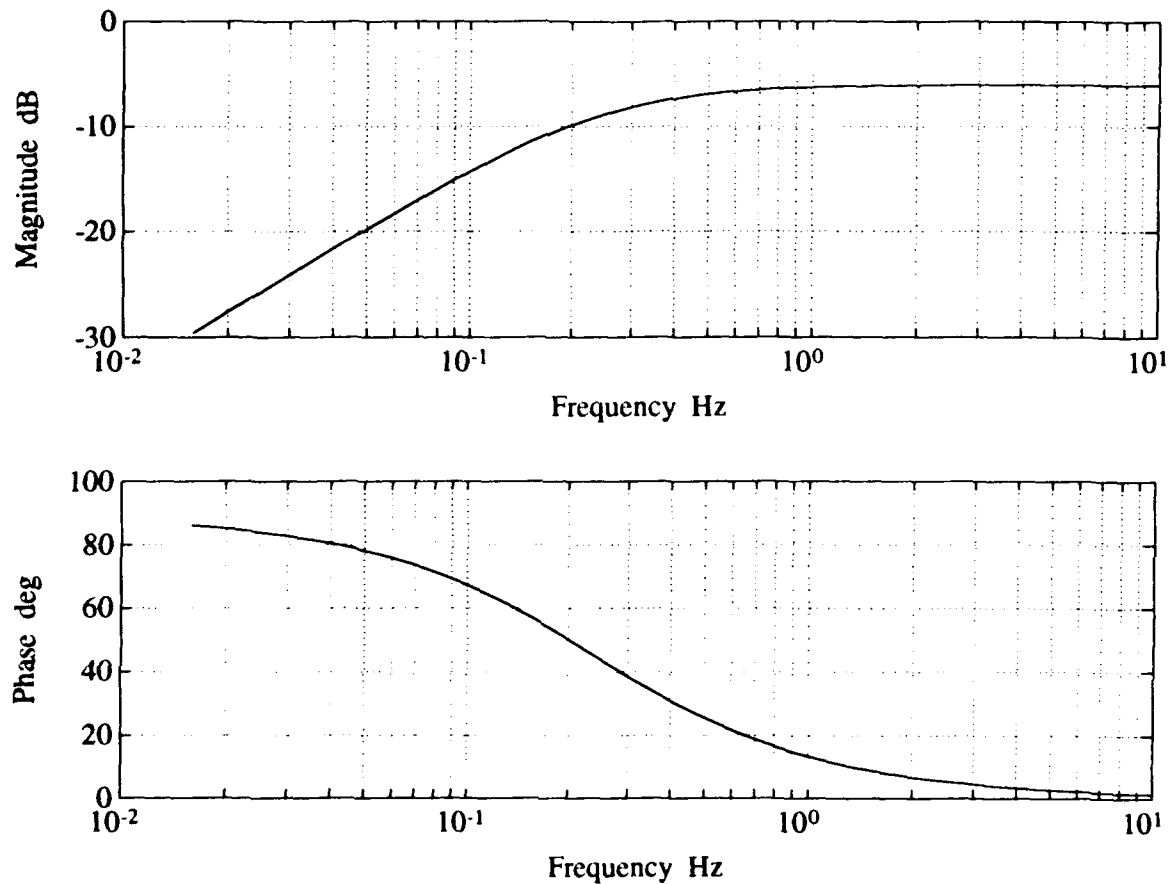


Figure A.2: Lead Filter Frequency Response

as discussed in Chapter 3. The dead zone is implemented using the 741N OP-AMPs. Each operational amplifier is offset with a positive or negative voltage, corresponding to the positive or negative air-jet, that must be overcome by the control signal in order to cause the transistor to fire, thus opening the solenoid valve and turning on the force. A  $10\text{ M}\Omega$  and  $3\text{ k}\Omega$  resistor are used along with a  $\pm 15$  volt input to produce a  $\pm 9\text{ mV}$  dead zone when combined with the control magnitude reduction effect of the lead filter.

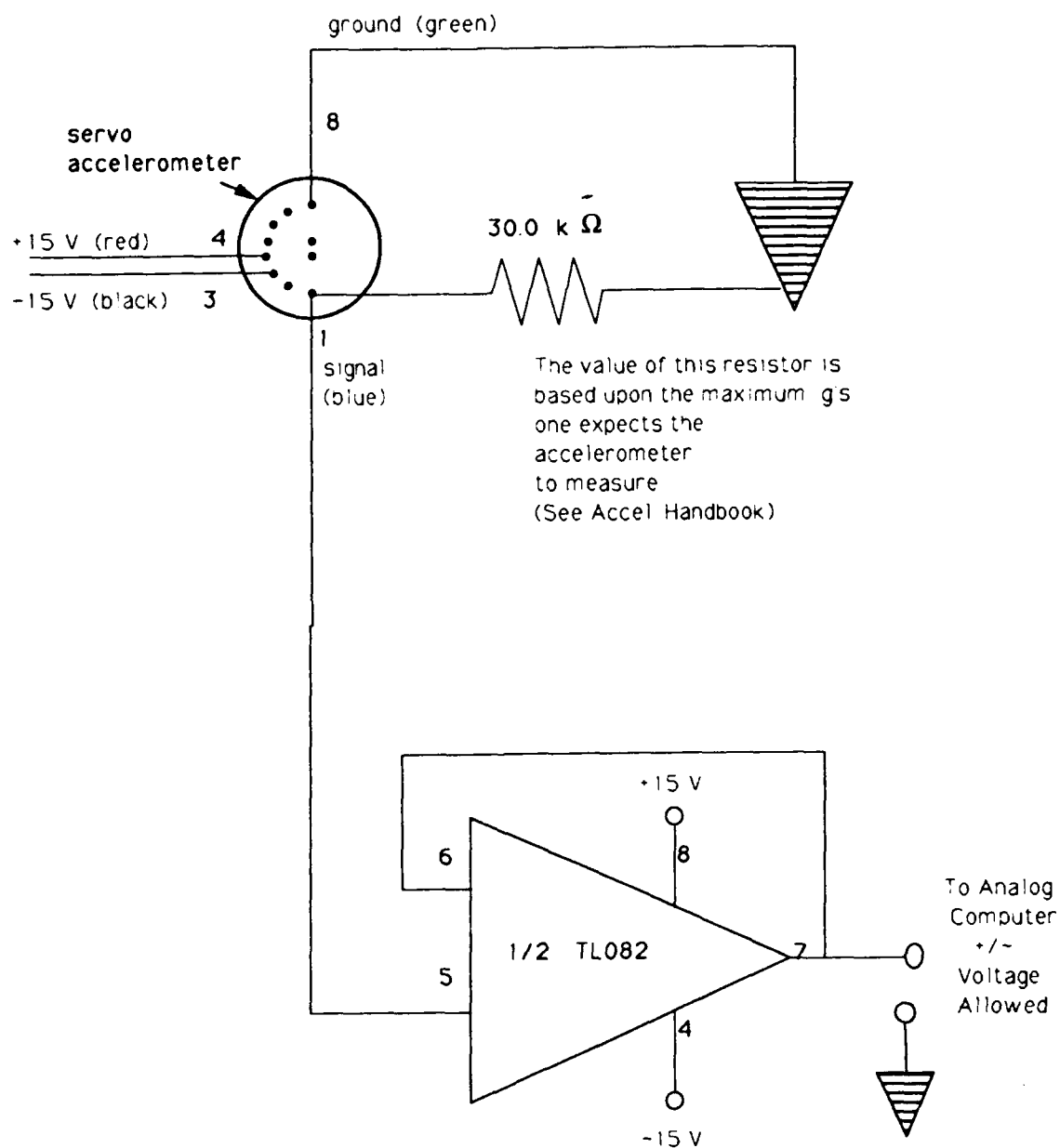


Figure A.3: Accelerometer Circuit



## Appendix B

### MODAL DAMPING COEFFICIENTS

The primary influence of damping on an oscillatory system is that of limiting the amplitude of the response at resonance. Damping has little influence in the response of frequency regions away from resonance. Equivalent linear viscous damping coefficients were determined for the first four modal resonant frequencies for the planar truss. The development assumes only linear viscous damping and is susceptible to errors caused by other types of structural damping such as non-linear coulomb damping (dry-friction).

A convenient method for determining the amount of damping present in a system is to measure the rate of decay of free oscillations. The greater the decay rate, the larger the damping will be. The logarithmic decrement procedure was used to obtain viscous damping coefficients for the first four lateral modes of the planar truss. This method was previously used by Shepherd [12] on a similar truss at the U.S. Air Force Academy. The method is outlined by Thompson [14].

For underdamped oscillatory motions the solution to the second order vibration problem is

$$y = Y e^{-\zeta \omega_n t} \sin(\sqrt{1 - \zeta^2} \omega_n t + \phi) \quad (B.1)$$

which is shown graphically in figure B.1. The logarithmic decrement  $\delta$  is defined as the natural logarithm of the ratio of any two successive amplitudes [14]. The expression for  $\delta$  is

$$\delta = \ln \frac{y_1}{y_2} = \ln \frac{e^{-\zeta \omega_n t_1} \sin(\sqrt{1 - \zeta^2} \omega_n t_1 + \phi)}{e^{-\zeta \omega_n (t_1 + \tau_d)} \sin(\sqrt{1 - \zeta^2} \omega_n (t_1 + \tau_d) + \phi)} \quad (B.2)$$

where the damped period  $\tau_d$  is

$$\tau_d = \frac{2\pi}{\omega_d} = \frac{2\pi}{\omega_n \sqrt{1 - \zeta^2}} \quad (B.3)$$

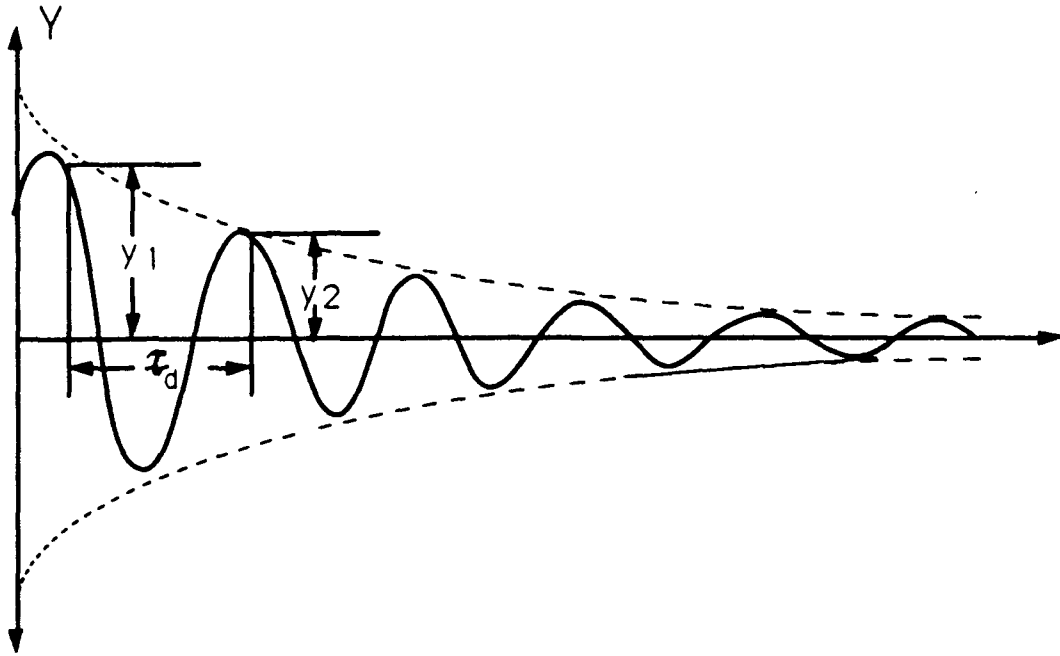


Figure B.1: Rate of Decay of Oscillation Measured by Logarithmic Decrement

Since the values of the sines are equal when the time is increased by the damped period, equation B.2 reduces to

$$\delta = \ln \frac{e^{-\zeta \omega_n t_1}}{e^{-\zeta \omega_n (t_1 + \tau_d)}} = \ln e^{\zeta \omega_n \tau_d} = \zeta \omega_n \tau_d \quad (\text{B.4})$$

Substituting in equation B.3 for  $\tau_d$ , the expression for the logarithmic decrement becomes

$$\delta = \frac{2\pi\zeta}{\sqrt{1-\zeta^2}} \quad (\text{B.5})$$

An expression for the damping ratio is then explicitly determined

$$\zeta = \frac{\delta}{\sqrt{4\pi^2 + \delta^2}} \quad (\text{B.6})$$

When the damping ratio is small, which is the case for lightly damped structures such as the flexible planar truss, the term  $\sqrt{1-\zeta^2}$  is approximately equal to one. Equation B.6 can be reduced to

$$\zeta = \frac{\delta}{2\pi} \quad (\text{B.7})$$

with little loss of accuracy. A similar approach for peaks separated by  $n$  cycles shows that the logarithmic decrement may be expressed as [12]

$$\delta = \frac{1}{n} \ln \frac{y_1}{y_{n+1}} \quad (\text{B.8})$$

The experimental method used to determine the logarithmic decrement for each mode was to drive the planar truss with the tip AJTs at each modal frequency until full lateral range of motion was achieved. The AJTs are then switched off and the truss is allowed to decay freely at the excited mode. For the first mode the truss endpoint was displaced one-half inch and released since the full excitation of the first mode would cause the ball bearings to be shaken loose. The decay was measured with the tip and midpoint mounted servo accelerometers. The previous derivation for the damping ratio was accomplished for displacement, but for low frequency lightly damped modal vibrations, the lateral acceleration will decay at the same logarithmic proportion. To realize a logarithmic decrement the peak amplitudes are measured at 90 and 10 percent of full displacement. Equation B.8 is used where the  $n$  cycles are counted between the two measurement points. Equation B.7 is then used to determine the damping coefficients for each modal resonant frequency. The truss tip and midpoint data were averaged to obtain the damping ratio except for the third mode where the midpoint is a structural node. The calculated damping coefficients may be seen in table 2.2.

## Appendix C

### NUMERICAL VALUES REQUIRED FOR SIMULAB SIMULATION

This appendix contains the numerical values for the reduced order truss model used in SIMULAB. The 4-DOF linear model is eighth order and has two inputs, the tip and midstation AJT actuator pairs. The parameter values for the non-linear AJT model rise time filter are also presented here.

#### *C.1 Four Degree of Freedom Linear Truss Model*

The open loop model describing truss dynamics is written in state space form

$$\dot{\mathbf{x}} = \mathbf{A}_r \mathbf{x} + \mathbf{B}_r \mathbf{u} \quad (\text{C.1})$$

where  $\mathbf{A}_r$  and  $\mathbf{B}_r$  are the reduced order state and input matrices respectively.

The states of the truss include the inertial lateral velocities and positions of the truss tip, midpoint, and station 14. Also included as states are the angular velocity and angular rotation about the tip batten center of gravity. The state vector is

$$\mathbf{x} = \begin{pmatrix} x_1 \\ x_2 \\ x_3 \\ x_4 \\ x_5 \\ x_6 \\ x_7 \\ x_8 \end{pmatrix} = \begin{pmatrix} \dot{y}_{tip} \\ \dot{\theta}_{tip} \\ \dot{y}_{mid} \\ \dot{y}_{14} \\ y_{tip} \\ \theta_{tip} \\ y_{mid} \\ y_{14} \end{pmatrix} \quad (\text{C.2})$$

where the  $y_i$ s specify the location of lateral motions and  $\theta$  specifies angular motions of the truss.

Since the AJT actuators are located at the tip and midspan of the structure, only the force inputs corresponding to those truss stations are retained in the reduced order input matrix.

$$\mathbf{u} = \begin{pmatrix} u_1 \\ u_2 \end{pmatrix} = \begin{pmatrix} f_{tip} \\ f_{mid} \end{pmatrix} \quad (\text{C.3})$$

The input units for  $f_{tip}$  and  $f_{mid}$  are  $lb_f$ .

The numerical values for the state and input matrices are shown in equations C.4 and C.5.

$A_r =$

columns 1 through 4

$$\begin{bmatrix} 4.857e+00 & -4.101e+02 & 2.429e-01 & -5.322e+00 \\ 2.682e-01 & -2.064e+01 & 3.738e-02 & -3.050e-01 \\ 1.103e+01 & -7.714e+02 & 2.878e+00 & -1.402e+02 \\ -1.989e+00 & 1.838e+02 & 7.006e-01 & 1.196e+00 \\ 1 & 0 & 0 & 0 \\ 0 & 1 & 0 & 0 \\ 0 & 0 & 1 & 0 \\ 0 & 0 & 0 & 1 \end{bmatrix}$$

columns 5 through 8

$$\begin{bmatrix} 4.008e+04 & -3.295e+06 & 1.1735e+03 & -4.118e+04 \\ 2.162e+03 & -1.660e+05 & 2.764e+02 & -2.434e+03 \\ 9.174e+04 & -6.407e+06 & 2.528e+04 & -1.164e+05 \\ -1.423e+04 & 1.391e+06 & 7.028e+03 & 8.289e+03 \\ 0 & 0 & 0 & 0 \\ 0 & 0 & 0 & 0 \\ 0 & 0 & 0 & 0 \\ 0 & 0 & 0 & 0 \end{bmatrix} \quad (\text{C.4})$$



$B_r =$

$$\begin{bmatrix} 1.521e+01 & 7.558e-01 \\ 2.960e-01 & 4.467e-02 \\ 7.558e-01 & 6.358e+00 \\ -2.798e+00 & 1.148e+00 \\ 0 & 0 \\ 0 & 0 \\ 0 & 0 \\ 0 & 0 \end{bmatrix} \quad (C.5)$$

The outputs of the SIMULAB model were the states and the accelerations of each retained degree of freedom as was shown in table 3.1.

### C.2 Non-linear AJT Parameters

The non-linear block diagram of the AJT used in SIMULAB incorporates a second order filter to approximate the rise time delay between the control signal and the development of full force from the AJTs.

The filter can be expressed in transfer function form as

$$G_r(s) = \frac{F_{ss}\omega_n^2}{s^2 + 2\zeta\omega_n s + \omega_n^2} \quad (C.6)$$

where the parameter values for equation C.6 are presented in table C.1.

Table C.1: AJT Rise Time Filter Parameter Values

$F_{ss}$	0.6 lb <sub>f</sub>
$\zeta$	0.95
$\omega_n$	200 rad/sec

## Appendix D

### REQUIRED INPUTS TO MAPMODES FOR UWAA PLANAR TRUSS

The finite element model for the UWAA planar truss was developed using MAPMODES, a matrix algebra package designed by Hallauer at USAFA [4]. MAPMODES operates on an input data file called *MAPMODES.IN* to produce the output data files. This appendix presents the required numerical inputs for *MAPMODES.IN* for the UWAA planar truss. Each truss member and the structurally borne actuators and sensors are accounted for in the MAPMODES model providing a very accurate modal matrices and natural frequencies.

MAPMODES uses three different coordinate systems as a method to input the data. Coordinate transformations are used to transform all input matrices to a coordinate system based upon the center of gravity (CG) of each rigid batten. The various coordinate systems are shown in figure D.1.

Coordinate system 1 is the system in which the flexible truss elements are input into the *MAPMODES.IN* file. The substructure stiffness and mass matrices also require the orientation of the truss members with respect to the x-axis and the length of the truss member respectively, in addition to the stiffness and mass of each member. The average stiffness and mass properties were measured. The results inputs to MAPMODES are presented in table C.2.

Table D.1: Average Mass and Stiffness Properties of Flexible Truss Members

Member	Orientation (deg)	Stiffness	Mass /Length ( $\frac{lb \cdot s^2}{in}$ )	Length (in)
Diagonal	$\pm 45$	$6.14 \times 10^4$	$5.775 \times 10^{-5}$	19.69
Longitudinal	0	$9.71 \times 10^4$	$7.130 \times 10^{-5}$	13.92

Realizing that  $y_1$  and  $y_2$  are the same coordinate, a transformation  $T_1$  (equation D.1) is used to get from four coordinates down to three.

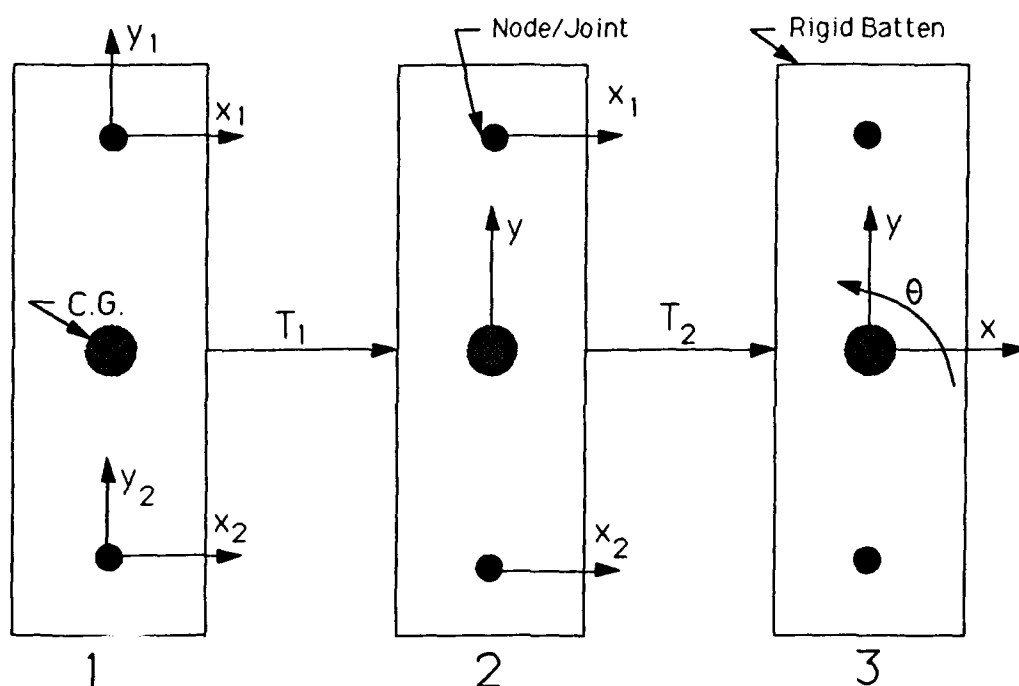


Figure D.1: MAPMODES Coordinate Transformations

$$T_1 = \begin{bmatrix} 1 & 0 & 0 \\ 0 & 1 & 0 \\ 0 & 0 & 1 \\ 0 & 1 & 0 \end{bmatrix} \quad (D.1)$$

Coordinate system 2 is then transform via  $T_2$  to obtain the sought after C.G. coordinate system where  $y$  indicates lateral motion,  $x$  longitudinal motion, and  $\theta$  tip angular motion. The coordinate transform from system two to three is

$$T_2 = \begin{bmatrix} \frac{1}{2} & 0 & \frac{1}{2} \\ 0 & 1 & 0 \\ 0 & 0 & 1 \\ -\frac{1}{c} & 0 & \frac{1}{c} \end{bmatrix} \quad (D.2)$$

where  $c = 13.92$ . The data can be entered into the *MAPMODES.IN* file in the coordinate system that is most convenient. However, one must remember to perform the appropriate transformations to get the final solution in terms of C.G. coordinates

(system 3).

The effect of the constraining structure on the flexible modes of the truss was approximated using the results obtained by Hallauer [6]. The mass matrices were then fine tuned so that the finite element model better matched the experimental mode shapes and resonant frequencies for the first four lateral vibrational modes. The constraining table mass and stiffness matrices are given in the C.G. coordinate system and presented in equations D.3 and D.4.

$$T_{mass} = 0.1 \times \begin{bmatrix} 1.238 & 0 & 0.0188 \\ 0 & 1.241 & -12.083 \\ 0.0188 & -12.083 & 248.78 \end{bmatrix} \quad (D.3)$$

$$T_{stiff} = 0.25 \times \begin{bmatrix} 2.862 \times 10^5 & 0 & 3.788 \times 10^4 \\ 0 & 1.958 \times 10^5 & -2.349 \times 10^6 \\ 3.788 \times 10^4 & -2.349 \times 10^6 & 8.020 \times 10^7 \end{bmatrix} \quad (D.4)$$

The scalar factors in front of the respective matrices are the scale factors used to match experimental data with the FEM for the UWAA truss.

The next step is the addition of the rigid batten (steel bar) assembly dominant inertia to the appropriate truss degrees of freedom. The steel bar assembly includes the rigid batten, a chordwise longitudinal truss member, two steel node joints, a bolt/washer combination, and two stainless steel plates glued to the bottom of the rigid batten to provide a smooth surface for the ball bearings. The joints and the bolt/washer combination are modelled as concentrated masses at the nodal points of each batten. The mass matrix for the steel bar assembly in C.G coordinates is

$$M_{sb} = \begin{bmatrix} m & 0 & 0 \\ 0 & m & 0 \\ 0 & 0 & I_{zz} \end{bmatrix} \quad (D.5)$$

where the mass<sup>1</sup> was measured to be  $0.0281 \frac{lb_f s^2}{in}$  and the moment of inertia of the rigid batten  $I_{zz} = 0.690 lb_f s^2 in$ .

---

<sup>1</sup> All mass and inertia values are normalized by the gravity constant ( $386 in/s^2$ ).

The next addition to the model is the mirror support structure and the tilting mirror platform mass matrix to the tip DOF of the FEM. The support structure was added directly to the steel bar assembly at the tip of the truss, and has the same form as equation D.5. The values for the mass and inertia of the support structure are  $m = 3.106 \times 10^{-3} \frac{lb_f s^2}{in}$  and  $I_{zz} = 0.0694 lb_f s^2 in$ . The mass matrix for the mirror is almost negligible, and could be omitted without introducing much error. It is included here for thoroughness. The tilting platform mass matrix has the same form as equation D.5 with  $6.435 \times 10^{-2} \frac{lb_f s^2}{in}$  and  $1.112 \times 10^{-4} lb_f s^2 in$  for the mass and inertia values respectively.

The last addition to the MAPMODES model is the matrix of concentrated masses of colocated thruster/accelerometer combinations attached at the center and tip of the planar truss. The actuator assembly includes the AJT actuator and its mounting structure, and the servo accelerometer combined with the accelerometer housing. The AJT assemblies are located at the joint and we assume that the accelerometer assembly mass is lumped at a node with only slight loss of accuracy. The matrix of concentrated masses for the accelerometer and AJT actuator assembly in C.G coordinates is

$$M_{AJT/Accel} = \begin{bmatrix} 2.804 \times 10^{-3} & 5.609 \times 10^{-3} & 7.559 \times 10^{-5} \end{bmatrix} \quad (D.6)$$

The units for each element in  $M_{AJT/Accel}$  are  $\frac{lb_f s^2}{in}$ .

## Appendix E

### EQUIPMENT LIST

This appendix provides a listing of the optical components required for the experiment performed in this thesis. For a complete listing of the truss and AJT actuator components see Shepherd [13]. This list is by no means all inclusive, but provides a good idea of what basic hardware is required to repeat this optical part of the experiment. The custom made hardware accessories were constructed by professional machinists in the department of Aeronautics and Astronautics machine shop.

#### *E.1 Laser Hardware and Optical Bench*

- 5.0mW Helium-Neon class IIb Laser CAT No. B61,333

Edmund Scientific Co., 101 E. Gloucester Pike Barrington, NJ 08807 Phone:(609)573-6250

- Twin Ring Laser Mount CAT No. B71,791
- Laser/Optics Honecomb BreadBoard Laboratory Table (3' x 4') CAT No. B38,434

#### *E.2 Optics*

- BroadBand 50/50 Dielectric Beamsplitter (2 in diameter) Cat No. 20B10BK-7

Newport Corporation P.O Box 8020 18235 Mt. Baldy Circle. Fountain Valley, CA 92728. Phone:(714)963-9811

- Cylindrical Planar Convex Optical Cylindrical Lens 100mm Focal length CAT No. CKX100
- Compact gimbal beamsplitter mount CAT No. GM-2

- Various height support posts and holders to screw into the optical bench

### *E.3 Custom Fabricated Optical Hardware*

- Mount for 2in square cylindrical lens. The mount was constructed to fit on top of a stainless steel post.

### *E.4 Control Mirror and Accompanying Hardware*

- 2 Piezo actuated tilting mirror platforms with strain gage sensors CAT No. S-226.00

Polytec Optonics, Inc. 3001 Redhill Ave. Bldg. 5-102 Costa Mesa, CA 92626  
Phone:(714)850-1835

- 1 Piezo Driver Amplifier with Controller Module CAT No. P-864.00 and E-808.00.

### *E.5 Custom Fabricated Tilting Mirror Hardware*

- Mirror platform support structure to attach tilting mirror platform to a truss station.
- Tilting mirror platform support structure to enable the mirror to be attached to one of the stainless steel posts and mounted into the optical bench.

### *E.6 Optical Sensing Equipment*

- PIN-SL76 Very high accuracy linear single axis position sensing photodetector  
UDT Instruments. 12151 Research Parkway, Orlando FL 32826 Phone (407)282-1408
- Model 301 DIV Signal Conditioning Amplifier

### *E.7 Custom Designed Sensing Hardware*

- Photodetector mount that can be screwed onto a steel post
- Darkened box around photodetector to reduce reflection and noise from room lighting.

### *E.8 Instrumentation and Electronics*

- Comdyna GP-6 Analog computers

Comdyna Inc. 305 Devonshire Road, Barrington, IL 60010 Phone:(708)381-7560

- Hewlett Packard HP35665A Dynamic Signal Analyzer



## BIBLIOGRAPHY

- [1] Adams, R. J. Controller Design for a Laser Steering Mirror on a Flexible Structure. MS. Thesis, University of Washington, 1990.
- [2] Barker, K. J. Toward the Robust Control of High Bandwidth High Precision Flexible Optical Systems. PhD Dissertation, University of Washington, 1991.
- [3] Franklin, G. F., Powell, D. J., and Emami-Naeini, A. **Feedback Control of Dynamic Systems**. Addison-Wesely Publishing, 1991.
- [4] Hallauer, W. L. **MAPMODES** User's Guide. *Private Publication*, 2 February 1989.
- [5] Hallauer, W. L. Jr. and Lamberson S. E. *Experimental Active Vibration Damping of a Plane Truss Using Hybrid Actuation*. **AIAA** Paper 89-1169, *30th Structures, Structural Dynamics and Materials Conference, Mobile, AL*, April 3-5, 1989.
- [6] Hallauer, W. L. Jr. and Lamberson S.E. *A Laboratory Planar Truss for Structural Dynamics Testing*. Unpublished Paper, 1988.
- [7] Hughes, R. O. *Conceptual Design of Pointing Control Systems for Space Station Gimballed Payloads*. **AIAA** Paper 86-1986, August, 1986.
- [8] Meirovitch, L. **Analytical Methods in Vibrations**. Macmillan Publishing Co., 1967.
- [9] Przemieniecki, J. S. **Theory of Matrix Structural Analysis**. McGraw-Hill, 1968.
- [10] Harris, C. M. **Shock and Vibrations Handbook**. McGraw-Hill Inc., 1988.